A Time Domain Boundary Element Method for Fluid-Structure Interaction Analysis on a Discontinuous Surface

Vom Promotionsausschuss der
Technischen Universität Hamburg

zur Erlangung des akademischen Grades

Doktor-Ingenieur (Dr.-Ing.)

genehmigte Dissertation

von
Moritz Hartmann

aus
Aachen

2023

1. Gutachter:	Prof. DSc. (Tech.) Sören Ehlers Technische Universität Hamburg
2. Gutachter:	Prof. Dr. rer. nat. Norbert Hoffmann Technische Universität Hamburg
Vorsitzender des Prüfungsauschusses:	Prof. Dr.-Ing. Robert Seifried Technische Universität Hamburg

Tag der mündlichen Prüfung: 25. August 2023

Digital Object Identifier (DOI): https://doi.org/10.15480/882.8909
Open Researcher and Contributor ID (ORCID): https://orcid.org/0000-0001-7282-0399

Summary

In this thesis, the development of the two-dimensional time domain solver cBEM for modeling linear hydrodynamic problems is described. The approach was based on Potential Flow Theory and applied Boundary Integral Equations with that the governing Boundary Value Problem was solved and the interactions of body and surface gravity waves were modeled. The embedding of the High-Order Spectral procedure into the Boundary Element Method in the symmetric Galerkin formulation represents an innovative coupling method for the treatment of hydrodynamic problems.

The explicit account of a surface discontinuity represented by the body in the free surface boundary domain, the strategy of incorporating the High-Order Spectral approach in the Boundary Element Method, and the development of suited desingularization techniques for kernel functions up to hypersingular order had been considered within this thesis. As higher-order basis functions had been used for the approximation of solution function space and geometry, the results of cBEM in terms of the boundary quantities, the potential and its normal derivative, were of good accuracy.

cBEM can be accounted as the foundation of a highly efficient three-dimensional nonlinear Boundary Element Method solver with possible future application e.g. in the research fields of analyzing nonlinear body motion due to nonlinear wave excitation in numerical wave tanks and for the optimization of ship hull geometries in the early design phase. For offshore operations, the deterministic wave and motion prediction would help to increase safety and cBEM was designed to fit into a holistic approach containing wave inversion, nonlinear wave propagation, and motion prediction. The efficient evaluation of the mixed Boundary Value Problem with highly efficient methods would allow predictions over a period of time that meets industry expectations.

The work is structured as follows. In the introduction, the scope of the work is highlighted and limitations and innovations are outlined. In the literature review presented thereafter, the Boundary Element Methods used in Marine Hydrodynamics are categorized into three main streams, and related research contributions are summarized. Based on this, the research gap is outlined and a global hypothesis defined. The research hypotheses structure and summarize the main concerns according to the global hypothesis and give the frame for the development of cBEM.

In chapter two, the theory of Boundary Integral Equations and numerical tools accounted for in the Boundary Element Method approach are summarized. Furthermore, the Linear Wave Theory and the High-Order Spectral method as well as the basic problems of wave-body interaction are described.

On the mathematical foundation and the introduction of the computational methods represented here, the steps for the development of the cBEM solver are presented in chapter three. After an overview of the steps, the Boundary Integral Equations for the different solvers are described. The direct formulation of cBEM is given and the methods accounted for in pre-, post-, and processing are introduced. It follows the verification of the approaches including the free surface solver fsBEM, the coupled solver cBEM, and the transient cBEM solver for the continuous and discontinuous surfaces.

The validation section, chapter four, shows the application of cBEM for hydrodynamic problems. The submerged and free surface piercing geometries were considered and linear problems with a forced oscillating body, the free surface elevation over a submerged cylinder, and the diffraction of waves due to a body below were compared with literature references.

The final discussion in the review of the research hypotheses follows and the conclusions are drawn. By identifying the status of the work described herein, future steps are pointed out. The extension of cBEM to a three-dimensional solver, equipped with efficient solving strategies and nonlinear extensions is outlined and future applications are given. Their potential is highlighted and the required developments are depicted.

Acknowledgements

The following stands representative to all those who have supported me in preparing this thesis and during my time as a research assistant at the TUHH.

I'm glad to meet many engaged, open-minded, inspiring, and supportive people. In addition to working on my scientific topic, I particularly value this aspect of my professional life. So many colleagues and friends have helped me to develop ideas and gain knowledge through discussions, and many pleasant memories will remain from this intense time.

First, I want to thank Prof. Sören Ehlers for his openness, trust, and constructive cooperation. During my time at the Institute of Structural Design and Analysis, his non-hierarchical leadership and openness to dialog and discussion helped me immensely in my scientific work.

Prof. Norbert Hoffmann I would like to thank for his support during my time as a research assistant. Even in challenging phases, he encouraged me on my path. I learned a lot from our discussions and always appreciated his perspective as a physicist.

Prof. Robert Seifried took over as chair of the examination committee and organized the venue and date for the presentation and examination. For that, I want to thank him very much.

Dr. Marco Klein was instrumental in introducing me to the field of fluid-structure interaction, and his honest and direct communication, as well as his matching questions, often helped me in concrete scientific practice. I am very happy for this and for our work together.

Dr. Franz von Bock und Polach I got to know during my Master's thesis, and without him and Sören Ehlers, I probably wouldn't have come back to the TUHH. I want to thank him for many helpful and path-guiding discussions.

During my research stay in Turin, Prof. Miguel Onorato, Dr. Francesco de Vita and I worked together, and I met Dr. Giovanni Dematteis and the team of the Department of Physics at UniTo. I'm very thankful for the opportunity to have researched together, the exchange of knowledge and the hospitality I received.

With Jasper Behrendt and Dr. Jakob Schwarz, I developed important insights and ideas that have been incorporated into this work. With their extensive knowledge of numerical methods and their implementation, they were crucial discussion partners for me. I'm very grateful for their support and cooperation.

Dr. Nicolas Desmars I would like to thank for the constant exchange on our research topics and many amicable dialogues. It serves as a stroke of luck to have met him, and I look forward to working together in the future.

I would like to thank my family for their emotional and unconditional support, and the many encouraging conversations. They have paved the way for me to write this thesis.

Linn deserves my deepest thanks. With her understanding, confidence, and encouragement, she has helped me an indescribable amount and given me so much support for my work.

Table of contents

Nomenclature

Abbreviations

BEM	Boundary Element Method
BIEMH	Boundary Integral Equation methods for Marine Hydrodynamics
BIE	Boundary Integral Equation
BIO	Boundary Integral Operator
cBEM	Coupled Boundary Element Method
DoF	Degree of Freedom
FFT	Fast Fourier Transform
FMM	Fast Multipole Method
fsBEM	Free surface Boundary Element Method
FSGF	Free Surface Green Function
GH	Global hypothesis
GMRES	Generalized Minimal RESidual
HOS	High-Order Spectral
LWT	Linear Wave Theory
MEL	Mixed Eulerian-Lagrangian
PDE	Partial Differential Equation
pFFT	Precorrected Fast Fourier Transform
RAO	Response Amplitude Operator
RH	Research hypothesis
RKx	x-th order Runge-Kutta integration
RSGF	Rankine-Source Green Function
WEC	Wave Energy Converter

Boundary Integral Equations

Γ	Boundary

γ_0	Trace
γ_1	Trace of the normal derivative
$\mathcal{A}$	Adjoint boundary integral operator
$\mathcal{D}$	Double boundary integral operator
$\mathcal{H}$	Hypersingular boundary integral operator
$\mathcal{S}$	Single boundary integral operator
S	Steklov-Poincare operator
Ω	Domain
σ	Bounded free term, source strength
C	Calderon projector
D	Double layer potential
G	Fundamental solution, Green Function
g_Γ	Boundary condition
N	Neumann potentials and its normal derivative
r	Distance of discrete points
S	Single layer potential

Mathematical variables

α_n	Lebesgue function
δ	Delta-distribution
sinc	Sinus cardinalis function
$\tilde{f}$	Fourier transform of f
a_k	Coefficients
C^k	Space of k-times bounded and continuous differentiable functions
D_n	Dirichlet kernel
E	Error
f	Arbitrary function
H	Hilbert space
h	Step size
l_k	Lagrange basis polynomials
L_p	Space of power p integrable functions
n	Unit normal vector

p	Polynomial function	
t	Unit tangent vector	
w	Weight function	
W_2^s	Sobolev-Slobodeckij space (also H^s)	
W_p^k	Sobolev space	
x_k	Sites of control points	

Physical variables and computational parameters

ρ	Density	kg m^{-3}
dt	Time increment	s
dx	Grid spacing	m
g	Gravity of earth = 9.81	m s^{-2}
L	Domain length	m
N	Number of grid points	–
nT	Number of time steps	–

Surface gravity wave variables

η	Surface elevation	m
$\hat{\eta}$	Amplitude of surface elevation	m
κ	κ operator	m^{-1}
λ	Wave length	m
ω	Angular wave frequency	rad s^{-1}
ϕ	Velocity potential	m^2 s^{-1}
ϕ_p^m	Modal amplitude	m^2 s^{-1}
ψ_p	Global basis function	–
τ	S-curved blend in function for u	–
ε	Wave steepness	–
φ	Phase shift	$^\circ$
c_p	Phase velocity	m s^{-1}
c_{gr}	Group velocity	m s^{-1}
D	Water depth	m
H	Wave height	m

k	Wavenumber	m^{-1}
p	Pressure	$\mathrm{kg\,m}^{-1}\,\mathrm{s}^{-2}$
s	Scaling factor for τ	–
T	Wave period	s
u	Stream velocity	$\mathrm{m\,s}^{-1}$

Body parameters

B	Breadth body	m
h	Submergence depth	m
T_B	Draught body	m
x_c, z_c	Position of body center	m
$y_a, \hat{y}$	Oscillation amplitude in sway mode	m
$z_a, \hat{z}$	Oscillation amplitude in heave mode	m

Wave-body interaction parameters

ϵ	Phase angle between force and motion	°
ψ	Phase angle between force and wave	°
A	Added mass	$\mathrm{kg\,m}^{-1}$
D	Damping coefficient	$\mathrm{kg\,s\,m}^{-1}\,\mathrm{rad}^{-1}$
F	Excitation force	$\mathrm{kg\,m\,s}^{-2}$
KC	Keulegan-Carpenter number	–

Subscript indizes

$(.)_B$	Body
$(.)_D$	Dirichlet
$(.)_N$	Neumann
$(.)_p$	Integrability class
$(.)_S$	Free surface
$(.)_W$	Water
$(.)_{osc}$	Oscillation

Superscript indizes

$(.)^{ext}$	Exterior
$(.)^{int}$	Interior
$(.)^{k}$	Differentiablity class

Chapter 1

Introduction

1.1 Scope of the work

The coupled Boundary Element Method (cBEM) is a two-dimensional, symmetric Galerkin approach using a direct Boundary Integral Equation (BIE) formulation suited for mixed Boundary Value Problems (mixed BVPs) with that, the monolithic coupling of wave and body dynamics in hydrodynamic applications can be modeled. The coupled approach allows the incorporation of wave dynamics in an efficient setup in that higher-order approximations for the solution and the geometry can be applied to obtain accurate solutions. cBEM represents the foundation for a real time capable, higher-order BEM that solves the interaction of waves and ship motions and targets to increase the safety and efficiency of offshore operations.

In the framework of this thesis, the free surface was represented by an equidistant distribution of collocation points, which allowed the incorporation of spectral-like approaches, e.g. the High-Order Spectral (HOS) method. Instead of using global basis functions and periodic boundary conditions, as usually done in spectral approaches, the HOS method was employed in the cBEM by using basis functions with compact support and applying the method of images that allow periodicity in the lateral spatial directions without the need of periodic Green functions.
The formulation of the HOS in terms of representation functions with compact support allowed the explicit account of the free surface discontinuity that appears due to the presence of the body. The handling of truncated elements as well as the evaluation of singular integral kernels with weak, strong, and hypersingular properties was one leading order problem addressed in this thesis.

The focus of this thesis was the development of a new numerical method. This included the design and mathematical formulation of the coupling approach as well as the development and implementation of new numerical approaches for handling discontinuities in the boundary domains. The proof of consistency and concept was done by the verification with analytic solutions and the application of the method

to well investigated hydrodynamic problems. For the development steps, the previously by J. Schwarz [150] implemented frequency domain BEM solver was accounted as a reference and helped efficiently solve methodological problems.

Subjected to this, the development and assembly of symmetric Galerkin Boundary Integral Operators (BIOs) are explained and the verification by testing against analytical solutions for different versions of the solver is presented. Furthermore, the implementation of a time integration scheme for the mixed boundary condition BVP and the proof of its validity in terms of stability and convergence is presented.

For the validation of the method, a submerged and surface piercing fixed body was investigated and hydrodynamically analyzed. The body was chosen to be of rectangular or circular geometry.

The limitations and new features of the solver version covered in this thesis are listed below.

Limitations

The numerical approach described in this thesis is limited in terms of:

- the restriction to two-dimensional domains,
- the linearization of wave dynamics,
- the consideration of forced body motions around the bodies equilibrium position,
- the academic character of the presented test cases with intersection at element endpoints,
- and the implementation of the code in a non efficient code environment that allowed effective code debugging.

Innovations

The presented approach is a novel method for wave-body interaction problems and is innovative in terms of:

- handling the free surface discontinuity due to the presence of the body,
- the direct evaluation of coupling operators including hypersingular kernel functions,
- the monolithic approach for coupling body and wave dynamics and the use of basis function with compact support as local representations for spectral basis functions which both allowed the incorporation of a HOS like approach in the BEM,
- as well as because of the symmetric Galerkin formulation, which allowed effective accounting for the discontinuity of the free surface and mixed BVP.

1.2 Applications of the Boundary Element Method in Marine Hydrodynamics

For the analysis of the loads and motions on ships and marine structures in waves, three main categories exist, the sea trial, the model test, and the numerical modeling. The first fulfills the consistency required for the physics inherently, but the complexity level is maximal, the ship had to be already built and equipped with measurement techniques. The model test can be performed in the design stage of a project and here the physics are inherently correct as well. By accounting scaling laws, the physics acting on model scale can be translated to the full scale model. Numerical modeling is arguably the most flexible of the three categories and relatively cheap in resources, but physical consistency is not guaranteed. The numerical methods have to be chosen regarding their physical limitations and the targeted accuracy level. Their efficiency is of great relevance today and in view of the changing climate on earth, the saving of resources is crucial.

The numerical, physic-based evaluation for the wave-ship and -structure interaction can be treated by different methods. The decision on which one to use is mainly based on accounting for the dominant flow and motion characteristics (yield physical limitations) and choosing the order of nonlinearity (yield accuracy) taken into account. Both are related to each other and have to be considered in common, but the latter choice is more in the hand of the method's user. In contrast, the first can be derived mostly by accounting for the body characteristics, the marine environmental conditions, and the operational profile.

The physical limitation relies on the choice of the complexity of the governing equations. For accounting viscosity and vorticity, the incompressible Navier-Stokes equation is the mathematical model of choice and methods as Direct Numerical Simulation (DNS) or the Reynolds-averaged Navier-Stokes (RANS) equation methods and Large Eddy Simulation (LES) with the related turbulence closing methods can be used. If viscosity is not relevant, but vorticity is significant, then the incompressible Euler equation based methods are applicable. Further simplification to an irrotational flow gives the Potential Flow Theory, mathematically represented by the Laplace equation and appropriate boundary conditions, which is a reasonable choice for several problems in marine hydrodynamics .

The Laplace equation and the related initial boundary conditions of the fluid domain and the included body essentially form an elliptic BVP. This can be solved by formulating a BIE and numerical treatment by the BEM. The main advantage of this method is that flow properties can be evaluated by accounting only for the domain's surface quantities. Consequently, the discretization of the surface domains is sufficient, and the computational effort can be reduced. The flow quantities of interest in this method are the velocity potential and its normal derivative, solving for one requires the definition in terms of the boundary conditions of the other.
A specific BVP problem might be characterized by its mathematical formulation and the numerical method used for solution evaluation. The mathematical formulation in terms of BIEs includes the use of a fundamental solution, also referred to as the Green function. The numerical method can be further subdivided into the topics of numerical integration, discretization of geometry and solution, the assembly of the BIE kernel functions, the linear system solvers, and its acceleration. The topics related to foundation, discretization, integration, and assembly will be studied in the following chapters because they are a distinguishing feature of BEM approaches applied in marine hydrodynamics. The aim is to provide a methodological overview from which the necessity for the development of the cBEM follows and relevant research questions can be derived.

A retro perspective view on the formulation of marine hydrodynamics BEM approaches allows to distinguish between three main streams, where the first includes the Free Surface Green Function approaches, the second the Rankine-Source Green Function methods, and the third a broader spectrum of BIE methods applied to the wave-body interaction problem. The formulation of BIEs and the Green function influences other properties of the approaches, as the accounted order of nonlinearity for geometry and solution representation and the hydrodynamic problem that is the focus of the analysis. The three main directions and related literature are detailed below.

1.2.1 Free Surface Green Function approaches

The first group, the Free Surface Green Function (FSGF) methods, see for an overview e.g. Yeung [192], Xie et al. [187] and el Moctar et al. [56], account Green functions containing a singular part and a harmonic part, where the latter component has to be evaluated in the manner that the Laplace equation and the boundary conditions, namely the dynamic and kinematic free surface - , the radiation - and the bottom boundary condition, are satisfied. The methods account the linearized equations of the wave-body problem and are mostly evaluated in frequency domain.

A short historical overview can start from the theoretical work and the first solutions with BIEs and FSGFs on the linearized radiation problem, a surface piercing body in forced oscillations, in two and three dimension in the 1940s and 1950s. The determination of ship motion in waves came more into the focus which rose the problem's complexity. The increasing computational power and the foundations of theo-

retical frameworks to solve the governing ordinary differential equation (ODE) in the 1970's and 1980's allowed significant development steps of numerical methods for ship wave interaction. The evaluation of related hydrodynamic parameters, essential for the ship motions, the development of efficient algorithms for the evaluation of the FSGFs and the solutions to certain method based problems as irregular frequency occurrence helped to make the methods applicable to problems in the industry from the early 1990's on. The considerations of different FSGF evaluation methods and acceleration techniques for the increase of accuracy and efficiency were part of the next stages. Until now research and developments related to the FSGF methods is going on and underlines the relevance of those methods for the shipbuilding and offshore industry.

That a unique solution in terms of the velocity potential for the BIE used for the linearized radiation problem in three dimension exists, has proven by John [89]. The waves radiating from the harmonically oscillating body has been decomposed in a regular wave and a radiation part. Moreover, the author has already outlined the difficulties related to irregular frequencies and the singular character of the integral kernel.
For the same problem, Ursell has provided firstly solutions for the two-dimensional case, in the regime of long [167] and short waves [170]. In [167], the author has constructed a polynomial approximation for the stream function under the assumption of the free surface and the bottom boundary condition. The approach has been used for the calculation of the added mass of a surface piercing body and explicit values of the results has been tabulated for different wavenumbers and body dimensions. The short wave problem solution, a case where an exact closed form solution does not exist, has been found by using a BIE. The solution for radiated waves of an oscillating body in a three-dimensional potential flow has been provided by Havelock [80] by means of the added mass and the damping coefficient over the investigated frequency range.
Wehausen & Laitone [181] have summarized the previous research on FSGFs and have provided solutions for the velocity potential fulfilling the free surface, radiation and bottom conditions in a three-dimensional potential flow. The solutions for infinite and finite water depth for simple singularities have been based on Bessel functions, which provide a solution for the Laplace equation in spherical coordinates, and a Cauchy Principal Value (CPV) integral, see Subsec. (2.1.7).
Later FSGF approaches for the oscillating body wave problem, as those of Kim [93] and Hearn [81], have been based on the evaluation of the BIE by spherical harmonics, which have been derived in Ursell [171] and have preliminary applied in Havelock [80]. Guevel et al. [69] have solved the radiation problem by considering an exponential integral, which have been later also used by Noblesse [131] and Martin [114], see e.g. Xie et al. [187].

In terms of practical applications in marine hydrodynamics, the high number of evaluations of the Green function to find a solution for the potential and its derivative in frequency domain (10 -100 frequencies require 10^6-10^8 evaluations of the Green function, see Newman [125]) made it necessary to find efficient solutions to decrease the time for evalauting the singular integral in the BIEs.
Noblesse [132] and Newman [125] have introduced methods that allowed the efficient evaluation of the solution for the BIEs in the FSGF approach for the application of wave ship interaction. Noblesse has used series expansion instead of evaluating the integrals by costly direct numerical integration. The use of BIE representations for the near and farfield regime has allowed to split the computational domain in two or more subdomains.
Based on this approach, Telste & Noblesse [164] have developed an algorithm and could speed up the computation of the potential and its derivatives. Newman has replaced the numerical integration by more efficient computable terms. In the direct neighborhood of the singularity a polynomial approximation has been used and at a reasonable distance to the singularity an analytic expansion has been accounted. The author has derived the expansions and polynomials for the deep water and finite depth water on the basis of the FSGFs provided by Havelock [80] and by John [89], respectively.

In Newman [126], a panel method suited for the numerical treatment of wave-body interaction with the FSGF approach has been introduced. The panel method is a specific BEM approach widely used in the aero- and hydrodynamic community with the advantage that numerical integration is not explicitly

necessary and can be replaced by geometrical properties of the discretization elements. Hess & Smith [82] have introduced the panel method and applied it for non lifting three-dimensional, arbitrary shaped bodies in a potential flow, see Subsec. (2.1.4) for details.
In the panel code developed by Newman [126], it has been considered that the panel potential can be obtained with certain geometrical relations between the panels vertices and the influencing field points which has been derived by applying the Gauß-Bonnet theorem. The assumption on bounded straight surface representations has extended the panel method to more complex geometries and for higher-polynomial order of the singularity distributions, the integration has been reduced to a possible small amount of integral evaluations.

A relevant issue in the application of the FSGF method in hydrodynamics is the non solvability of the BIEs for certain frequencies, referred as irregular frequencies. These frequencies have already been accounted in John [89] and has further been addressed in Frank [59], Ogilvie & Shin [134] and Ursell [172]. At these frequencies the numerical method's system matrix become ill conditioned due to the non-unique or trivial solution of the BIEs and the determinant of the assembled system matrix vanishes. To avoid these difficulties, several strategies exist, see e.g. Kobus [96] and Ogilvie [134]. Lee [103] and Sclavounos [106] have provided a solution that account for a superposition of the Green function and the multiplication of an imaginary constant with the Green's function derivative normal to the field point's related surface element.

For the evaluation of the FSGF, different methods has been developed from the late 1980's on. The efficient numerical methods provided by Newman and Noblesse and the solutions of hydrodynamic related issues provided by Sclavounos and Lee have been accounted in the development of the commercial code WaveAnalysisMIT (WAMIT, see [104, 130, 105]).
The double Chebyshev polynomial approach has been provided by Chen [28] and Wang [179] and has given the basis to the Bureau Veritas code HYDROSTAR.
Delhommeau [45, 46] has used interpolation within a presaved tabular to decrease the computational time for the FSGF method AQUADYN. In this code, dipoles and source distributions have been used to evaluate the unknown potential and its derivative. The open source code NEMOH has been introduced by Babarit & Delhommeau [7] and has been recently updated by Kurnia & Ducrozet [100].

The computational time of the approaches has been decreased by accounting acceleration methods. Newman [126] has extended the computational time saving farfield multipole approximation method introduced in Hess & Smith [82, 83] by using higher moments yielding an increasing accuracy for the farfield evaluation. In the multipole expansion, see Thorne [165], Korsmeyer [97], and Narbors et al. [119], the influence of two panels in far distance is evaluated in terms of replacing the farfield panel with a point source - quadripole combination whose strength is found by accounting the area and the moments of the panel of interest. For infinite water depth the method has been provided by Borgarino et al. [21]. Further approaches are the precorrected Fast Fourier Transform (pFFT) which has been used by Nabors et al. [120] and compared to the multipole expansion approach.

In terms of the analysis of moving ships with steady forward speed, the formulation of a proper FSGF is not trivial, see Newman [128]. First the wave pattern of a ship in forward speed is not axis-symmetric, so that an additional coordinate have to be accounted for the polynomial approximation of the FSGF. Additional singularities in the free surface plane at downstream to the ship location and the difficulties of finding asymptotic expansions for the farfield have been two more occurring problems. The FSGF for this problem is characterized by one double and one single integral which cover the symmetric and downstream wave pattern of the ship, respectively. Newman [127] has introduced polynomials solving the former effectively and Neumann expansion has been used for the latter, see Baar & Price [6] and related issues has been addressed in e.g. Ursell [173] and Clarisse [30]. An alternative approach is the use of the impulsive Green function to model the moving steady state source, see King et al. [94].

The developments related to FSGF approaches still continues. Eigenfunction expansion, Peter & Meylan [138], semi-analytic approaches, Delia et al. [47], global approximation, Wu et al. [185] and a second order ODE, Clément [33] and a modified ODE approach, Xie [186], have been used in FSGF methods. Xie et al. [187] have given a recent comparison in terms of accuracy and efficiency of the approaches of Wu,

Delhommeau, Telste and Noblesse as well as Newman's FSGF formulations.

The massive use of the FSGF method stands alone for the feasibility of the approach for the hydrodynamic analysis of ships and structures. The main advantages of the FSGF approach is that once the FSGF for the defined surface flow set up is known, no fluid boundary conditions have to be accounted during the computation and that the evaluation of wave-body interaction reduce to the discretization of the bodies surface and the consideration of its boundary conditions. Moreover, the evaluation of hydrodynamic coefficients can be done very effectively.

The main limitations are the inability to solve hydrodynamic problems for different environmental conditions by one general FSGF formulation. The unsolvability of the BIEs at the irregular frequencies is also an issue that has to be addressed when using the FSGF approach. Also in the analysis of moving ships with steady forward speed and the account of nonlinear wave-body interactions, FSGF approaches are limited.

This makes the method most relevant for evaluating the hydrodynamic coefficients of ships. Also, the linearized motion analysis of ships at zero or small forward speed and the load evaluation of structures, as e.g. the first- and second-order wave loads on a space fixed hydrodynamic compact offshore structures in moderate sea states, are applications well suited for FSGF approaches

1.2.2 Rankine-Source Green Function methods

The second stream of the BEMs for Marine Applications are the Rankine-Source Green Function (RSGF) methods. In a potential flow a Rankine oval or a Rankine body is known as a superposition of an uniform stream, an upstream positioned source and a downstream located sink forming an oval shaped body, see e.g. Clauss et al. [32] and Katz & Plotkin [91]. Contrastly, a Rankine-source or Rankine-singularity is in the context of three-dimensional RSGF methods the r^{-1} -type singularity, where $r = |y - x|$ is the distance between a collocation point x and a singularity y. The Green function in this method is then given by the Rankine-singularity and multiplied by a corresponding unit source strength σ

$$G(x, y)\sigma = \frac{\sigma}{|y - x|}\,, \tag{1.1}$$

see Dawson [38], Nakos & Sclavounos [123], Huang [85] and Söding & Bertram [158]. In this method the Green function does not contain any information about the free surface boundary conditions, those these methods require the discretization of both the water and the body surface.

Although Weinblum & St. Denis [182] pointed out many aspects regarding the motion of ships in forward speed already in 1950, the numerical evaluation of the wave resistance and the wave pattern around the ship hull came alongside the increasing computational power into the focus of seakeeping research in the late 1970's. Therefore, the problem of a forward moving ship in waves has been decomposed into the steady state problem, where the surrounding fluid domain is at rest, and an unsteady problem, with the ship in encountering waves. In this period falls also the development of an advanced Strip Theory Method introduced by Ogilvie & Tuck in [135] applied as an alternative to the BEM but with limitations regarding longitudinal motions due to the account of only two-dimensional ship sections.

The linearized two and three-dimensional BIE evaluation method of Yeung [193], has brought an alternative to the FSGF method for the hydrodynamic research field and is here seen as one of the conceptual starting points of both the second and third stream of BEM in Marine Hydrodynamics. Yeung has highlighted the simpler kernel function and the vanishing of the limits according to the fluid boundary conditions, which he has e.g. shown by giving finite and infinite depth results, as advantages over the FSGF approach. The increase of accuracy at smaller number of discretization segments reached by higher-order discretization has been pointed out by showing the application of basis function (he has used a linear one) for the solution space approximation in the three-dimensional case. The transformation of the Cartesian coordinates to polar respectively spherical coordinates have been used. By presenting the heave and pitch motion of a sphere and ellipsoids in three dimensions, the approach has been validated.

First contributions to the RSGF approaches are the methods of Gadd [61] and Dawson [38]. Dawson has developed a panel method based on the approach of Hess & Smith [82, 83] using a RSGF to compute

the wave resistance of and the surface elevation around bodies moving with forward velocity. To model the downstream propagation of the wave consistently, Dawson has applied an upstream finite difference operator. The double model solution has been used to simplify the free surface as symmetry line on that the body is mirrored. For the three-dimensional problem and Froude number $Fn = 0.359$, the results has indicated that at higher Froude numbers the discretization of the free surface should be considered instead of applying the double model solution.

Nakos [122] and Nakos & Sclavounos [123, 121], have used a BIE formulation with a RSGF and a frequency domain panel code to investigate the steady and unsteady seakeeping problem. For the solution of the velocity potential a bi-quadratic B-Spline basis function has been employed, allowing the solution of the panels to be influenced by the neighboring panel solutions. The error of the numerical method has been found by means of comparing the continuous and discrete operators of the problem's describing linear system in Fourier space and has been investigated in terms of numerical dispersion and stability, see also Sclavounos & Nakos [151]. To account both the uniqueness of the solution and avoid wave reflection at the boundaries of the finite domain, a radiation condition working as damping zone has been introduced. For the linearization of the free surface, the Neumann-Kelvin method and the double-hull method has been compared in terms of the wave pattern solution of steady and unsteady Wigley hull simulations. It has shown that the latter one gives more reasonable results for wave length and wave amplitude with the conclusion to favor the latter over the first one and review the use of Neumann-Kelvin linearization for the farfield approximation in hybrid methods (superposing linearized and nonlinear free surface solution in far and nearfield of the ship respectively).

Jensen [87] has calculated the steady flow around the forward moving ship by a collocation RSGF method. By iteratively solving a sequence of equations with the linearized boundary condition (see Jensen et al. [88]), the nonlinear free surface boundary condition has been approximated at the collocation points. The body surface has been discretized by triangular panels and a numerical integration has shown to be feasible after a proper transformation of the singular kernel resulting in a vanishing integral for constant source strength. Furthermore, the ship motion has been iteratively calculated based on the loads acting on the actual wetted surface of the ship hull (the surface elevation at the panels is approximated by the panel velocities) and the requirement of load equilibrium has been used for the correction of trim and sinkage. The radiation condition has been employed by an additional row of sources and collocation points at the domain behind and in front of the ship, respectively and compensates the radiated waves in the farfield. This treatment of the radiation condition results in a comparable Froude number lower limit to that in the approach of Nakos and Sclavounos (see Bertram & Yasukawa [12]). For slender ship geometries (Wigley hull and Series-60 ship), the method has shown convergent results that match with experiments. The increase of memory and computational time for decreasing Froude number and problems in convergence of the solution for a fuller ship geometry has limited the investigations.

Bertram [11] has extended the previous work of Jensen to the unsteady flow problem and has accounted the interaction with the steady problem (solved with Jensen [87]) and unsteady wave problem. Harmonically oscillating RSGFs are used to model the incident wave. The potential of the incident and diffracted waves can be decomposed in symmetric and antisymmetric parts for port-starboard symmetric geometries and allows accounting the ship by a mirror image and half the free surface discretization with respect to the ships centerline. The radiation and diffraction problem has been analyzed for a Series-60 ship hull and a submerged geometry showed reasonable results with experiments and a Strip Theory Method. The dense matrices of the linear system in Jensen [87] and Bertram [11] have been solved by Gauss Elimination schemes leading to higher computational times and memory requirements.

In [158], Söding & Bertram have introduced the three-dimensional frequency domain code GLRankine, which has been developed to analyze the wave resistance of mono hull ships in regular deep water waves at specifiable encounter frequencies ranges. Instead of an collocation approach, the patch method, in that the source strength is averaged over the panel surface, has been employed and the modification of the free surface boundary condition formulation avoid the account of higher-order derivatives therein. The discretization of the body has been done by using an unstructured triangular grid where in contrast for the free surface a block structured grid has been considered. The steady state flow has been

accounted fully nonlinear whereas the unsteady periodical flow assumptions have been linearized with respect to wave amplitude. For the radiation condition, the approach of Jensen [87] and Bertram [11] has been used. The resulting forces and moments can be evaluated globally or on specified ship sections and flow separation at the stern and rudder has been accounted. In Söding et al. [159], some extension of the method have been presented as the stabilization of the approach (due to the avoidance of the m-terms in the boundary conditions) in terms of using the steady velocity potential at body fixed coordinate system for computing the transient velocity potential and accounting viscous roll damping in the roll induced radiation moment. Results for various vessel types as passenger ferry and container ship have been presented and has shown to be well comparable with RANSE code or experiments. Only for roll motions larger errors occur, which has been related to nonlinear response of roll motion to small excitations and the linear basement of the approach.

A time domain linear RSGF method including the temporal memory effect of the hydrodynamic forces by a convolution integral, as proposed in Cummins et al. [36], has been introduced by Kring [99]. This works have given the basis for the foundation of the seakeeping code SWAN2 and has been based on the experiences with the frequency domain code SWAN1 (Nakos & Sclavounos [123, 121]), as e.g. the choice of the numerical beach as radiation condition. The forced motion case, where the load on the body surface is prescribed and hydrodynamic coefficients have been derived, and the free floating ship hull in head waves, where the body motion heave and pitch and the corresponding hydrodynamic coefficients have been integrated in a time integration scheme, has been accounted and has been analyzed in terms of numerical stability, convergence tests and has been validated by experiments and frequency domain results from SWAN1.

Nonlinear RSGF methods account for various nonlinear effects for the free surface and body boundary conditions as well as for the wave-body interaction. To name only a few of the relevant nonlinear contributions, these are at first place motion amplitudes that are not any more linearized with respect to wave amplitude and forward ship speed. Secondly roll motion which behave nonlinear to small excitation forces and furthermore, viscous effects at the rudder and the stern. This requires computation in time domain, because the linear superposition of wave component is not valid anymore if wave and body motion extend the small amplitude limit.
The difficulties in nonlinear RSGF methods lies in potentially large motion of the ship and thus large relative motions between the free surface mesh and the body mesh as well as in the occurrence of water and wave effects like spraying and wave breaking whose dominant scales requires most often a finer grid resolution, see Söding [157] and el Moctar et al. [56].

Huang [85] has introduced a nonlinear three-dimensional RSGF panel method based on an integral formulation suited for the evaluation of large amplitude wave and ship motion. The approach has been based on the weak scatterer hypothesis, which accounts nonlinear incident wave and large body motion, but only a small disturbance of the incident wave due to the body. Furthermore, the approach has been an extension of the frequency and time domain linear RSGF codes SWAN1 and SWAN2 developed by the MIT group around Sclavounos, Nakos and Kring. The amplitudes of ship response have been assumed to be small whereas the incoming wave and body amplitudes have not been limited. Nonlinear Equation has been accounted for the body motion. Wave reflection at the domain boundaries has been avoided by the introduction of a numerical damping zone. The body boundary condition has been considered over the actual wetted surface of the ship. The explicit-implicit Euler scheme has been used for time integration and the nonlinear equation of motion has been calculated with a fourth order predictor corrector method. The code validation has been done by hulls of the Series 60 ship and container ships and has indicated to agree well with experiments and has yield a significant improvement compared to linear RSGF methods.

Riesner & el Moctar [141] have developed a nonlinear time domain RSGF method based on the linear frequency domain approach presented in Riesner et al. [143] and Riesner & el Moctar [142] and GLRankine, see Söding & Bertram [158] and Söding et al. [159]. In line with e.g. Kring [99], the authors have accounted the convolution integral representing the memory effect of the flow. For the weakly nonlinear method, linearized body reactions have been accounted, while the free surface and the equation of

the rigid body motion have been treated nonlinear, the actual wetted surface of the body surface have lead to nonlinear Froude-Krylov and restoring forces and viscous effects as viscous roll damping have been considered. The method has been validated for a container ship in quartering seas up to high wave steepness and has shown well comparable results with experiments and GLRankine for the motion amplitudes. Improvements compared to the linear frequency domain approach has been indicated especially for larger wave length and increasing nonlinearity, also indicated by the Response Amplitude Operators (RAOs).

In [157], Söding has introduced a nonlinear RSGF patch method for the nonlinear analysis of symmetric monohull ships in deep water waves. The decomposition of the velocity potential of the incident wave into a disturbed and undisturbed component has allowed to damp the disturbance potential over the full computational domain (in contrast to the damping over a damping zone as in Söding & Bertram [158]) which led to the avoidance of both reflected waves from the domain boundaries and disturbance waves due to e.g. numerical errors. The undisturbed potential has remained unaffected from the damping. More specifications of the method have been the avoidance of spray and wave breaking by extrapolating the surface elevation at the ship hull from the neighboring panels, the application of the Dawson operator for ships in forward speed and the account of partly submerged body panels in terms of a decreased source strength that has been computed by using the time dependent panel submergence ratio. For the time integration, a Runge-Kutta fourth order scheme has been employed, the time derivative of the potential has been evaluated with a direct method and the free surface mesh has been updated at every time step whereas the body discretization has remained constant. To account for contributions of viscous effects as well as control, external forces and weight forces, corresponding residual loads has been incorporated in the force and moment evaluation. The method has been compared in terms of the results for e.g. linear transfer functions, torsional moment and horizontal bending moment with experiments in model scale and the linear RSGF solver GLRankine for quartering and head waves of a containership and has shown reasonable agreement with the experiments. The author has stated that the identification of a favorable method (nonlinear or linear) remain unclear from the presented results.

The Rankine Source approaches allow the evaluation of moving ships and account of nonlinearities in the water body interaction. Compared with the FSGF approach, Newman [128] has pointed out that the method is advantageous in the evaluation of fully nonlinear wave ship interaction and the evaluation of wave and wave resistance for steady state ship motions in three dimensions.
As disadvantages the evaluation of flow quantities in the farfield due to the high computational effort has been outlined in Newman [128]. Furthermore, the fulfillment of the radiation condition for small Froude numbers is non trivial.

Furthermore, the fulfillment of the radiation condition for small Froude numbers is critical due to the requirement of a higher discretization and the stabilization of the iterative solvers. To overcome the increasing number of Degrees of Freedom (DoFs) specific solutions has to be elaborated, as e.g. the linearization of the free surface and the double model solution is accounted where the bodies geometry is mirrored along the free surface plane. For starboard-port symmetric ships, the computational domain can be further simplified by using only one half of the, at the center plane dived, ship and half of the free surface domain, see e.g. Dawson [38] and el Moctar et al. [56].

1.2.3 Boundary Integral Equation Methods for Marine Hydrodynamics

The third stream of BEMs contains more general BIE formulations and are here referred as the Boundary Integral Equation methods for Marine Hydrodynamics (BIEMH). The starting points of these methods are the Green's identities and from this tailored formulations according to the application in focus are derived. Especially the coupled evaluation of unknown data of both Dirichlet and Neumann boundaries is of strong interest and make those approaches suitable for numerical wave tank implementations.

In the BIEMH group, the techniques for operator assembly, desingularization in the near and self regime, the acceleration in the farfield and further approaches are well comparable to methods used in classical BEM applications and research fields as e.g. acoustics, material science and electrical engineer-

ing.

A short review on the historical development of works related to this group indicates that the focus was first on the numerical investigations of nonlinear wave dynamics and the formation of strongly nonlinear wave events. From the end of the 90's on and with increasing computational power, the focus went more and more to nonlinear wave-body interaction that include rigid motion solver additionally, requiring an increasing number of iterations.

An early contribution to this class of BEMs next to Yeung's approach [193], has been the work Longuet-Higgins & Cooklet [112]. Therein, the Mixed Eulerian Lagrangian (MEL) approach for the investigation of nonlinear progressive waves in two dimensions has been introduced and a BIE solver has been used to find the unknown normal derivative of the free surface velocity potential, which is alongside with its tangential derivative necessary to find the material derivative of the independent quantities. Under the assumption of periodicity in space, the free surface has been transformed into a closed contour by using polar coordinate mapping. The singular integrals has been regularized by decomposing the weakly singular kernel in the near singular regime and using Taylor series to expand the normal derivative by means of the tangential coordinate around the singular point. For the integration and the evaluation of the contour, Lagrange interpolation and cubic splines has been used. The implicit Adams-Moulton multistep time integration scheme has caused instabilities at the free surface and has made a smoothing technique necessary.

In Grilli et al. [65] a two-dimensional higher-order BEM solver has been introduced. Instead of using periodic boundary conditions, a wave board motion the one end of the numerical wave tank has been defined by prescribing the paddle normal velocity whereas at the opposite side the Sommerfeld radiation condition has been accounted for the wave absorption. For the time stepping of the material free surface description, a more robust explicit method using Taylor series expansion and higher-order derivatives in space, see Dold & Peregrine [50], has been applied and has not necessitated the use of a smoothing technique. The Gauss type Berthold-Zaborowsky formula for weakly singular integrals and the double node technique at the corners of the mixed boundary value problem has been applied. The authors have presented results among others related to a plunging breaker and a solitary wave generation.

Xü [188] has developed a direct collocation BIE two- and three-dimensional solver that accounts for mixed boundary condition and have applied bi-quadratic polynomials for solution and geometry approximation (QBEM). The main focus for the application has been a numerical wave tank for modeling strongly nonlinear wave phenomena like overturning waves. Therefore, Xü has accounted and modified the MEL approach of Longuet-Higgins & Cooklet [112], e.g. in terms of numerical integration and farfield regime acceleration. The integration is performed iteratively and the order of the Gauss integration is chosen adaptively. The farfield regime integral has been evaluated by multipole expansion. Special attention has been put on the treatment of near singular regime integration, which is relevant at the curved surface and the points/lines at which Neumann and Dirichlet boundaries meet. For the latter case, the double node technique (see e.g. Lin et al. [108], Dommermuth & Yue [53]) has been applied. Here both intersecting boundaries have data, but the datum of one of these boundaries has been defined by a finite difference operator applied to the corresponding other known boundary data and its neighbors. The singularity at the curved surface is computed by accounting the triangular polar coordinate mapping (referred also as degenerate triangle mapping, see e.g. Li et al. [107]). The free surface solution has been found iteratively for that a Generalized Minimal RESidual (GMRES) solver with a Symmetric Successive Over-Relaxation (SSOR) preconditioner has been used for efficiently solving the linear system.

In Xue et al. [191], the 'Laplace solver' introduced in Xü [188] and Xü & Yue [189] and extensions, e.g. Xue [190], have been used for the analysis of breaking wave dynamics as well as the formation of crescent steep waves.

In the accompanying paper of Xue et al. [191], Liu et al. [111] have introduced the extension of the BIE solver to nonlinear wave-body interaction and have investigated the pattern of steady state bow waves and the higher harmonic excitations of a vertical cylinder in Stokes waves and the related nonlinear wave diffraction. The double node technique used already in Xü [188] has been also applied for discontinuities in the solution caused by geometrical discontinuities at the body surface. At the intersection region the

domains overlap and two collocation points, one for each domain, are given in the neighboring panels of the intersection points, with only one holding the BC. At the corresponding other one the solution is solved for.

Zhang et al. [195] have described the incorporation of the QBEM solver into the three-dimensional time domain seakeeping code LAMP (see e.g. Lin & Yue [109, 110]), later referred LAMP-QBEM. For the gain of performance and accuracy, several challenges as e.g. the automatic grid generation for QBEM panels and related misaligned collocation points at panels a corresponding handling and the robust time stepping scheme have been addressed in the paper. Positive side effects of the QBEM implementation are the straight forward evaluation of derivatives in terms of shape function derivatives instead of finite difference operators, e.g. for the gradient calculation of the velocity potential in the pressure evaluation and the continuous distribution of the pressure over the surface in terms of QBEM. The accounted verification tests have proved the faster convergence and higher accuracy after the QBEM implementation, but in the accounted comparison studies, the difference between the two methods have not shown to be significant. This has been explained by the lower importance of the dynamics in the wave-body interaction compared to the nonlinear inertia and hydrostatic forces for motions in vertical mode, heave and pitch. Contrary, scenarios where horizontal motions or combination of both modes become relevant, added wave resistance problem and capsizing events respectively, are assumed to show the relevance of a higher-order approach more clearly.

In Grilli et al. [63] the extension to three dimensions of the two-dimensional approach in Grilli et al. [65] and the incorporation of techniques for the handling of Neumann-Dirichlet boundary intersection corners, e.g. at the wave paddle, and interpolation for higher-order tangential derivatives for the Eulerian Lagrangian time integration, see Grilli & Svendsen [67] and Grilli & Subramanya [66], have been shown and allowed the investigation of three-dimensional shoaling and breaking waves. Following the approach of Grilli & Svendsen in two dimensions, the near singular cases have been identified by geometric criteria and have been regularized by subdividing the reference element into subsections on that the integration on parametric coordinates can be performed by standard Gauss-Legendre quadrature. For the weak singularities, the non-singular formulation has been found after applying the polar coordinate mapping. The authors stated that the accuracy and stability in the three-dimensional solver is most likely due to the C^2 interelement continuity of the basis function and the explicit time integration scheme.

Shao [153] has introduced higher-order BEM approaches for the analysis of weakly nonlinear wave-body interaction. Both a two-dimensional version including bi-quadratic polynomial basis functions and a three-dimensional version, accelerated by the Fast Multipole Method (FMM), have been developed and used for the study of wave radiation and diffraction of floating and fixed bodies including higher-order effects of body motion and excitation. The decomposition of the domain and the use of body fixed coordinate system in the body including domain part has saved the evaluation of m-terms and their derivatives. Regularization of the higher-order BEM solver has been done by considering the CPV integral under triangular polar coordinate mapping and both smooth and sharp edged bodies can be evaluated due to the definition of the body boundary condition at the actual body position. In [154], Shao & Faltinsen have applied the approach to linear analysis of ship motions in steady and unsteady flow and have indicated that the double body linearization have given favorable results over the Neumann-Kelvin linearization. For the stabilization of the time stepping method an upward finite difference operator for the spatial derivative in the direction of the flow has been chosen instead of the derivative of the basis function.

In the following time, the numerical wave tank of Grilli et al. [63] has been used as basis of the extension to investigate nonlinear wave-body interactions. A first contribution in this direction has been presented by Guerber et al. in [68]. Therein a two-dimensional, fully nonlinear and two way coupling BIE approach has been applied for the modeling of Wave Energy Converters (WEC). The approach accounts for two BIEs, the standard one including Dirichlet and Neumann densities of the velocity potential and a BIE for the time derivative of the velocity potential and its normal derivative. Both fulfill the Laplace equation and conditions are specified at each boundary including wave maker and absorption wave paddle. In the case of freely moving body an implicit procedure (see Tanizawa [163] and Van Daalen [174])

has been necessary due to the unknown body BC, where the Neumann condition of the potential's time derivative has been expressed by a third BIE including a regular integrand depending on bodies geometry. The method has been verified by checking the energy and volume conservation in the transient computations for fixed and freely diving cylinder. As validation case and simplified model for the WEC, the Bristol cylinder has been used as validation case within this study.

The follow up work of Guerber et al.'s work has been presented by Dombre et al. [51] and includes the widen of the application range of the two-dimensional numerical wave tank to free floating, surface piercing bodies. A new time stepping scheme with favorable energy conservation properties, has been investigated and have applied, referred as symplectic integrator like time marching procedure. Both fixed and free floating bodies has been investigated in terms of hydrodynamic forces and validated by experimental results, including large amplitude motions.

The investigation of nonlinear interaction of waves and fixed bodies and the behavior in wave radiation and diffraction have been done by Dombre et al. in [52]. As a basis, Grilli et al.'s approach [63] has been applied with modifications in terms of parallelization and time stepping. The first has allowed more efficient computations using multiprocessor units and the latter, the semi-Lagrangian method, has been developed for the analysis of vertical fixed or submerged bodies. Therein, a new definition of the material derivative including the vertical free surface position has been incorporated. Furthermore, the extension to unstructured grids have increased the flexibility in handling arbitrary hull geometries.

Harris et al. [75], see also Harris et al. [74], have further modified the numerical wave tank of Grilli et al. [63] in terms of geometry and solution representation by cubic B-splines and fast farfield evaluation by using ExaFMM (see Wang et al. [180]. For the generation and absorption of waves, most of the approach introduced in Grilli & Horrilo [64] has been implemented. The semi-Lagrangian time stepping already used in Dombre et al. [52] has been applied as well. The farfield acceleration has proven to give a significant performance increase and have allowed to analyze the presented problems of the fixed surface piercing truncated and bottom mounted cylinders in waves to be computed in a reasonable time. For the applications radial domains have been chosen , and the main focus was the evaluation of diffraction and horizontal forces on the cylinders.

In summary, the group of the BIEMH provide formulations with that case-tailored, higher-order approaches can be derived and up to strongly nonlinear dynamics be considered. In the numerical schemes, the regularization or desingularization of the singular kernels become necessary and make these approaches mathematically more challenging.

1.3 Research gap and definition of research hypotheses

In the following, the findings from the literature review are summarized , and the research gaps are identified. Based on this, the research hypotheses (RH) are defined, which are addressed within this thesis. The global hypothesis (GH) is defined as the overarching goal, which will not be reached within this work, but for that the developed methods are designed for and that will be based on the two-dimensional cBEM solver in the future perspective. The introduction concludes with an outline of the thesis' structure.

From the literature review, three main streams for the BEM in Hydrodynamics can be seen namely the FSGF, the RSGF, and the BIEMH approaches. The methods differ in terms of the applications and research questions that are in focus and in view of their specifications.
It has been shown that often specific numerical procedures have been applied to realize the practical applications as e.g. in the RSGF method the application of the Dawson operator to fulfill the radiation condition or special wave damping approaches, e.g. based on adding source points in the numerical setup.
The assumptions of the methods can be quite limiting in terms of real world applications. A common case is the linearization of wave and body dynamics which allow the analysis of the problem in the frequency domain. With the use of the FSGF and the increasing complexity of ships and structures in the forward speed limit, this approach is usually limited to small Froude numbers. In contrast, the fulfillment of the radiation condition is challenging in the RSGF methods which makes them unfavorable for smaller Froude numbers. In the BIEMH often investigations in numerical wave tanks are in focus which relate the approaches more to research than industrial applications.
In most of the methods related to the first two streams, the potential of computational efficiency has been not fully exploited and the time to perform e.g. unsteady simulations with a nonlinear RSGF code has required a high amount of computational resources. For all three BEM streams for Hydrodynamic applications, the real time capability has not been reached yet.
It has been also shown that no established time domain approach exists up to now that uses real time observations as boundary conditions for the BEM which would be one requirement for the application of the BEM in a deterministic (phase resolving) wave and motion prediction solver.
Finally, the monolithic coupling of wave and body dynamics with the incorporation of a spectral method for wave propagation is not yet accounted for in an established BEM code.

The findings from the literature review indicate that the current state of the BEM research and development for hydrodynamic applications misses some aspects which are outlined next.
First, a time domain BEM is missing that uses a fixed (no remapping in every time step) regular grid with equidistant collocation points (grid not defined by the body shape) on the free surface for the computation of wave-body dynamics by considering a mixed BVP. This would include a method for accounting for the free surface discontinuity due to the body shape and the explicit desingularization of all BIOs including the Hypersingular BIO and the setup of a robust coupling solver.
On the other hand, thereby the advantages of the HOS approach which are first and foremost the account of an arbitrary order of nonlinearity in the wave dynamic equations and the efficient solving of wave propagation could be incorporated as the HOS method rely on a computational domain with equidistantly spaced collocation points. By this, the second gap, the incorporation of an efficient approach for potentially nonlinear wave propagation in the BEM framework by a monolithic coupling approach, is identified.
The third relevant item is the lack of universality in the BEM methods, which address the limitations and specific focus of the three BEM streams. Indeed, there is no established code that provides a toolbox of methods with that all three applications can be computed.
The last two observed gaps in the existing approaches address first the computational efficiency and second the application to rigid body motion forecast. Addressing the efficiency, it can be concluded that a real time capable nonlinear time domain BEM solver is missing until now. For the forecast of e.g. ship motions in offshore operations, the application of a time domain BEM for deterministic motion prediction (alongside a suited wave reconstruction and wave propagation approach) has not yet been established.

The research and development gaps indicated the potential of innovative solutions and by defining

the following research hypotheses the red line for the development of the cBEM solver was outlined. They gave the frame for the implementation steps that had to be proven and on that basis the coupled approach was founded on.

Research hypotheses for cBEM development

RH1: By replacing the κ-operator of global support with a Hypersingular Boundary Integral Operator, the BEM solution converges to the first order HOS solution.

RH2: Let Γ be a boundary with a discontinuous manifold $\Gamma_d \subset \Gamma$ (:= a set of connected elements where no solution function is defined on) then there exist a method that can assembly two operators one for the discontinuous domain Γ_d and one for the rest of the boundary domain $\Gamma_{FS} = \Gamma \setminus \Gamma_d$ so that the union of the two operators gives a solution that is equal to the solution of the full domain.

RH3: Assume a mixed BVP that contains two separate boundary parts on that either a Dirichlet BVP or a Neumann BVP are defined and consider that a reference solution exist that employs a sufficiently differentiable analytic function to find the complete Cauchy data of the problem. Then the solution of a suited BIE system can be found by accounting the Dirichlet and Neumann boundary data at the corresponding boundary parts and the error between the solution and the analytic Neumann and Dirichlet datum of the reference is sufficiently small and converges at considerable order with increasing resolution.

RH4: Assume a mixed BVP that contains a combined boundary with a Dirichlet BVP and a Neumann BVP boundary part and consider that a reference solution exist that employs a sufficiently differentiable analytic function to find the complete Cauchy data of the problem. Then the solution of a suited BIE system with the Dirichlet and Neumann boundary data as boundary conditions at the corresponding boundary parts exist and the error between the solution and the analytic Neumann and Dirichlet datum of the reference is sufficiently small and converges at considerable order with increasing resolution.

RH5: The application of the explicit Runge-Kutta time integration scheme for the wave dynamics allows stable computations with high accuracy of submerged and surface piercing bodies in regular, small amplitude waves.

RH6: The monolithic coupling of the wave and body dynamics in time domain by using a direct BIE formulation for mixed BVPs (incorporation of all Boundary Integral Operators) in symmetric Galerkin formulation is realizable and give accurate results in hydrodynamic applications.

The derivation of the global hypothesis directly followed from the last two research gaps and highlights the future perspective targeted to be reached based on the here presented work.

Global hypothesis

GH: A real time capable time domain higher-order BEM approach that accounts nonlinear wave-body interaction and is suited for the deterministic wave and motion prediction can be developed on the basis of the coupled 2D BEM approach.

The structure of the thesis is outlined in the following. In the second chapter theoretical introductions

to the BEM and marine hydrodynamics are given. It follows the description of the cBEM solver and the related developed approaches and their verification in the third chapter. The validity of the cBEM solver for hydrodynamic applications including the surface piercing body is highlighted in the next chapter. The thesis is closed by discussing the results in terms of the defined hypotheses, drawing conclusions and giving an outline for future code developments, and possible applications.

Chapter 2

Theoretical background

After the review of applications of the BEM in ocean engineering, the focus in this section is put on the theory of BEM and hydrodynamics. Starting with the boundary value problems and their solution evaluation with BIEs, methods for the approximation of solution and geometry as well as numerical integration are discussed providing an overview of essential tools necessary for BEMs. In the second part, linear aspects for the description of surface gravity waves are summarized and the HOS method is introduced. Alongside the consideration of wave and body dynamics, corresponding governing problems are explained and characteristic parameters are presented.

2.1 Boundary Element Method

The BEM, see Katsikadelis [90], Sutradhar et al. [162], Bonnet [18] and Steinbach [161], is a widely used numerical approach for solving BIEs and is especially of interest for the efficient computation of problems with a small surface to volume ratio as e.g. contact problems, acoustics or free surface flows. The evaluation of approximative solutions for BVPs by accounting for the boundary domain and solving for boundary quantities by a BIE is the essential task in this approach. The formulation of a BVP as BIE requires the existence of a fundamental solution for the problem of interest. This exists e.g. for linear elliptic PDEs as the Helmholtz and Laplace equation.
A general difficulty in the approach is the property of the fundamental solutions and their normal derivatives to include singularities, for three dimensions of type r^{-n} with $n \in [1, 2, 3]$ and of type $\log(r)$ and r^{-n} with $n \in [1, 2]$ for two dimensions. As the fundamental solution represents the influence of two points with distance r, the influence increases drastically if the distance becomes small. Therefore, special discretization techniques that account for the singularities at the boundary have to be used.
By the use of BIEs for solving BVPs, not the original PDE is approximated but only the considered funda-

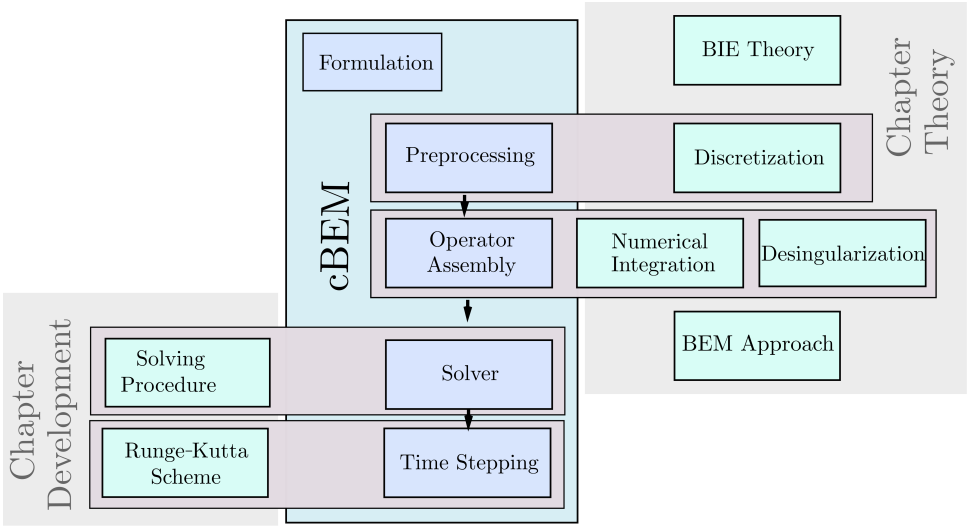

Figure 2.1: Flowchart of cBEM solver (central vertical panel) and related topics that are outlined in the next two chapters (left and right panels, gray shadowed).

mental solution. This makes the approach independent of the considered problem and having a working BEM environment allows the fast extension to other equations for that a fundamental solution exists. The account of all discretization points and their influences on each other results in dense influence matrices and make the solution finding more affordable in terms of solving techniques. For the evaluation of nonlinear problems in the BEM approach, the discretization of the volume is necessary because the volume potentials are additionally required. By this, the advantage of only considering the boundary domain vanishes and the BEM is most likely not any more favorable over other field resolving numerical approaches like the FEM. An alternative is the use of the dual reciprocity method where the fundamental solution of the simpler problem is considered and the nonlinearities and inhomogeneities are taken into account via series expansions of basis functions with global support, see e.g Partridge et al. [136].
The reduction of a field problem to a boundary problem, the straightforward account of exterior infinite problems due to the favorable characteristic of the fundamental solution to decrease rapidly with increasing distance (Sommerfeld radiation condition), the evaluation of accurate solutions for both the potential and its derivatives as well as the use of farfield approximations in FMM and pFFT resulting in very efficient solvers, make the BEM to a valuable and often favorable choice for numerical computations of BVPs.

In Fig. (2.1) the structure of the following chapters is described by showing the relations between the accounted topics and the modules in cBEM. The subjects related to the formulation, preprocessing, and operator assembly are introduced in this section and give the basis for the development steps of cBEM in the next sections. In contrast, the solver and time stepping are only briefly addressed in terms of theory. For these cBEM modules, more focus was put on the practical employment in cBEM that fit well to Sec.(3) and is discussed there. Short general introductions to the solution evaluation and the time stepping are given in the next section before describing the employment of the tools, introduced below, in practice.

2.1.1 Preparatory remarks

Hereafter, the basic assumption in terms of functional analysis and the origin of BIE and BEM is shortly and abbreviated described, for a deeper dive into the topic, the textbook of Steinbach [161] is recommended on which also the notation and review of the following paragraphs is based on. Further accounted textbooks are Hutson et al. [86] for functional analysis of BVPs, Adams & Fournier [1] for the theory of Sobolev Spaces and Sutradhar et al. [162] as reference for the symmetric Galerkin BEM.

Remarks from the perspective of functional analysis For the problem of interest it is necessary to first identify and second define properties that are relevant for finding a (unique) solution for the problem. Having identified the smoothness of functions as one of the main properties, the questions where and how the definition of smoothness can be applied has to be answered. A fast answer might be that the definition can be done on a domain and by suited function spaces with appropriate norms and characteristics. A more specific overview is given in the following, where Steinbach [161] was accounted as main reference.
The domain is defined as an open and simply connected subset of the space of n-dimensional real valued functions $\mathbb{R}^n, \Omega \in \mathbb{R}^n$ with a surrounding boundary $\partial\Omega = \Gamma$.
The function space of main interest is the Sobolev space $W_p^k(\Omega)$ defined over Ω with $k \in N_0$ and $0 \leq p \leq \infty$. This vector space is widely used in the theory of PDEs, one main reason might be that the spaces for differentiability (order k) and for integrability (order p) of the functions are both considered and the weak derivative of the function is in focus. One other, that the requirements on smoothness are relatively weak, see Hutson et al. [86]. The connection to the spaces of k times bounded and continuously differentiable functions, $C^k(\Omega)$ (and related spaces $C^\infty(\Omega)$ and $C_0^\infty(\Omega)$ as well as the space of Hölder continuous functions $C^{k,\kappa}(\Omega)$ with $\kappa \in (0,1)$), and to the space of power of p integrable functions, $L_p(\Omega)$, is indicated in the definition of the Sobolev norms. By the definition of the norms, the Sobolev Space becomes a Banach space inheriting properties as e.g. the Minkowsky inequality.
Of specific interest is the case of $p = 2$, the space of square integrable functions $L_2(\Omega)$, which is indeed a Hilbert space with the main additional property, that an inner product is given with that the space becomes a complete metric space.
The space of locally integrable function $L_1^{loc}(\Omega)$ is of interest when e.g. singular kernel function appear and the definition of an interval where the function is integrable allows to evaluate this function locally, see e.g. the CPV integral.
According to differentiability, the specific Hölder continuous function space $C^{k,1}(\Omega)$, defined as the space of $C^k(\Omega)$ functions whose k-th order partial derivatives are Lipschitz continuous functions, is of relevance because it locally constitutes the property of compactness (=bounded and closed) to the domain's boundary and ensure that finite families (of parametrizations for the boundary and the domain) exist (see Steinbach [161]). Descriptively, the property of Lipschitz continuity implies that a function has locally at all its pairs of points a connecting line whose slope has an absolute value that is smaller or equal than a real valued number, see e.g. Sohrab [160].
The Sobolev-Slobodeckij space W_p^s with the non integer order $s = k - \kappa$ and $p = 2$ is a Hilbert space and is for a Lipschitz domain referred $\forall s > 0$ as

$$W_2^s(\Omega) = H^s(\Omega). \tag{2.1}$$

The Sobolev space H^s and its duality space (defined as the space that contains all linear functionals that maps H^s to a field) are used e.g. as function space for BIEs.
Other relevant properties that are given in the Sobolev space are the Embedding theorem, the Norm Equivalence theorem and the Bramble-Hilbert Lemma, see Adams & Fournier [1], which gives relations between norms of Sobolev spaces, define equivalent norms for bounded linear functionals and provide the error of the approximation of a function by a polynomial, respectively. The possibility to approximate functions that are an element of Sobolev spaces is an additional feature that is very relevant when it comes to discretization.

For e.g. a BVP that is numerically solved by a BEM approach, the boundary is discretized in the way that

$$\Gamma = \bigcup_{i=1}^{J} \Gamma_i, \tag{2.2}$$

and it is of interest to constitute certain properties on the manifolds Γ_i of the boundary. Assuming a local parametrization $x = \chi_i(\xi)$ on every manifold, the space of this parametrization, referred as parameter

spaces, can also be chosen to be a Sobolev space $H^s(\Gamma)$ [161]. It has to be accounted that the order of differentiability s depend on (and is limited by) the differentiability class of the local representations.

The boundary can be seen as the trace of the domain. In this context, the interior trace operator is formally a linear map defined as, see Steinbach [161],

$$\gamma_0^{int} := H^s(\Omega) \mapsto H^{s-1/2}(\Gamma) \tag{2.3}$$

for $\Omega \subset \mathbb{R}^d$ with $d = 2, 3$ and $\Omega \in C^{k-1,1}$ with $1/2 < s \leq 1$ and can be used to map domain functions to the boundary. The order reduction by $1/2 = 1/p$ of the Sobolev spaces are defined by "the phenomenon that passing from functions in $W^{m,p}(\Omega)$ to their traces on surfaces of codimension 1 results in a loss of smoothness corresponding to 1/p of a derivative" (Adams & Fournier [1], p.234).
The trace operator is bounded $\forall v \in H^s(\Omega)$ by

$$||\gamma_0^{int}||_{H^{s-1/2}}(\Gamma) \leq c_T ||v||_{H^s(\Omega)}. \tag{2.4}$$

Correspondingly, an inverse trace operator can be defined that describes the linear mapping from the boundary to the domain, see e.g. Steinbach [161].
The trace operator is used to formalize the limiting process of domain quantities to boundary densities. By applying the trace operator on Double or Single layer potentials, Boundary Integral Operators (BIOs) can be defined, which play a relevant role in the theory of BIEs and are described in one of the following section.

Differential operator and weak formulation Assuming that a general form of a Partial Differential Equation (PDE) is given by [161]

$$(Lu)(x) = f(x) \tag{2.5}$$

with the linear differential operator of dimension $d = 2, 3$

$$(Lu)(x) := -\sum_{i,j=1}^{d} \frac{\partial}{\partial x_j}\big[a_{i,j}(x)\frac{\partial}{\partial x_i}u(x)\big] + a_0(x)u(x) \tag{2.6}$$

and the scalar real valued function u, the constant coefficients $a_{ij}(x)$ fulfilling $a_{ij}(x) = a_{ji}(x)$ for all $i, j = 1, ..., d, x \in \Omega$ and the function f representing an inhomogenety. Furthermore, the functions f, u, v used here and in the following, are considered to be sufficiently smooth. The exterior unit normal vector $\mathsf{n}(y)$ is given nearly everywhere for $y \in \Gamma$.

Then the weak formulation of the PDE, which one find by multiplication with a test function v and integrating over the domain Ω is given by

$$\int_\Omega (Lu)(x)v(x)dx, \tag{2.7}$$

and represent the connection between PDE and BIE.

Boundary value problem For elliptic partial differential equations, the BVP is a standard tool for the solution evaluation [161]. By the definition of boundary conditions, the problem is well-defined and a solution to the PDE can be found. The problem is additionally well posed, if an existing and uniquely defined solution depend continuously on the boundary conditions.

The list of types of BVPs and related boundary conditions contains first the Dirichlet BVP, where the boundary conditions are defined as Dirchlet densities, and the Neumann BVP, correspondingly having Neumann boundary conditions. Second the combined BVP, namely the Robin BVP, that have a combined and weighted condition of both Neumann and Dirichlet conditions, and the Cauchy BVP, that does not assume any weighting functions for the combined conditions. Last the mixed BVP, where all four

previously discussed boundary conditions may defined on the boundary, but in the way that the conditions are defined separately on disjoint decompositions of the boundary, e.g. for Neumann and Dirichlet boundary conditions, the BVP reads $\Gamma = \Gamma_D \cup \Gamma_N$.

For some applications, the complete Cauchy data of the solution $(\gamma_0^{int}u(x), \gamma_1^{int}u(x))$ for $x \in \Gamma$, are of interest. The Dirichlet and the Neumann datum, $\gamma_0^{int}u(x)$ and $\gamma_1^{int}u(x)$ respectively, can be found by deriving the corresponding BIEs with the help of Green's identities and using the direct BIE approach.

Divergence theorem and Green's identities Now, considering a vector field $f(x)$ in a reference volume Ω that is surrounded by the closed boundary Γ. The Divergence theorem, see e.g. Bronstein [24], states that the divergence in Ω equals the flux normal to Γ. This reads [161]

$$\int_\Omega \frac{\partial}{\partial x_i} f(x)dx = \int_\Gamma \gamma_0^{int} f(x) n_i(x) ds_x \quad \text{for } i = 1, ..., d \tag{2.8}$$

and defining $f(x) = u(x)v(x)$, the rule for the integration by parts is found by

$$\int_\Omega v(x)\frac{\partial}{\partial x_i}u(x)dx = \int_\Gamma \gamma_0^{int}v(x)\gamma_0^{int}u(x)n_i(x)ds_x - \int_\Omega v(x)\frac{\partial}{\partial x_i}u(x)dx. \tag{2.9}$$

Applying the rule of integration by parts to the PDE's weak formulation, Eq. (2.7) and substituting the linear differential operator, Eq. (2.6), yield Green's first identity [161]

$$\underbrace{\sum_{i,j=1}^{d} \int_\Omega a_{i,j}(x)\frac{\partial}{\partial x_i}u(x)\frac{\partial}{\partial x_j}v(x)dx}_{\text{symmetric bilinear form a(u,v)}} = \int_\Omega (Lu)(x)v(x)dx + \int_\Gamma \gamma_1^{int}u(x)\gamma_0^{int}v(x)ds_x \tag{2.10}$$

with the interior trace operator

$$\gamma_0^{int}f(x) := \lim_{\Omega \ni \tilde{x} \to x \in \Gamma} f(\tilde{x}) \quad \text{for } x \in \Gamma \tag{2.11}$$

and the interior conormal derivative

$$\gamma_1^{int}f(x) := \lim_{\Omega \ni \tilde{x} \to x \in \Gamma} \Big[\sum_{i,j=1}^{d} n_j(x) a_{i,j}(\tilde{x}) \frac{\partial}{\partial \tilde{x}} f(\tilde{x}) \Big] \quad \text{for } x \in \Gamma\,. \tag{2.12}$$

These operators represent the approach of the bulk variable $\tilde{x}$ to the boundary quantity x, $\Omega \ni \tilde{x} \to x \in \Gamma$.

Green's second identity is then given by accounting the symmetry of the bilinear form, $a(u, v) = a(v, u)$, see Eq. (2.10) from that $a(v, u)$ is found by switching the roles of the functions u and v, and gives

$$\begin{aligned} \int_\Omega (Lu)(x)v(x)dx + \int_\Gamma \gamma_1^{int}u(x)\gamma_0^{int}v(x)ds_x = \\ = \int_\Omega (Lv)(x)u(x)dx + \int_\Gamma \gamma_1^{int}v(x)\gamma_0^{int}u(x)ds_x \quad . \end{aligned} \tag{2.13}$$

Fundamental solution The existence of a fundamental solution is mandatory for finding a solution of a PDE by using the BIE approach. The Malgrange-Ehrenpreis theorem, see Ehrenpreis [55] and Malgrange [113], states that for the group of linear partial differential operators with piecewise constant coefficients a fundamental solution to the corresponding PDE exist.

By solving

$$(L_y G)(x, y) = \delta(y - x) \quad \text{for } x, y \in \mathbb{R}^d \tag{2.14}$$

in the distributional sense with the delta-distribution δ, the fundamental solution or Green function $G(x,y)$ is found, see for evaluation techniques of the fundamental solutions e.g. Steinbach [161]. Considering the Green function as test function, $v(x) = G(x,y)$, in the weak form of the PDE, Eq. (2.7), Green's second identity, Eq.(2.13), reads

$$\begin{aligned}\int_\Omega (Lu)(x)G(x,y)dx + \int_\Gamma \gamma_1^{int}u(x)\gamma_0^{int}G(x,y)ds_x = \\ = \int_\Omega (L_yG)(x,y)u(x)dx + \int_\Gamma \gamma_1^{int}G(x,y)\gamma_0^{int}u(x)ds_x \quad .\end{aligned} \tag{2.15}$$

2.1.2 Boundary Integral Equations

The BIE in combination with a well-defined BVP form the basis to find an approximative solution by an numerical approach for that here the BEM is considered. As the basis procedure to find a BIE (from the PDE over Green's identities and the use of the fundamental solution towards the representation formula) has been sketched in the previous paragraphs, in the following, the focus is to introduce a more formal BIE representation by the help of the BIOs.

Boundary Integral Operators For a homogeneous PDE with a linear elliptic partial differential operator of second order with the fundamental solution $G(x,y)$, the Single layer potential, $Sw \in H^1(\Omega)$, for a given density $w \in H^{-1/2}(\Gamma)$ and the Double layer potential, $Dv \in H^1(\Omega)$, for a given density $v \in H^{1/2}(\Gamma)$ reads for $x \in \Omega \cup \Omega^C$ with $\Omega^C = \mathbb{R}^d \setminus \Omega$, see Steinbach [161],

$$u := (Sw)(x) := \int_\Gamma G(x,y)w(y)ds_y \tag{2.16}$$

$$u := (Dv)(x) := \int_\Gamma \gamma_{1,y}^{int}G(x,y)v(y)ds_y \tag{2.17}$$

and define bounded and linear maps between the boundary and the domain Sobolev spaces

$$S : H^{-1/2}(\Gamma) \mapsto H^1(\Omega) \tag{2.18}$$

$$D : H^{1/2}(\Gamma) \mapsto H^1(\Omega) \tag{2.19}$$

under considering that the Single layer potential and the Double layer potential being solutions to the homogeneous PDE and the domain function $u \in H^1(\Omega)$ is satisfying

$$||u||_{H^1(\Omega)} = ||Sw||_{H^1(\Omega)} \leq c||w||_{H^{-1/2}(\Gamma)} \quad \text{for } w \in H^{-1/2}(\Gamma) \tag{2.20}$$

$$||u||_{H^1(\Omega)} = ||Dv||_{H^1(\Omega)} \leq c||v||_{H^{1/2}(\Gamma)} \quad \text{for } v \in H^{1/2}(\Gamma) \tag{2.21}$$

and thus bounded by a certain constant c [161].
The order of the function space $H^{-1/2}(\Gamma)$ corresponds to w being the derivative of function $v \in H^{1/2}(\Gamma)$ (differentiation reduces the order of the function space by one) and thus, the Single layer potential maps from the boundaries derivative function space to the domain whereas the Double layer potential maps from boundaries function space.

The application of the interior trace and the interior conormal derivative operators to the Single and Double layer potentials give for $x \in \Gamma$ the mapping properties (left) and the relations of the layer potentials to the corresponding BIOs (right) [161]

$$\begin{aligned}
&\gamma_0^{int}S : H^{-1/2}(\Gamma) \mapsto H^{1/2}(\Gamma) && (\mathcal{S}w)(x) = \gamma_0^{int}(Sw)(x) \\
&\gamma_0^{int}D : H^{1/2}(\Gamma) \mapsto H^{1/2}(\Gamma) && \gamma_0^{int}(Dv)(x) = [-1+\sigma(x)]v(x) - (\mathcal{D}v)(x) \\
&\gamma_1^{int}S : H^{-1/2}(\Gamma) \mapsto H^{-1/2}(\Gamma) && \gamma_1^{int}(Sw)(x) = \sigma(x)w(x) + (\mathcal{A}w)(x) \\
&\gamma_1^{int}D : H^{1/2}(\Gamma) \mapsto H^{-1/2}(\Gamma) && (\mathcal{H}v)(x) = -\gamma_1^{int}(Dv)(x)
\end{aligned} \tag{2.22}$$

with

$$\sigma(x) = \lim_{\varepsilon \to 0} \frac{1}{2(d-1)\pi} \frac{1}{\varepsilon^{d-1}} \int\limits_{y \in \Omega : |y-x| = \varepsilon} ds_y \quad \text{for } d = 2, 3 \tag{2.23}$$

and wherein the following layer potentials, again for $x \in \Gamma$,

Single layer repr. with the Single BIO $\mathcal{S}$: $$(\mathcal{S}w)(x) = \int\limits_{\Gamma} G(x,y) w(y) ds_y \tag{2.24}$$

Double layer pot. with the Double BIO $\mathcal{D}$: $$(\mathcal{D}v)(x) = -\lim_{\varepsilon \to 0} \int\limits_{y \in \Gamma : |y-x| \geq \varepsilon} [\gamma_{1,y}^{int} G(x,y)] v(y) ds_y$$

Adjoint layer pot. with the Adjoint BIO $\mathcal{A}$: $$(\mathcal{A}w)(x) = \lim_{\varepsilon \to 0} \int\limits_{y \in \Gamma : |y-x| \geq \varepsilon} \gamma_{1,x}^{int} G(x,y) w(y) ds_y$$

Hypersing. layer repr. with the Hypersingular BIO $\mathcal{H}$: $$(\mathcal{H}v)(x) = -\int\limits_{\Gamma} \gamma_{1,x}^{int} \gamma_{1,y}^{int} G(x,y) [v(y) - v(x)] ds_y$$

have been used. For the derivation of the Hypersingular representation that is given by a CPV integral, a regularization has been applied on the original BIE resulting from the conormal derivative of the Double layer potential $\gamma_1^{int}(Dv)(x)$ because the original BIE does not exist in the limit $\varepsilon \to 0$ in the CPV sense, see Steinbach [161].
The relevance of BIOs is due to their function to hold relevant properties which are related to both the mathematical framework as mapping properties and defintions regarding boundedness and ellipticity and the more practical information as which Green kernel (and thus which singularity order) has to be accounted. The mapping properties including a Dirichlet to Neumann map as well as the relationship of the operator to each other are introduced next as some examples for the properties of the operators.
For Γ being a Lipschitz boundary the BIOs are bounded for $s \in [-1/2, 1/2]$ and have the linear mapping properties

$$\begin{aligned} \mathcal{S}: &\quad H^{-1/2+s}(\Gamma) &&\mapsto H^{1/2+s}(\Gamma) \\ \mathcal{D}: &\quad H^{1/2+s}(\Gamma) &&\mapsto H^{1/2+s}(\Gamma) \\ \mathcal{A}: &\quad H^{-1/2+s}(\Gamma) &&\mapsto H^{-1/2+s}(\Gamma) \\ \mathcal{H}: &\quad H^{1/2+s}(\Gamma) &&\mapsto H^{-1/2+s}(\Gamma) \end{aligned} \tag{2.25}$$

which describes the mappings between the boundary Sobolev spaces corresponding to function and its derivative, $H^{1/2+s}$ and $H^{-1/2+s}$, respectively. For a homogeneous PDE, the bounded Steklov-Poincare operator [161]

$$\mathtt{S} := \mathcal{S}^{-1}(\sigma I - \mathcal{D}) : H^{1/2}(\Gamma) \mapsto H^{-1/2}(\Gamma) \tag{2.26}$$

relates the Cauchy data and can be used to calculate the Dirchlet to Neumann map by

$$\gamma_1^{int} u(x) = (\mathtt{S} \gamma_0^{int}) u(x). \tag{2.27}$$

Due to the relations between the BIOs [161]

$$\begin{aligned} \mathcal{S}\mathcal{H} &= (\sigma I - \mathcal{D})((1-\sigma) I + \mathcal{D}) \\ \mathcal{H}\mathcal{S} &= (\sigma I + \mathcal{A})((1-\sigma) I - \mathcal{A}) \\ \mathcal{S}\mathcal{A} &= -\mathcal{D}\mathcal{S} \\ \mathcal{A}\mathcal{H} &= -\mathcal{H}\mathcal{D} \end{aligned} \tag{2.28}$$

a symmetrization of the in general not self-adjoint (see for details on self-adjointness Hutson et al. [86]) Double BIO $\mathcal{D}$ by the Single BIO is given and the products $\mathcal{S}\mathcal{H}$ and $\mathcal{H}\mathcal{S}$ including the Hypersingular operator can be computed by using the even weaker singular Double and Adjoint operator.

Calderon projector, BIE system, CBIE and NDBIE Assuming the representation formula for the general inhomogenous PDE, Eq. (2.5), and $\tilde{x} \in \Omega$

$$u(\tilde{x}) = -\int_\Gamma \gamma_{1,y}^{int} G(\tilde{x}, y)\gamma_0^{int} u ds_y + \int_\Gamma \gamma_0^{int} G(\tilde{x}, y)\gamma_1^{int} u ds_y + \int_\Omega G(\tilde{x}, y) f(y) dy \tag{2.29}$$

and approaching the limit $\Omega \ni \tilde{x} \to x \in \Gamma$ gives the BIEs for the Dirichlet BVP and the Neumann BVP

$$\begin{aligned} \gamma_0^{int} u(x) &= (\mathcal{S}\gamma_1^{int} u)(x) + (\mathcal{D}\gamma_0^{int} u)(x) + [1 - \sigma(x)]\gamma_0^{int} u(x) + N_0 f(x) \\ \gamma_1^{int} u(x) &= \sigma(x)\gamma_1^{int} u(x) + (\mathcal{A}\gamma_1^{int} u)(x) + (\mathcal{H}\gamma_0^{int} u)(x) + N_1 f(x) \end{aligned} \tag{2.30}$$

with the Neumann potentials $(N_0 f)$ and $(N_1 f)$, see Steinbach [161]. By using the Calderon projection [161]

$$C = \begin{pmatrix} (1-\sigma)I + \mathcal{D} & \mathcal{S} \\ \mathcal{H} & \sigma I + \mathcal{A} \end{pmatrix} \tag{2.31}$$

the complete Cauchy data can be obtained from the following direct BIE system

$$\begin{pmatrix} \gamma_0^{int} u \\ \gamma_1^{int} u \end{pmatrix} = \begin{pmatrix} (1-\sigma)I + \mathcal{D} & \mathcal{S} \\ \mathcal{H} & \sigma I + \mathcal{A} \end{pmatrix} \begin{pmatrix} \gamma_0^{int} u \\ \gamma_1^{int} u \end{pmatrix} + \begin{pmatrix} N_0 f \\ N_1 f \end{pmatrix} \quad . \tag{2.32}$$

For the homgeneous PDE, $f = 0$, the right hand side terms related to the Neumann potentials in the BIE system, Eq. (2.32), vanishes and Eqs.(2.30) become for $x \in \Gamma$ the Conventional BIE (CBIE)

$$\gamma_0^{int} u(x) = (\mathcal{S}\gamma_1^{int} u)(x) + (\mathcal{D}\gamma_0^{int} u)(x) + [1 - \sigma(x)]\gamma_0^{int} u(x) \tag{2.33}$$

and the Normal Derivative BIE (NDBIE)

$$\gamma_1^{int} u(x) = \sigma(x)\gamma_1^{int} u(x) + (\mathcal{A}\gamma_1^{int} u)(x) + (\mathcal{H}\gamma_0^{int} u)(x). \tag{2.34}$$

Considering now a Dirichlet BVP with known Dirichlet data $g_D \in H^{1/2}$ the corresponding equations can be derived by using the CBIE, Eq. (2.33), and the NDBIE, (2.34), as

$$(\mathcal{S}\gamma_1^{int} u)(x) = \sigma(x) g_D(x) - (\mathcal{D} g_D)(x) \tag{2.35}$$

$$([1 - \sigma(x)]I - \mathcal{A})\gamma_1^{int} u(x) = (\mathcal{H} g_D)(x) \tag{2.36}$$

where both equations represent Fredholm equations, the latter is of second kind and the first is of first kind.
The characterization as Fredholm equations can be applied here, because the BIOs are compact integral operators. Alongside the property of being a Fredholm equation, the existence and uniqueness of the solution to the particular problem can be verified and well known strategies for the solution evaluation in terms of analytic methods exist (e.g. Neumann series) [161].
For a Neumann BVP one find correspondingly from the CBIE and NDBIE, Eqs. (2.33) and (2.34), respectively, for $x \in \Gamma$

$$(\sigma(x)I - \mathcal{D})\gamma_0^{int} u(x) = (\mathcal{S} g_N)(x) \tag{2.37}$$

$$(\mathcal{H}\gamma_0^{int} u)(x) = (1 - \sigma(x)) g_N(x) - (\mathcal{A} g_N)(x) \tag{2.38}$$

with Neumann boundary conditions $g_N \in H^{-1/2}$. Here are the roles of the Fredholm equations changes with respect to CBIE and NDBIE and the CBIE gives a second kind and the NDBIE a first kind Fredholm equation.

Direct and indirect BIE method Until here, the interior trace and conormal derivative have been applied. By accounting the exterior trace and conormal derivatives, corresponding BIEs as in Eqs. (2.22) and layer potentials and representations as in Eqs. (2.24) can be derived.
By using the interior and exterior operators, the BIEs can be formulated as exterior and interior problems, see e.g. Steinbach [161], denoted by the superscripts $^+$ and $^-$ respectively. The versions refers to the existence and validity of a solution either in the enclosed domain or the exterior domain of the boundary, see Fig. (2.2). There the approach of the exterior and interior domain quantities, Ω^+ and Ω^-, towards the boundary give the representation Eq. (2.24) valid on the corresponding boundary layer Γ^+ and Γ^-.

The direct and indirect approach, see e.g. [90], refers to different methods for the evaluation of the BIEs and differ specifically in accounting one or both of the exterior and interior layer quantities. The layer represent the limiting approach of the boundary quantities. The direct approach either the interior or the exterior layer by choosing the boundary conditions in the way that the solution at the corresponding other layer vanishes, see Antoine & Darbas [5]. In the indirect approach the solutions are subtracted and jump relations are obtained.

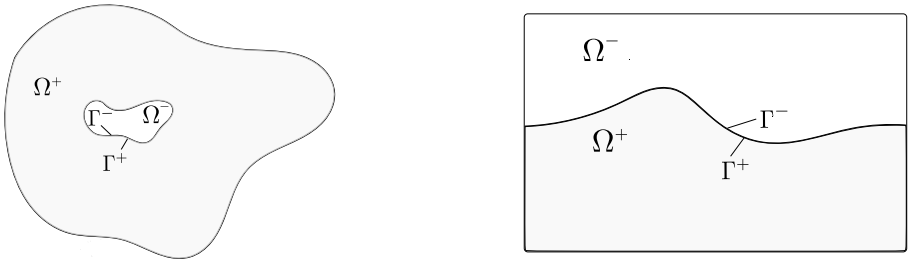

Figure 2.2: Interior and exterior layer representations, respectively Ω^-, Γ^- and Ω^+, Γ^+ by using the example of a closed boundary problem and the extension of the problem to an open boundary problem, e.g. for a two-fluid flow, separated by an interface.

The BIE system, Eq. (2.32), gives the direct approach for the interior problem. The advantages of the direct BIE is the ability to interpret the results of the BIE directly.
The unknowns are the values of the physical densities (quasi jumps of the densities assuming that either inner or outer part of the density vanishes), namely the value and the normal derivative of the value. To obtain the BIE corresponding to the problem of interest, the densities are substituted in the BIEs.
The solution of the indirect formulation gives jump relations on the boundary, also referred as sources and dipols, σ and μ respectively. The jump densities can not directly physically interpreted. The approach is based on the layer ansatz, see Fig. (2.2), in which the direct BIEs of the interior and the exterior problem are subtracted. This is represented by applying the trace γ_0 and the conormal derivative γ_1 to the Single and Double layer potentials and yield the jump relations [161] at the boundary and for $x \in \Gamma$

$$\begin{aligned}
[\gamma_0 Sw] :=& \gamma_0^{ext}(Sw)(x) - \gamma_0^{int}(Sw)(x) = 0 \\
[\gamma_0 Dv] :=& \gamma_0^{ext}(Dv)(x) - \gamma_0^{int}(Dv)(x) = v(x) \\
[\gamma_1 Sw] :=& \gamma_1^{ext}(Sw)(x) - \gamma_1^{int}(Sw)(x) = -w(x) \\
[\gamma_1 Dv] :=& \gamma_1^{ext}(Dv)(x) - \gamma_1^{int}(Dv)(x) = 0 \quad .
\end{aligned} \tag{2.39}$$

In contrast to the direct approach where the operator matrix (Calderon projector) appears on the right hand side, the operators of the indirect approach (layer potentials) appear on the left hand side and need to be inverted to find a solution in terms of jump densities. After obtaining these indirect solutions the physical values are evaluated in a second step by considering a second equation.

2.1.3 Application to Laplace equation

Since incompressible potential flows are considered here, the Laplace equation

$$-(\Delta\phi)(x) = 0 \tag{2.40}$$

is considered. In Eq. (2.40) the linear differential operator of the PDE, Eq. (2.5), is the Laplace operator $\Delta := \nabla \cdot \nabla$, with $\nabla := (\frac{\partial}{\partial x_1}, ..., \frac{\partial}{\partial x_d})$ representing the Nabla operator, acting on the velocity potential ϕ

$$(L\phi)(x) := -(\Delta\phi)(x) = -\sum_{i=1}^{d} \frac{\partial^2\phi(x)}{\partial x_i^2} \quad . \tag{2.41}$$

The weak form of the Laplace equation is then given by

$$-\int_\Omega (\Delta\phi)(x)t(x)dx = -\int_\Omega (\nabla \cdot \nabla\phi)(x)t(x)dx \quad . \tag{2.42}$$

The substitution of Eq. (2.41) in Green's second identity, Eq. (2.15), and accounting the interior trace and conormal derivative of a scalar valued sufficiently smooth function Ξ for the considered Laplace and for $y \in \Gamma$ equation to be

$$\begin{aligned} \gamma_0^{int}\Xi(y) :=& \Xi(y) \\ \gamma_1^{int}\Xi(y) :=& \frac{\partial}{\partial n_y}\Xi(y) = \mathsf{n}(y) \cdot \nabla\Xi(y) \end{aligned} \tag{2.43}$$

gives

$$\begin{aligned} -\int_\Omega (\Delta_y\phi)(y)G(x,y)dy + \int_\Gamma \frac{\partial}{\partial n_y}\phi(y)G(x,y)ds_y = \\ = -\int_\Omega (\Delta_y G)(x,y)\phi(y)dy + \int_\Gamma \frac{\partial}{\partial n_y}G(x,y)\phi(y)ds_y \, . \end{aligned} \tag{2.44}$$

The Green functions for the Laplace operator read for two dimensions [161]

$$G(x,y) = -\frac{1}{2\pi}\log|x-y| \tag{2.45}$$

and for three dimensions

$$G(x,y) = \frac{1}{4\pi}\frac{1}{|x-y|}, \tag{2.46}$$

and have the following symmetry properties in the weak, strong and hypersingular kernel [162]

$$\begin{aligned} G(x,y) =& G(y,x) \\ \nabla_y G(x,y) = -\nabla_x G(x,y) =& \nabla_x G(y,x) \\ \frac{\partial^2 G}{\partial n_x \partial n_y}(x,y) =& \frac{\partial^2 G}{\partial n_x \partial n_y}(y,x). \end{aligned} \tag{2.47}$$

By considering the potential ϕ to fulfill the Laplace equation $(\Delta_y\phi)(y) = 0$ and assuming that the fundamental solution gives a solution to the Laplace equation,

$$\int_\Omega (\Delta_y G)(x,y)\phi(y)dx = \phi(x) \, , \tag{2.48}$$

the first integral on the left vanishes and the first integral on the right simplifies respectively, and the representation formula for the Laplace equation in terms of the Dirichlet datum results in

$$\phi(x) = \int_\Gamma \frac{\partial}{\partial n_y} G(x,y)\phi(y) ds_y - \int_\Gamma \frac{\partial}{\partial n_y}\phi(y) G(x,y) ds_y \,. \tag{2.49}$$

For a solution of the Laplace equation in terms of the Neumann datum, the normal derivative $\frac{\partial}{\partial n_x}$ of Eq. (2.49) is considered and gives the representation formula for the Neumann problem

$$\begin{aligned}
\frac{\partial}{\partial n_x}\phi(x) =& \frac{\partial}{\partial n_x}\Big[\int_\Gamma \frac{\partial}{\partial n_y} G(x,y)\phi(y) ds_y - \int_\Gamma \frac{\partial}{\partial n_y}\phi(y) G(x,y) ds_y\Big] \\
=& \int_\Gamma \Big(\frac{\partial}{\partial n_x}\frac{\partial}{\partial n_y} G(x,y)\phi(y) + \frac{\partial}{\partial n_y} G(x,y)\frac{\partial}{\partial n_x}\phi(y)\Big) ds_y - \qquad (2.50) \\
& - \int_\Gamma \Big(\frac{\partial}{\partial n_x}\frac{\partial}{\partial n_y}\phi(y) G(x,y) + \frac{\partial}{\partial n_y}\phi(y)\frac{\partial}{\partial n_x} G(x,y)\Big) ds_y \\
=& \int_\Gamma \frac{\partial}{\partial n_x}\frac{\partial}{\partial n_y} G(x,y)\phi(y) ds_y - \int_\Gamma \frac{\partial}{\partial n_y}\phi(y)\frac{\partial}{\partial n_x} G(x,y) ds_y \,. \qquad (2.51)
\end{aligned}$$

With the layer potentials

$$\begin{aligned}
\Big(\mathcal{S}\frac{\partial}{\partial n_x}\phi\Big)(x) &= \int_\Gamma G(x,y)\frac{\partial}{\partial n_y}\phi(y) ds_y \qquad (2.52) \\
\Big(\mathcal{D}\phi\Big)(x) &= -\lim_{\varepsilon\to 0} \int_{y\in\Gamma:|y-x|\geq\varepsilon} \Big[\frac{\partial}{\partial n_y} G(x,y)\Big]\phi(y) ds_y \\
\Big(\mathcal{A}\frac{\partial}{\partial n_x}\phi\Big)(x) &= \lim_{\varepsilon\to 0} \int_{y\in\Gamma:|y-x|\geq\varepsilon} \frac{\partial}{\partial n_x} G(x,y)\frac{\partial}{\partial n_y}\phi(y) ds_y \\
\Big(\mathcal{H}\phi\Big)(x) &= -\int_\Gamma \frac{\partial}{\partial n_x}\frac{\partial}{\partial n_y} G(x,y)[\phi(y)-\phi(x)] ds_y
\end{aligned}$$

and the representation formulas, Eqs. (2.49) and (2.50) as well as the Calderon Projector C, Eq. (2.31), the BIE system reads

$$\begin{pmatrix} \phi(x) \\ \frac{\partial\phi}{\partial n_x}(x) \end{pmatrix} = \begin{pmatrix} (1-\sigma)I + \mathcal{D} & \mathcal{S} \\ \mathcal{H} & \sigma I + \mathcal{A} \end{pmatrix} \begin{pmatrix} \phi(y) \\ \frac{\partial\phi}{\partial n_y}(y) \end{pmatrix} \tag{2.53}$$

which can be used to find the complete Cauchy data for the Laplace problem.

2.1.4 Discretization

After choosing the BIE formulation for the given BVP, an approximative solution can be found by applying a numerical method, for that here the BEM approach is considered. The accuracy of the approximative solution depend directly on the discretization of both the geometric and the solution function spaces. This dependency might be analyzed from a theoretical and a practical point of view, where the latter tangents the specific choice of the discretization parameters in a simulation setup. The theoretical aspects include the preceding choice of the type and order of the basis functions used for the approximation of geometry and solution function space and are in the focus hereafter.

Order and type of basis functions The order of basis functions governs the decay order of the error (convergence order) at increasing number of boundary elements (h-refinement). By accounting a higher number of collocation points over the element (p-refinement), the order of the basis function

is increased, where the term control point refer to the location where the Cauchy data of the solution function are defined. In a perfect numerical setup the convergence order of a numerical solution at a higher discretization coincide with the order of the basis function.
The definition of the type depend on the support that is required for the solution space basis functions. For spectral methods the functions need to have global support and typically harmonic basis functions with periodic boundary conditions are applied, Canuto et al. [26, 25]. In the HOS method, the function ψ_p in Eq. (2.97) represent the basis function of global support. In contrast, the basis function in BEM are defined over a certain local range, the boundary elements, and have typically locally limited support, see Parag. (2.1.1). A typical choice is to use polynomials with a reasonable polynomial degree to approximate the function space at the elements. In the following, the local range of influence is used to distinguish between two types of limited support functions.

Definition 2.1.1. *(Intraelement and interelement basis functions.) Basis functions of intraelement support are defined and valid over a parametric space that is related to one element. An example in cBEM are the Lagrange polynomials that are used e.g. for the solution function space of the body.*
In contrast, the interelement basis functions refer to parametric space that represent more than one element. The number of accounted elements depend typically on the order of the applied basis function. By extending the support to more elements, the influence across neighboring elements can be modeled. The Z-Splines are used as interelement type basis functions in cBEM.

Introducing possible ways of describing functions and curves, points the way towards the application of higher-order representation of the basis functions.

Description of functions and curves

How functions and curved surfaces are mathematically described is stated in the next paragraphs after sketching the concept of parametrization and isoparametric approximation.

Parametrization Instead of describing the geometry in global coordinates, a parametric description is favorable as curved shapes simplify to straight analogous representations. In the parametric space usually the basis functions are defined over a certain interval on that the control points are distributed. The parametric mapping defines the transformation of global to parametric variables. The Jacobi matrix holds the partial derivatives of parametric and global coordinates. Its determinant, referred as Jacobian, represent the size of the element.
The isoparametric concept, originally introduced in the context of FEM, provides the same order of approximation for the solution and function space. To realize the consistent formulation the representations of functions and curves is outlined.

Polynomials Polynomials functions $p(x)$ of degree *p* are defined as the summation of factors given by coefficients a_i and variables x

$$p(x) = a_0 + a_1 x + a_2 x^2 + ...a_n x^{(n)} = \sum_{i=0}^{n} a_i x^{(i)} \tag{2.54}$$

and defined by $p + 1$ control points, see e.g. Davis & Rabinowitz [37] and De Boor[41].

The approximation theorem of Weierstrass states that every real valued, continuous function $f(x)$ with $x \in [a, b]$ can be approximated to any desired accuracy by a polynomial p. This reflects the importance of polynomials in approximation theory.

Orthogonal polynomials, as e.g. the Hermite and Jacobi polynomials, and their linear combinations can be used to approximate a wide range of functions. They can be constructed as three term recurrence relation and are considered for the construction of interpolative quadrature rules, see Subsec. (2.1.5). Assuming the polynomial p_i to be orthogonal to p_j, they are defined by the inner product

$$\langle p_i, p_j \rangle = \int_a^b g(x) p_i(x) p_j(x) dx \quad i \neq j \tag{2.55}$$

where $g(x)$ is the weight function and the indices i and j are recurrence stages. The formulation in terms of the moments of the weight function g, [37],

$$\mu_n = \int_a^b x^n g(x) dx \tag{2.56}$$

is a further property that characterizes orthogonal polynomials and useful for applications in statistics, see e.g. Sadjang [144]. Considering the weights and intervals, three examples of this polynomial class are the Legendre ($g(x) = 1, [-1, 1]$), the Chebyshev ($g(x) = \frac{1}{\sqrt{1-x^2}}, [-1, 1]$), both Jacobi polynomials, and the Laguerre ($g(x) = \exp -x, [0, \infty]$) polynomial [37]. The orthogonal basis polynomials are given usually in modal form. This indicates that each basis are directly related to one specific spectral component, see Canuto et al. [26].

Polynomial interpolation The interpolation problem to the function $\Theta(x; a_1, ..., a_n)$, see Voss [176] and De Boor [41], asks to find the coefficients a under that the interpolation conditions

$$\Theta(x_k, a_1, ..., a_n) = y_k \tag{2.57}$$

with $k = 1, .., m$ are fulfilled at control points x_k on the interval $[a, b]$.
Considering Weierstrass's approximation theorem and substituting the polynomial $\Theta(x_k, a_1, ..., a_n) \approx p(x_k)$ in Eq. (2.57), gives the interpolation condition

$$p(x_k) = y_k. \tag{2.58}$$

A practical example for applying interpolation is the evaluation of function values at locations that does not coincide with the collocation points of the solution. In cBEM this is used to locally increase the number of control points in parameter space (upsampling), so that the kernel function $f(x)$ can be approximated at higher-order m

$$f(x_n) \approx f(x_m) N_{m,n} \text{ with } x_n \geq x_m \tag{2.59}$$

where $N_{m,n}$ is the basis function containing the interpolation weights. The set of weights for a new data point represent its basis polynomial and the matrix of interpolation weights, $N_{m,n}$, describe the basis change from the original to the new points.

The Lagrange and Newton form are two basic structures that can be used for the evaluation of the interpolation problem with polynomials, see De Boor [41]. Following Voss [176], the Lagrange form of the polynom $p \in \Pi_n$

$$p(x) := \sum_{k=0}^{n} f(x_k) l_k(x) \tag{2.60}$$

with the Lagrange basis polynomial

$$l_k(x) = \prod_{i=0, k \neq i}^{n} \frac{x - x_i}{x_k - x_i} \tag{2.61}$$

with $l_k(x_l) = \delta_{kl}$ for $k, l = 0, ..., n$.
The Newton form applies divided differences, computed by the recursion formula [176]

$$[x_k] := y_k \tag{2.62}$$

$$[x_0, ..., x_l] := \frac{[x_{l+1}, ..., x_k] - [x_l, ..., x_{k-1}]}{x_k - x_l} \tag{2.63}$$

with the control points $x_0, ..x_k$ to find the coefficient a so that the function

$$f(x) = a \prod_{k=0}^{n} (x - x_k) \tag{2.64}$$

can be evaluated. Writting the polynomial p at point n can be written as

$$p_n = p_{n-1} + f(x) = p_{n-1} + a \prod_{k=0}^{n-1} (x - x_k) \tag{2.65}$$

and substituting the divided difference yield the Newton form of the polynomial

$$p(x) := \sum_{k=0}^{n} [x_0, ..., x_k] \prod_{l=0}^{k-1} (x - x_l). \tag{2.66}$$

The Newton form is more efficient in terms of floating point operations and introducing new control points can be done without calculating the basis completely new as it has to be done for the Lagrange form. But the increase of the number of control points can lead to erasures in the divided differences. Here alternative algorithms as the Neville-Aitken approach can be used, see De Boor [41] for details.
As the Lagrange form does not consider function values explicitly but only the locations of collocation points, the evaluation of the basis function $l_k(x)$ for a constant set of control points is considerably fast. Furthermore, the condition $l_k(x_l) = \delta_{kl}$ ensures that the basis functions are equal to one only at their corresponding collocation point. Thus, by multiplicating the Lagrange bases with a solution function, gives the function values at the control points explicitly: The polynomial basis is given in nodal form, in opposite to the modal description for orthogonal basis functions, see Canuto et al. [26]. This argues for choosing the control points to match the collocation points.
Both approaches consider the function $\Theta^{(r=0)}$. The evaluation of derivatives, $r \neq 0$ in the polynomial can be done by the Hermite or Hermite-Birkhoff interpolation, see e.g. Voss [176].

Error consideration and quantification A leading order error for polynomial approximation are oscillations of the solution functions increasing at the interval endpoints typically occurring for a high number of equidistant control points, see e.g. Voss [176]. The so called Runges phenomenon, referring to the oscillation shape that are similar to that of the interpolated Runge function, can be avoided by accounting unequally spaced control points as e.g. given by the Chebyshev distribution.
A possible quantification for the occurrence of such phenomena is the Lebesgue function [41]

$$\lambda_n := \sum_{i=0}^{n} |l_i(x)|. \tag{2.67}$$

It represents the basis polynomial of the Lagrange polynomial. Considering its uniform norm $||T|| := \max |T(x)| : a \leq x \leq b$ and comparing the polynomial $P_n f$ to the function f by the estimate

$$||P_n f|| \leq ||\lambda_n|| ||f||, \tag{2.68}$$

gives a measure of the interpolant to the best approximation $P_n f$, see De Boor [41]. The Lebesgue constants for Chebyshev and equidistant control point locations, given as

$$(2/\pi) \log(n+1) + 0.9625 < ||\lambda_{n,C}|| < (2/\pi) \log(n+1) + 1 \tag{2.69}$$

and

$$||\lambda_{n,eq}|| < 2^{n+1}/(e(n) \log(n)) \,, \tag{2.70}$$

shows that the measure grows exponentially for the equidistant spacing, whereas it increases only logarithmically for the Chebyshev locations with increasing number of control points n. As $||P_n f||$ must be even larger as the Lebesgue measure, Eq. (2.68), and large values indicate that the function f can no longer be approximated by $P_n f$, the Chebyshev sites are favorably for the interpolation.

The Jackson theorem [41]

$$|f(x) - p| \leq c_r \left(\frac{b-a}{n-1}\right)^r \omega_s(f^{(r)}, \frac{b-a}{2(n-1-r)}) \tag{2.71}$$

yield an upper limit for the quality of the polynomial approximation of function $f(x)$. The modulus of smoothness ω_s takes thereby the continuity of f at its r-th derivative into account.
To decrease the upper bound in Eq. (2.71), for a given function the term $(b-a)/n$ needs to be become small. This can be either done by making the interval $[a,b]$ small by introducing q subintervals, increasing n or doing both. Considering the last option and increasing nq, the polynomial unknowns increase with qn on $[a,b]$ the basis function and the degrees of freedom rise correspondingly. In contrast, by defining piecewise polynomials on the q subintervals, the basis function and complexity increase only with n for each of the polynomials [41].

The favorable properties that are related to the definition of piecewise polynomials on subintervals lead to the use of spline functions. They add continuity requirements at the intersections of the subintervals so that the support over the interval $[a,b]$ is guaranteed.

Spline functions Originally, the splines refer to thin beams of certain stiffness used typically by naval architects to find optimal curves for the description of ship hulls, see e.g. Schumaker [149]. By using lead weights the splines were fixed at control points and formed on the free sections a smooth curve that represent the condition of the spline's minimal strain energy.
In the same manner, spline functions refer to the "best interpolating function" (Schumaker [149], p. 7) that smoothly connect defined points and underly certain constraints.
Schönberg [146] has introduced the one-dimensional spline functions to describe two-dimensional curves and Holladay [84] and Walsh et al. [178] have improved the theory in terms of minimum curvature and best approximation property, see Ahlberg et al. [2]. The cubic splines has been investigated by Walsh et al. [178], Ahlberg et al. [2] and Schoenberg [147]. Three and higher-dimensional splines with the ability to represent surfaces, were introduced by Birkhoff & Garabedian [15] and further developed by De Boor [39] and Ahlberg et al. [3, 2].

Lower order representation of solution and geometry

For lower order representations of the function space, a constant or linear solution is considered. The geometry is represented by a polygonal mesh formed by quadrilateral or triangular surface elements, also referred as panels. As constant or linear basis function are used, the obtained convergence rate is maximal of first order.

Constant and linear panel methods The introduction of panel codes by Hess & Smith [82, 83] allowed a numerical analysis of BVPs in three dimensions and played, among other disciplines, a significant role in marine hydrodynamics, see various examples in Sec. (1.2.3).
Hess & Smith have used plane panels with a constant solution and for the verification of their method, computational results for the velocity distribution have been compared with analytic solutions. Among other validation cases the authors have made the connection to hydrodynamics and presented the velocity distribution on two ship hulls.
As the panel method represent a pioneering BEM approach it follows an outline of the method for solving integral equations. The unknown quantities are typically the strength of the singularities, commonly sources and doublets. An integral operator contains the summed influences of the panels to each other and the integration over the surface according to the BIE. Considering the boundary conditions yield a linear system from that the strength can be found and the loads on bodies can be derived as described in Sec. (3.2.4).
Typical applications are the flow around a submerged body or the evaluation of drag and lift coefficients for a wing profile. For the latter, the Kutta-Joukowski boundary condition is necessary because it applies a condition to the trailing edge that artificially conserve the circulation around the wing profile.
An overview of the method has been given by Katz & Korobkin [91] and specifications e.g. according to the sensitivity of the method to the number and location of panels used and the distance of the panels to each other have been outlined.
The limitations of the panel methods [91] are mainly given by the assumption of potential flow and

present if viscosity becomes relevant, e.g. if the angle of attack for a wing profile is high. The assumption of potential flow limits the lower order panel approaches, e.g. when considering the flow around profiles and vorticity and flow separation become relevant at higher angles of attack. Furthermore, the lower order representation of geometry due to the polygon mesh and the solution space restrict the accuracy of the approach. Accounting higher-order approximations, the accuracy can be improved.

Higher order approximation

Using higher-order basis functions for the solution allow evaluating an approximative solution of higher accuracy with lower resolution due to the direct relation between polynomial and convergence order. As the numerical effort increase with the number of elements, higher-order basis functions are an important factor for the gain of computational efficiency.
This can be done in panel methods by representing the singularities by higher-order polynomials. But those higher-order panel methods reach a limit in terms of accuracy and applicability as the geometry representation of arbitrary shaped surface due to a polygon mesh can not guarantee to be free of irregularities, see e.g. Katz & Plotkin [91].
Therefor, the account of the higher-order approximation for both the geometry and the solution is of interest to reach a high accurate numerical approximation. This is also reflected in the isogeometric ansatz that considers the combination of Computer Aided Design (CAD) and FEM or BEM, see Beer et al. [10].
In the following, relevant examples of higher-order approximations are given. By considering Def. (2.1.1), a sorting in inter- and intraelement support basis function is outlined. Starting with the geometry, the solution function space representation follows.

Geometry The accurate representation of the geometry has to be considered with high priority. A lack of accuracy in the geometry approximation cannot be compensated for by even the best considered accuracy in the solution.
With the focus on two dimension, the spline functions and the Bézier curves are relevant for an accurate discretization and introduced here.

Interelement type basis function The first group, the spline functions belong to the interelement type basis functions, as they are given by a set of piecewise polynomials defined over a certain subinterval for that the gradient at the subinterval intersections is considered with a certain continuity requirement. Thus, their range of validity accounts in general more than one parametric (sub)space.
The basis splines (B-Splines), introduced by [148], can represent every spline function by a suited linear combinations. Recurrence algorithms, see De Boor & [40] and Cox [35], can be applied for the evaluation of the control points. The B-splines form a minimal subset of the spline function on that certain requirements as smoothness and the degree of the parametrization can be defined.
The Non-Uniform Rational B-Splines (NURBS) introduced by Versprille [175] are widely used for geometry representation. The formulation as rational functions allow the exact representation of analytic geometries as e.g. the sphere.

Intraelement type basis function The definition and evaluation of the constraints for splines (e.g. for Hermite cubic splines in two dimensions eight conditions has to be defined) is necessary for the design of constructible structures. But in the context of free form model design, simpler geometry representations with less constraints would have been favorable.
The Bézier curves fall in this group due to their simple definition by point locations (at least two endpoints) and its gradients.
Dividing the Bézier Curve in segments (point and corresponding gradient definition), at the intersections of the subintervals no continuity requirement is defined which makes them to be members of intraelement supported basis function. Apart from the missing condition, they are closely related to the B-Splines. The Bézier curves are defined as linear combinations of Bernstein basis polynomials. The Bernstein basis are used to construct real valued polynomials with integer coefficients that have properties as positivity, symmetry and a maximum that equals one. They have been use for a constructive proof of

the approximation theorem of Weierstrass.
Introduced by de Casteljau, [42] and Bézier [14, 13] while they worked in the French car industry, these simpler approximations to the geometry founded the basis for CAD, see Prautzsch et al. [139].
It can be noted that by adding continuity constraints, the composite Bézier curves extend the class of Bézier curves to interelement type basis functions.
The extension to three-dimensional geometries and their application to the BEM have been shown e.g. in Schwarz [150]. The combination of T-Splines and Bézier patches is reasonable choice and allows the development of isogeometric BEM.

Solution function space The increase of the convergence order is due to accounting a higher accuracy for the solution description. Both types of basis functions play a role and possible favorably applications for the one or the other are given next.

Intraelement type basis function Typically, polynomials of higher degree are accounted for the increase of the approximation order. They are defined over a certain interval in parameter space and have intraelement support. For the choice of the polynomial basis, the characteristic of the function of interest has to be considered. The advantages of the Lagrange basis, see Subsec. (2.1.4), to allow efficient evaluation at constant control points makes them favorable for the farfield approximation of the BEM. The basis change for the upsampling, see Eq. (2.59), can be simply done as only the new point sites have to be known.

Interelement type basis function The use of basis functions of interelement type has the advantage to account the influence of neighboring points. Thereby, basis function of global support can be approximated which are an essential ingredient of spectral approaches. These considerations gave the basis for the coupling of the BEM and HOS approach. Of most interest hereby is the Z-Spline function.
Sagredo [145] has introduced cardinal Z-Splines which represent higher-order splines of compact support. The Z-Splines of order m, $Z_m(x)$, are defined by combining the piecewise Hermite-Birkhoff polynomials of degree $p = 2m - 1$ with the finite difference matrix. The account of the finite difference operator equips the splines with the $(m-1)$-th derivative at order m.
The most relevant property of the cardinal Z-Splines in the context of cBEM, is the convergence to the analytic sinus cardinalis function

$$\mathrm{sinc}(x) = \frac{\sin\left(\pi(x-j)\right)}{\pi(x-j)}. \tag{2.72}$$

Apart from its property to represent a perfect filter for signals by avoiding aliasing (see Whittacker-Shannon theorem), the sinc function might be interpreted as a non periodic, scaled version of the Dirichlet kernel

$$D_n(x) = 1 + 2\sum_{i=1}^{n} \cos\left(ix\right) = \begin{cases} \frac{\sin\left((n+1/2)x\right)}{\sin\left(x/2\right)} & \text{for } x \neq 2\pi i \\ 1+n & \text{for } x = 2\pi i \end{cases}, i \in \mathbb{Z} \tag{2.73}$$

with real valued variable x and degree $p = n$, see Canuto et al. [26]. The convolution of the Dirichlet function with function $f(x)$ yield its Fourier series approximation

$$(D_n * f)(x) = \int_0^{2\pi} f(y) D_n(x-y)dy = \sum_{k=1}^{n} \tilde{f}(k)\,\exp^{ikx} \tag{2.74}$$

with the Fourier transform of $\tilde{f}$ given as

$$\tilde{f}(k) = \int_0^{2\pi} f(x)\,\exp^{-ikx}\,dx. \tag{2.75}$$

In the HOS approach, Subsec. (2.2.2), Fourier series and the wavenumber vector are accounted for the evaluation of the κ-operator, see Subsec. (2.2.2) and Eq. (2.95). In that sense, the Dirichlet kernel represent a truncated Fourier series at one discrete collocation point. With their convergence properties, the use of Z-Splines as interelement basis functions therefore can mimic the Fourier series approximation that are accounted in the nonlinear wave propagation method.

2.1.5 Numerical integration

Numerical integration is essential for the evaluation of BIEs in the BEM and is done by summing up the single elements' products of integration weights and kernel function values at certain integration points. Usually the integration points are given relative to the physical space coordinates in parametric coordinates. In addition with the integration weights they form a pair of parameters that is applicable to any boundary element independent of its geometrical description. The transformation between the physical and parametric coordinate spaces is described by a mapping rule and can lead to a reduction of the dimensional order as e.g. in two dimensions the integration over a curved boundary element reduces to an integration over a straight line.
As main references both the book of Davis & Rabinowitz [37] which include a library for the evaluation of quadrature rule parameters and Voss [176] have been used.
The definition of points and weights is given by numerous quadrature rules. In the following the focus is set on the widely used group of interpolative type quadratures.

Interpolative quadrature rules

Interpolative quadratures, see [176, 37] for details, approximate the integral of the kernel function $f(x)$ by the integral of the polynomial representation $p(x)$ of this function

$$\int_a^b f(x)dx \approx \int_a^b p(x)dx = \sum_{k=0}^{n} w_k f(x_k) \tag{2.76}$$

which is given as the sum of the product of integration weights w_k and the kernel function values at subsequent integration point locations $f(x_k)$. The integration domain $[a, b]$ is discretized with n integration points.
The weights w_k are found by polynomial interpolation. Employing the interpolation with Lagrange polynomials yield the weights as

$$w_k = \int_a^b l_k^n(x)dx \tag{2.77}$$

where the Lagrange basis polynomials l_k^n are computed on the basis of the integration point locations. The order of the quadrature is $m = p + 1 = n$ where p denotes the highest polynomial degree for that exact integration is yielded. The polynomial interpolation allows to locally increase the integration order by increasing the number of integration points. By computing the corresponding basis polynomials and concatenating with the function values at the collocation points, the higher-order approximation for the integral is found. The upsampling is relevant for the integration of the kernel function in the near and self regime because close to the singularity a sufficient accurate integration requires a higher resolution of the kernel function.
The error of the approximation of the interpolative quadrature rule is given by [37]

$$\begin{aligned} E(f) &= \int_a^b f(x)dx - \sum_{k=0}^{n} w_k f(x_k) \\ &= \int_a^b (f(x) - p(x))dx \end{aligned} \tag{2.78}$$

and the evaluation of quadrature parameter sets so that the error E becomes minimal is essential in constructing quadrature rules.
There are different methods to define the integration point distribution and integration weights, and two examples of interpolative quadrature rules are described next.

Newton-Cotes type quadrature rules The Newton-Cotes formulas are a family of quadrature rules with equally spaced integration points [176, 37]. The integration weights are found by Lagrange polynomial interpolation. Thus, for any number of integration points $n \in N$ a subsequent set of points and weights can be provided.
The rules can be formulated in closed or open form, where the closed formulation imply that the interval endpoints are accounted as integration points and allow the explicit access to the endpoint values, which might be of relevance, e.g. for continuity requirements and singularity handling. As an example the C^0 continuity interelement requirement can be named, where the closed form is applied to fix the endpoint values of the neighboring elements to the same values. Vice versa, the values can also be defined as free.
In contrast, the open formulas does not include the endpoints of the integration interval. Consequently, the integral value include the interval end points by extrapolation. This estimate of the end point value might lead to errors if the function have singularities at the boundaries of the interval, but can be favorable if the derivative of the function is singular at the end points. Then, the non singular extrapolated function values represent the near regime estimate of the singular derivative and a reasonable value is found without evaluating the singularity explicitly [37].
Typical examples of closed Newton-Cotes quadratures are the Trapezoidal ($n = 1$), the Simpson's ($n = 2$) and the Simpson's 3/8 ($n = 3$) rule. The Trapezoidal rule exactly integrates polynomials up to first order (equivalent to integration order 2) and the two Simpson's rules up to cubic order. For the open formulas there exist rules for the corresponding orders, e.g. the midpoint rule ($n = 0$) exactly integrates up to linear polynomial order and the Milne's rule ($n = 4$) up to cubic polynomial order, see [176, 37].
The error for Newton-Cotes formula according to Eq. (2.78) with the equidistant spacing of the integration points h, with the $2n$-th derivative of the kernel function f is given by

$$E = e_k h^{2n+1} f^{(2n)}(\xi) \quad \text{for } a < \xi < b \tag{2.79}$$

if $f \in C^{2n}$ in [a,b]. The vector e_k contains constant factors for odd and even number of integration points for each k [37].

As in polynomial interpolation with equidistant control point distribution, Runge's phenomenon is observed if the number of integration points is high.

Gauß type quadrature rules A relevant task in terms of maximizing the accuracy of integration rules is to find quadratures which allow an exact integration for the highest possible polynomial degree. This is $p = 2n - 1$ because a quadrature with $2n$ unknowns (n points + n weights) can never exactly integrate a polynomial of degree $p = 2n$, see e.g. Davis & Rabinowitz [37].
The Gauß quadratures use polynomial weights and non equidistant points so that indeed an exact integration value can be numerically computed up to the maximal possible polynomial degree. These quadratures are open formulas and their set of integration pointsare symmetric with respect to the center of the integration interval and the weights are equal at each pair of symmetric points.
The accounted polynomials p have to be orthogonal to the solution space of the weight function $w(x)$ and can be found by solving Eq. (2.55). Accounting the orthonormal polynomial $\breve{p}_n$ with positive leading coefficient k_n, the integration weights are given as

$$w_k = -\frac{k_{n+1}}{k_n}\left(\breve{p}_{n+1}(x_k)\frac{\partial \breve{p}_n}{\partial x}(x_k)\right)^{-1} \tag{2.80}$$

at the integration points x_k so that exact integration

$$\int_a^b w(x)p(x)dx = \sum_{k=1}^{n} w_k p(x_k) \tag{2.81}$$

for polynomials up to order $p = 2n - 1$ can be realized [37].
A number of orthogonal polynomials exist and their choice of application depend on the characteristics

of the weight and the kernel function. Three examples for Gauß quadratures with different specification, see for details Davis & Rabinowitz [37], are introduced next, namely the Gauß-Jacobi, the Gauß-Legendre and the Gauß-Lobatto quadrature.
The Jacobi polynomials are orthogonal to the weight function

$$w(x) = (1-x)^{\alpha}(1+x)^{\beta} \tag{2.82}$$

with $\alpha, \beta > 1$ on the interval [-1,1]. This quadrature can be used for kernel functions with interval end point singularities.
With $\alpha = \beta = 0$, the weight function becomes $w(x) = 1$ and the corresponding orthogonal polynomials are the Legendre polynomials. The Gauß-Legendre quadrature is the most classical Gauß quadrature and lead to the exact integration of polynomials of highest maximal degree $p = 2n - 1$.
If the interval endpoint values, $f(-1)$ and $f(1)$, are known, the closed Gauß-Lobatto quadrature [37] (also Lobatto quadrature)

$$\int_{-1}^{1} f(x)dx \approx a\big[f(1) + f(-1)\big] + \sum_{k=2}^{n-1} w_k f(x_k) \tag{2.83}$$

can be applied. The polynomials are orthogonal to $w(x) = 1$ and an approximate integration can be found for kernel functions $f(x) \in C^{2n-2}$ and exact integration for polynomials up to degree $p = 2n+1$ is possible. The basis structure of Gauß rules with preassigned values is of the form

$$\int_{a}^{b} f(x)dx \approx \sum_{k=1}^{m} a_k f(y_k) + \sum_{k=1}^{n} w_k f(x_k) \tag{2.84}$$

where the first term contains predefined integration points y_k. The unknown parameters a_k, w_k, x_k are evaluated under the assumption to yield exact integration for maximal possible degree, with $m + 2n$ unknowns this is $p = m + 2n - 1$. The Radau quadrature is of the same structure but account only one of the endpoint values [37].
The above polynomials are usually defined to be orthogonal to the weight function over the interval [-1, 1], but can in general normalized to any other integration interval by a linear mapping.

The error of the n-th Gauß type quadrature according to Eq. (2.78) including the weight function can be quantified by accounting the $2n$-th derivative of the kernel function and the coefficient k_n

$$\begin{aligned} E_n(f) &= \int_a^b w(x)f(x)dx - \sum_{k=0}^{n} w_k f(x_k) \\ &= \frac{1}{(2n)!k_n^2} f^{(2n)}(\xi) \quad \text{for } a < \xi < b \end{aligned} \tag{2.85}$$

if $f(x) \in C^{2n}$ in [a,b]. Another option is the application of the Konrod extension to increase the number of integration points and find the error as the difference of two integral evaluations of varying order. The method of Konrod increases the number of integration points of a given n-point Gauß rule to $n+1$ which gives an exact integration for polynomials of degree $p = 2n + 1$ and reuse the Gauß point rule of lower order [37, 176].

As disadvantages of the Gauß type quadratures, the characteristic of the weights and points of being irrational numbers and that a change of integration points requires a complete new evaluation of integration points and weights can be named. By using modern computational capacities and routines as the Newton-Raphson methods (usually for Gauß-Legendre, extension of the classical Newton-Raphson root finding method) or the Golub-Welsch approach (use three term recurrence relation, formulation of eigenvalue problem) to find the quadrature parameters, these disadvantages do not have a high priority anymore. Additionally and as outlined above, the Konrod extension could be used as a more favorable option due to accounting the previous computed quadrature parameter sets for the evaluation of the new ones [37].

2.1.6 BEM formulation

The two main BEM formulations, the collocation and the Galerkin form are introduced next. A comparison of the two approaches and a recent overview of the symmetric Galerkin method are provided in the book of Sutradhar et al. [162].

Collocation method Collocation approaches account collocation points as locations for the solution. As the solution has to exactly fulfill the BIE at these sites, this method satisfy the equations in the strong sense. The collocation points are related to the boundary elements, the latter approximate the geometry and the first are the references for the solution. A typical choice is to consider them one-to-one, so that the grid points represent discretization and solution concurrently.
The evaluation of the integral kernels by quadrature rules require the distribution of additional integration points over the elements. The integral values have to interpolated from the integration sites to the collocation points.
For the Collocation method the solution function space requires to be C^1 continuous. The obtained BIOs are not symmetric due to the integration only the source domain is considered.
The Collocation method is used for spectral approaches, see e.g. Canuto et al. [26]. Also the variables in the HOS method are evaluated at collocation points.
A specific Collocation approach is given by the Nyström method. Here the same sites for collocation and integration points are considered. The collocation points are interpreted as point charges with strengths equal to the integration weights, see Bremer [22]. By choosing specific weights, Bremer & Gimbutas [23] have shown that the integral evaluation results in a quasi double integration over the boundary elements and thus can reduce the requirements for the boundary. Schwarz [150] has applied the Nyström approach to a frequency BEM.

Galerkin method In the Galerkin approach, see Sutradhar et al. [162], the solution of the BIE is considered to be fulfilled in the weak form. Instead of satisfying the solution at every point explicitly, the weak sense provides the solution of the BIE as weighted average. The weighting is realized by using suited basis functions of compact support as test functions. The consideration of both trial and test function for the boundary domains in the residual function, results in practice in the evaluation of double integrals. In terms of computational time, this additional integration on the target subdomain makes the Galerkin implementation in general less efficient than the collocation method.
Using the same basis functions for both function spaces (Bubnov-Galerkin) and considering the symmetry property of the Green function, see Eq. (2.47), the obtained BIOs are symmetric as well. Also for mixed BVPs and the related block matrix system, the symmetric Galerkin BEM and the symmetry properties hold for BIOs representing both the eigen and the coupling influence of the Dirichlet and Neumann boundary domains. For the coupling parts, the off diagonal operators, precisely the symmetry holds for the operator and its transposed counterpart.
The Galerkin method represents the closest approximation to the exact solution found by projecting it to the basis function spaces and is thereby of higher accuracy than the collocation method [162]. Considering the NDBIE, the solution at the boundary has to be of continuity class C^0 which lowers the requirements for the approximation of geometry and solution compared to the collocation method and the functions does not require being continuous differentiable across the elements.
Furthermore, the limit to the boundary approach and the related direct desingularization allows to apply the same evaluation procedure for all kernels and even weakens the singularity, see Bonnet & Guiggiani [19]. An overview of the symmetric Galerkin approach and its application in various research fields is given in Bonnet [16]. The symmetry property is an important feature that allows the interpretation of the BIOs in more physical manner and analogous parts in FEM and BEM can be identified. This allows a straightforward coupling of the two approaches, combining their particular advantages.
Also in spectral methods, the weighted residual form is considered, typically as Petrov-Galerkin formalism, where different basis functions for the trial and test function solution spaces are used [26].

2.1.7 Desingularization of singular integral kernels

The singular property of the fundamental solution and the occurrence of even singular versions of it in CBIE and NDBIE makes the evaluation of the BIOs challenging. Therefor desingularization approaches has to be used so that the singularities are either weakened or the expression become regular. The desingularization is relevant in the self and adjacent element regime and most challenging for the Hypersingular BIO. Various methods exist for the desingularization. An overview is provided by Sladek & Sladek [156] and Guiggiani [71] for the Collocation method, by Bonnet [18, 19] for the Galerkin method and by Faria [57] for a recent overview containing also desingularization approaches for the Galerkin and Nyström methods. In the following a selection of methods is given which aims to represent the typical strategies.

Cauchy Principal Value and Limit to the boundary approaches As general methods for the desingularization of singular integrals the CPV method and the limit to the boundary approach can be named and are described next. In the CPV method a vanishing, symmetric region with radius ε around the singular point is considered for strongly singular integrals. By integrating over the intervals [-a, ε] and [ε, b], the integral over the singular region is decomposed in two parts. Applying the limiting process, $\varepsilon \to 0$, the integral can be computed by trivial means. The CPV ansatz extract thereby the ε region around the singular point from the integration and replace the singular integral by an analytic expression. The inherently positive denominator of r^{-2} kernels is not centrally symmetric and the CPV method cannot employed for this type of singularity because the singular value diverges for positive and negative values of $r \to \infty$, see Sutradhar et al. [162].
The limit to the boundary method assumes that the solution over the boundary is continuous and include a vanishing neighborhood in the integral kernel. The limiting process is performed by considering the exterior and interior part around the boundary. The limit is taken after integration and yield to an analytic equation for the singular part. The approach has two advantages over the CVP, no region has to be extracted, and the approach is independent in terms of symmetry consideration of the kernel function and thus can be applied for all types of singularities. Based on this method, the desingularization in general symmetric Galerkin BEM is done. It's suited for straight elements, see for the SGBEM e.g. Balakrishna et al. [8, 9] and Gray et al. [62]. Furthermore, the methods allows an efficient calculation of all gradients of the boundary quantities by considering the equations of the exterior and interior trace in common, see [162].

Indirect methods In the group of indirect or regularization methods falls the integration by parts (e.g. Sirtori et al. [155] and Frangi [58] for the SGBEM) and the method based on the application of the Stokes theorem (e.g. Bonnet [17] for the SGBEM). In these class of approaches the singularity is reduced which simplifies the evaluation of the BIEs.
The interpolation of densities based on polynomials allows the regularization in terms of boundedness and singularity order and is applicable to Collocation, Galerkin and Nyström approaches and independent on kernel and dimension, see e.g. Pérez-Arancibia [137] and Faria et al. [57]. A general regularization technique for the Galerkin method and based on the requirements for the Green function has been introduced by Bonnet [16]. Here an analogous to the FEM stiffness matrix is derived for the BEM and the potential energy of the densities is used for the evaluation of regularized operator matrices.

Direct Desingularization For the here presented work, the direct desingularization approach was used. As in the limit to the boundary approach, a vanishing region around the singularity was accounted. On this region, a Taylor expansion in parameter space was performed. This separates the previously singular integral in an analytical part with explicit expressions and a regularized integral part that was suited for numerical quadrature. One of the main advantage of this method was the provision of an exact solution for the singular integral parts. For the collocation BEM this method has been developed for strongly and hypersingular integrals by Guiggiani & Gigante [72] and Guiggiani et al. [73, 70], respectively.

Direct approach for 2D Galerkin BEM

For the two-dimensional symmetric Galerkin BEM a direct approach suited for hypersingular kernels has been developed by Bonnet & Guiggiani [19] and is described in the following. This approach is exact and conserves the symmetry. The method has required essentially assumptions for the fundamental solution and continuity requirements for the density function. Related to the first requirement, the nonsingular factor $\mathcal{V}_{i,j}(\mathsf{e}, r, \mathsf{y})$ (fundamental solution has been decomposed in a singular part (r^{-2} for hypersingular kernel in two dimensions [19]) and a nonsingular part) has had to be bounded in the limiting case ($r = 0$), had symmetry properties and had to vanish for the radial derivative. Secondly, the solution functions have had to fulfill interelement C^0 continuity for boundaries with corners and have had to be in the limiting and weighted integral form $C^{0,\kappa}$ (Hölder) continuous over the element, which have lowered the requirements compared to the collocation approach for that $C^{1,\kappa}$ continuity is necessary. The direct method has been based on performing the limiting process on both the weighted BIE and the as a whole considered double integrals, which have been relevant conditions for conserving the symmetry. Furthermore, the boundary on that the BIE acts has been approximated by elements that are accounted for the double integration by means of the Cartesian product of source and target domain and its continuity might contain local irregularities in form of corners and contains the elements. The weight function has assumed to have compact support and belong to the source element domain that contains the singular point.

As in the approach for the collocation BEM, the aim has been to derive a regular and an analytical part for the singular integral, which is done by the approach of Bonnet & Guiggiani [19] in (here defined) six steps, namely the kernel function decomposition and fundamental solution definition, the weighting of the BIE and Taylor series term substitution, the conduct of the limiting process, the geometrical discretization, the derivation of the desired expressions for self and adjacent influence cases and the analysis of the occurring free terms. Some of these steps are described in the following.
The Taylor expansions of the potential and its gradient have been added and subtracted to the weighted vanishing region BIE part (either CBIE or NDBIE), have been sorted regarding the derivative order of the terms and then have been accounted for the limiting case ($\varepsilon \to 0$). The resulting integral parts either have given the desired contributions including a solid angle part or have vanished for the limiting part. The geometry has been discretized by means of geometrical basis functions, also referred as shape functions, resulting in a description of the surface by the global coordinates η and ξ. The derivation of geometrical parameters as normal, tangent and determinant of the Jacobian in the global parameter space has served as the basis for the farfield integration. For the self and adjacent regime, a parametric coordinate space has been used.
Considering the self regime case, the coordinate transformation from global to parametric coordinates (u,v) has been done after separating the square regime in two triangular regions and by applying both an affine and a triangular-to-square transformation (Duffy-like transformation). Whereas the singular cases (η=ξ) have appeared in a band around the diagonal in global coordinate space, the transformation have yield the shift of the singular cases along to coordinate axis u (v=0). In this coordinate space, a tensor quadrature rule have been used for numerical integration. By considering the Jacobi determinant of the transformation, the nonsingular factor of the hypersingular kernelfunction in parametric coordinates has been derived for the two triangular subregions and has been expanded in a first order Taylor series in v around $v = 0$. For the terms, explicit expressions have been given. These have been substituted in the hypersingular integral in parametric form and have yielded the integral parts that have been either evaluated analytically or numerically. Appearing terms that have been in the order of $\mathcal{O}(\varepsilon^{-1})$ and $\mathcal{O}(\ln \varepsilon)$ canceled each other due to the assumptions of interelement continuity.
The derivation of the direct neighboring elements desingularization has been based on the same structure. Here the singular case has appeared, if the neighboring elements have shared an endpoint. Accounting the adjacent and transposed adjacent case, the singular point has been transformed by a Duffy mapping to a line along to one of the coordinate axis with the advantage of suiting again to the tensor Gauss quadrature rule. The Jacobian has applied to the nonsingular factor of the hypersingular kernel weakens the singularity about one order so that the strongly singular kernel functions have been already regularized by this transformation. A zero-order Taylor expansion of the nonsingular factor has been suffi-

cient and substituting this into the parametric hypersingular integral version has given the desingularized terms for the neighboring elements. It has to be noted, that the two adjacent and self cases has to be accounted in common to ensure that the unbounded free terms have canceled out each other. The arise of unbounded and bounded free terms in the direct evaluation of singular integrals has been shown for the Collocation and Galerkin approach and has been assigned to the specification of the limiting process, see Guiggiani [70] and Bonnet et al. [20]. The unbounded terms have vanished, if certain assumptions (also referred as canceling conditions), e.g. in terms of continuity, have hold for the application of the corresponding BIE. In Bonnet and Guiggiani, the unbounded free terms have been derived and have been newly shown for the hypersingular BIE. The cancellation conditions for these terms have been outlined to be the interelement continuity of both the basis function for the potential and the tangent vector. Explicit expressions of these terms have been given for the isotropic and anisotropic problem. The bounded free term has a certain value if the boundary is smooth in terms of the tangent (normal) vectors. For discontinuities of the tangent vector, as it appears e.g. for corners (e.g. [70], [58] for the Collocation approach), the bounded terms have had to be evaluated explicitly and Bonnet & Guiggiani [19] have presented the integral terms for the two-dimensional Galerkin approach. A more detailed discussion on the free term considered for cBEM can be found in Subsec. (3.3.2).

2.2 Hydrodynamics

2.2.1 Potential Flow and Linear Wave Theory

The main variable that is used to describe the wave dynamics and kinematics in the Potential Flow Theory, see e.g. Clauss et al. [32], is the velocity potential ϕ. The field of this scalar variable sufficiently describes the fluid flow as its gradient gives the velocity field, and the pressure field by considering the time derivative additionally. The descriptiveness of this variable might be increased by considering the direct relation to the stream function: the velocity potential's isolines are perpendicular to the stream lines of the flow. By considering the Laplacian of the velocity potential for two-dimensional problems

$$\Delta\phi = \frac{\partial^2\phi}{\partial x^2} + \frac{\partial^2\phi}{\partial z^2} = 0 \tag{2.86}$$

the fluid is described as non-viscous and the flow as incompressible and irrotational. This three assumption define the characteristics of the Potential Flow Theory that differentiate to the Euler equation by the non-vorticity.

The velocity potential, see e.g. Mei et al. [115], is given by

$$\phi(x,z;t) = -\frac{\hat{\eta}g}{\omega}\exp^{i(kx-\omega t+\varphi)}\exp^{kz} \tag{2.87}$$

with the wave amplitude $\hat{\eta} = \varepsilon/k$, the wave steepness ε and the phase shift φ between single waves.

To describe a bulk of fluid in a domain of interest, the boundary conditions are essential. Especially the conditions at the free surface are crucial as they give the velocity potential and the surface elevation, which are linked to the formation of surface gravity waves. Both the dynamic (pressure condition at the free surface) and kinematic (motion is only tangential to the free surface boundary) boundary conditions describe the free surface behavior and are given by

$$\frac{\partial\phi}{\partial t} + g\eta + \frac{1}{2}(\nabla\phi\nabla\phi) + \frac{p_a}{\rho_W} = 0 \tag{2.88}$$

$$\frac{\partial\eta}{\partial t} + \frac{\partial\eta}{\partial x}\frac{\partial\phi}{\partial x} - \frac{\partial\phi}{\partial z} = 0 \tag{2.89}$$

at the free surface $z = \eta(x;t)$, see Mei et al. [115]. The Nabla operator of the velocity potential in two dimension is $\nabla\phi = grad\phi = (\frac{\partial\phi}{\partial x}, \frac{\partial\phi}{\partial z})^\mathsf{T}$ and p_a is the atmospheric pressure at the free surface, ρ_W the water density and g the gravity of earth.

At the bottom and walls of the accounted fluid domain, the fluid flows only tangential to the surface so that the derivative of the velocity potential normal to the boundary surface vanishes

$$\frac{\partial \phi}{\partial n} = 0. \tag{2.90}$$

Under the assumption of small amplitude and thus low steepness waves, that are given at large wave length to wave height, $\lambda >> H$, and large water depth to wave height, $D >> \lambda$, (deep water condition, also $kD >> 1$) ratios, the free surface variables are sufficiently represented by their values at the linearized free surface, represented by the still water level $z = 0$. This approach is referred as Airy theory, Airy [4], or Linear Wave Theory (LWT) and the still water variables are found by the linearization of Eqs.(2.88), see e.g. Clauss et al. [32],

$$\frac{\partial \phi(x,0;t)}{\partial t} = -g\eta(x;t) \tag{2.91}$$

$$\frac{\partial \eta(x;t)}{\partial t} = \frac{\partial \phi(x,0;t)}{\partial z}. \tag{2.92}$$

The linearization of the wave dynamics allows applying the principle of superposition of single regular waves with different wave frequency, which is of interest to represent natural, irregular sea states. For the composition of such wave systems, the amount of energy at every wave frequency gives the sea state specific wave spectrum. To switch between the representation in frequency and space domain, the Fourier transform can be applied under the assumption of linearity. The Fast Fourier Transform (FFT, Cooley & Tukey [34]) allows to perform the convolution very efficiently and evaluations of wave-body interaction for different frequencies can be done with small computational effort. This gives the RAO and in addition with the sea state specific wave spectrum, the motion of ships can be determined in a statistical manner.

It has to be noted that for nonlinear wave dynamics the interaction between the single regular waves is a relevant mechanism and the superposition principle is not any more applicable. The FFT can not applied to fully resolve the wave dynamics and mode coupling between the wave components has to be considered.

The linearized Potential Flow Theory is a sufficient approximation for a wide range of applications in hydrodynamics for ships and offshore structures. To frame the range of its applicability first the validity of the potential flow assumption and second the low steepness criterium has to be reviewed for the considered cases. The latter is dominated by the wave to fluid characteristic whereas the first accounts additionally the dimensions of the considered body. Some nondimensional parameters help to quantify, if the first order theory is applicable.

Non dimensional wave parameters The potential flow for wave-body interaction can be considered (the viscosity of the flow can be neglected) either if the characteristic length of the structure a compared to the wave length λ, $2a\pi/\lambda$ (diffraction parameter), is sufficiently large or if the ratio of drag to inertia forces is small. The latter criterium is quantified by the Keulegan-Carpenter number, Keulegan et al. [92],

$$KC = \frac{u_0 T}{2a} \tag{2.93}$$

with the velocity amplitude u_0 and the wave period T. This ratio of drag to inertia force ratio becomes for deep water the ratio of the circumstance of the particles' motion orbit to the structural dimension $KC = \frac{\pi\hat{\eta}}{2a}$, see e.g. Clauss et al. [32].

In certain ranges of the diffraction parameter and KC number the Potential Flow Theory is extended by terms that consider e.g. the missing effect of viscosity, see e.g. Chakrabarti [27].

Wave variables To introduce some relevant variables for describing surface gravity waves in space and time, the wavenumber $k = \frac{2\pi}{\lambda}$ and the angular wave frequency $\omega = \frac{2\pi}{T}$ linked by the linear dispersion relation

$$\omega = \sqrt{gk \tanh(kD)} \tag{2.94}$$

are named. The dispersion of waves, an essential characteristic for surface gravity waves, describes the changing wave velocity at different wave frequencies and give the velocity quantities of phase speed $c_p = \frac{\omega}{k}$ and the group velocity on that the wave energy is transported $c_{gr} = \frac{\partial \omega}{\partial k}$. For deep water, the group velocity becomes $c_{gr} = \frac{g}{2\omega} = \frac{c_p}{2}$.

2.2.2 High-Order Spectral method

The HOS method, developed by Dommermuth & Yue [53] and West et al. [184] independently, is a numerical approach based on Potential Flow Theory that allows to evaluate nonlinear wave dynamics up to an arbitrary both order of nonlinearity n and number of wave modes m. The approach is a direct evaluating method for the Zakharov equation [194] and the mode coupling approach, and solves the Laplace equation by considering an initial BVP. The efficient computation is realized by evaluating the nonlinear products of the wave variables in physical space and calculating the derivatives by the FFT (linearly scaling with order n and mode m), also referred as pseudo spectral approach. In this context, the surface Laplacian $\Delta_x = (\nabla_x^2 + \nabla_y^2)$ is of significance as it relates the vertical derivative of any function $f(x)$ to the Fourier transform of the function $\tilde{f}(k)$ in wavenumber space. This has been represented in West et al. [184] by the vector identity

$$\begin{aligned} \kappa^2 f(x) &= -\Delta_x f(x) \\ &= \int (k_x^2 + k_y^2) \tilde{f}(k) \exp^{ik \cdot x} d^2k \end{aligned} \tag{2.95}$$

with $\kappa = \frac{\partial}{\partial z}$ and the wavenumber vector k, which has given two options for the calculation of the second vertical derivatives (either by FFT or by using finite differences). The favorable one for the efficient numerical evaluation of κ has been outlined by West et al. [184] to be the FFT as it has first used also for odd vertical derivatives and second the finite difference evaluation has shown to differ significantly from the FFT result at higher frequencies.

The relevant quantities of interest are the free surface velocity potential $\phi_S = \phi(x, z = \eta, t)$ (here for a two-dimensional computational domain) and the surface elevation η for that nonlinear evolution equations, see Zakharov [194], are established. This is done by applying higher-order expansions and identifying the nonlinear wave-wave interaction as eigenfunctions in the spectral domain.

Based on the Taylor expansion in the vertical coordinate around the still water level, the free surface velocity potential ϕ_S can be computed from the linearized ($z = 0$) modal velocity potential ϕ^m by

$$\phi_S(x;t) = \sum_m \sum_n \frac{\eta^n}{n!} \kappa^n \phi^m(x, 0; t). \tag{2.96}$$

As in mode coupling approaches, the linearized velocity potential $\phi^m(x, 0, t)$ is given, under the assumption that the Dirichlet free surface condition is satisfied in each mode m, by

$$\phi^m(x, z; t) = \sum_p^\infty \phi_p^m(t) \psi_p(x, z). \tag{2.97}$$

in terms of the free (linear, non coupled) wave mode expansion or modal amplitudes $\phi_p^m(t)$ and the global eigen or basis functions ψ_p with the number of wave modes p. Depending on the fluid constraints, the basis functions have specific formulations, for deep water in two dimensions it yields

$$\psi_p = \exp(|K|_p z + i|K_p|x), \tag{2.98}$$

where K_p denotes the modal wavenumber vector, see Mei et al. [115] for details.

By applying the chain rule to the surface velocity potential, Eq. (2.96), for the time and space derivatives

$$\frac{\partial \phi_S}{\partial x} = \frac{\partial \phi(x,\eta;t)}{\partial x} + \frac{\phi(x,\eta;t)}{\partial z}\frac{\partial \eta}{\partial x} \tag{2.99}$$

$$\frac{\partial \phi_S}{\partial t} = \frac{\partial \phi(x,\eta;t)}{\partial t} + \frac{\phi(x,\eta;t)}{\partial z}\frac{\partial \eta}{\partial t} \tag{2.100}$$

and substituting the obtained equation into the coupled dynamic and kinematic boundary conditions, Eq.(2.88), the evolution equation for the modal variables ϕ_S and η gives

$$\frac{\partial \phi_S}{\partial t} = -g\eta - \frac{1}{2}\frac{\partial \phi_S}{\partial x}\frac{\partial \phi_S}{\partial x} + \frac{1}{2}\Big(1 + \frac{\partial \eta}{\partial x}\cdot\frac{\partial \eta}{\partial x}\Big)\mathsf{W}^2 + \frac{p_a}{\rho_W} \tag{2.101}$$

$$\frac{\partial \eta}{\partial t} = -\frac{\partial \eta}{\partial x}\frac{\partial \phi_S}{\partial x} + \frac{1}{2}\Big(1 + \frac{\partial \eta}{\partial x}\cdot\frac{\partial \eta}{\partial x}\Big)\mathsf{W} \tag{2.102}$$

in terms of the vertical velocity on the free surface [115]

$$\mathsf{W} = \frac{\partial \phi_S(x;t)}{\partial z} = \sum_m \sum_n \frac{\eta^n}{n!}\sum_p^\infty \kappa^{n+1}\phi_p^m(x,0,t)\psi_p(x,0). \tag{2.103}$$

As the Laplace equation has a solution if the dynamic and kinematic boundary conditions on the free surface are known, the surface elevation and surface velocity potential are used to calculate the modal amplitudes of certain orders and subsequently the vertical velocities. By substituting the results in the coupled evolution equation, the boundary condition at certain time instant are obtained. In contrast to Eq. (2.88), the standard time evolution of the potential and the elevation, Eq. (2.101) contains only free surface quantities and integration in time yield directly the free surface variables at the new time step.

Linear water waves are represented by harmonic functions, for which the series expansion is the Fourier series and the eigenfunctions are sines and cosines. The expansion coefficients are constant and represent the amplitudes of independent waves. In contrast, the expansion coefficients are non constant in nonlinear systems, see West et al. [184] and Dommermuth & Yue [53]. The nonlinearities are interpreted as scattering and couplings of the free modes. The series of nonlinear products of modal amplitudes, represents the nonlinear version of the Hamiltonian and affect the amplitudes and the phases of the linear waves. Compared to the harmonic changes in the linearized system, the nonlinear variations are characterized by much slower time scales.

According to Mei et al. [115], the number of free wave modes typically accounted in the HOS method are $\mathcal{O}(1000)$ compared to $\mathcal{O}(10)$ free modes accounted in the Zakharov equation [194] and the mode coupling approach. But other than in the mode coupling models, the HOS method does not treat the resonant and non resonant interaction separately. Furthermore, the spectral approach converges up to a wave steepness of $\varepsilon \approx 0.357 \approx 0.8 \times (0.142 \times \pi)$, thus breaking wave are not in focus. For the use of the spectral approach necessarily the periodic boundary conditions are a relevant limitation and the occurrence of aliasing errors has to be considered.

Nevertheless, the approach is a well established tool for modeling broad banded ocean waves and analyzing nonlinear wave dynamics.
An open source version of the HOS method, HOS ocean, has been published by Ducrozet et al. [54].

2.2.3 Wave-body interaction

The interaction of wave and body dynamics has been studied extensively throughout the twentieth century in terms of experiments, analytical models and numerical codes. The understanding of the coupled dynamic system from analyzing experiments and getting solution for mathematical simplified models for the dominant mechanisms were focused on the first half of the century. With increasing computational

power the design of numerical codes came on the table, see Sec.(1.2.3) and until today either the geometrical dimension (larger and more complex geometries) or the degree of freedom (more complex and more physics) were increased. This gave new questions on more specific problems and their solution brought an even more specific understanding to the problem.

The focus in this thesis is on the development of a two-dimensional linearized solver as described by the research hypothesis. The hydrodynamic problems that have been accounted for its validation represent simplified and specific cases. The identification of such cases will be done in the following section.

Newman [129] has described the mechanisms of wave-body interaction and has detailed the procedure of solving the wave-body interaction problem. The equation of motion is taken here as starting point. On the left side of the equation, the body motion is represented in terms of acceleration, velocity and displacement. Specific to the problem and the considered complexity, the body parameters as mass, damping and stiffness in addition with the analogous hydrodynamic coefficients added mass, damping and hydrostatic restoring are accounted. Sorting the coefficients to the corresponding motion component completes the body related part of the motion equation.

On the right side, the excitation forces that cause the body motion appears. These forces can be caused by waves, wind and other external forces as crane loads, shallow water effects or current. The excitation forces are categorized in terms of their effect to the coupled wave-body dynamics. The first component, the Froude-Krylov force, reflect the effect of the undisturbed wave on the body. The radiation component represent the wave system that appears from the motion of the body. The diffraction part covers the modification of the incident wave due to the presence of the body. Excitation forces that depend on both radiation and diffraction components are of second order and treated as nonlinear effects.

Linearization Under the assumption of small amplitude motions, the equation of motion (EoM) can be linearized. The radiation and diffraction problem can be accounted as individual contributions. In the case of a steady-state oscillatory motion without current or forward speed, the memory effect of the pressure fields vanishes.

This makes both the radiation and the diffraction problem favorable for validation test cases with cBEM. They are outlined in more detail below.

Wave radiation and diffraction

The radiation problem, see e.g. Newman [129], is represented by the forced oscillation of a rigid body around its equilibrium position in calm water. The motions of the body induces waves that are radiated away from the body. The radiated waves amplitude decrease with increasing distance from the body and represent the damping of the bodies induced kinetic energy due to the surrounding water.

The radiation excitation load on the body surface can be decomposed into an inertia and pressure load component. The acceleration related inertia component is proportional to the added mass, a portion of mass that is added to bodies mass and equal to the mass of the displaced body. The first pressure load depends on the velocity induced damping of the body. The second component is the restoring due to hydrostatics. The induced pressure loads due to radiation can be seen as work on the wetted body surface to restore the stable equilibrium respectively damp the body motion. The radiation load is independent on the incident wave characteristics, but depend on the geometry of the body and acts due to the motion of the body in the fluid. The evaluation of the force components is done by accounting the complex force transfer function (transfers excitations to forces) for radiation which is found by summing the coefficients for frequency dependent added mass and damping, multiplied with the related complex wave frequency component, and the restoring coefficient.

The diffraction of the incoming waves, see e.g. Newman [129], by the presence of the fixed body in its equilibrium position cause a disturbance of the surrounding wave system and describes the diffraction problem. It results in a diffraction excitation load on the submerged body surface. The magnitude of the

force in each motion component/mode depend on the wave amplitude and the complex force transfer operator for diffraction which is a function of the encounter frequency and the wave length. The frequency of encounter is found by the wave frequency and bodies speed, and its direction relative to the main wave field.

Frequency and time domain approaches

The linearized equations for the wave-body dynamics are often computed with frequency domain approaches, see e.g. Price & Bishop [140] and for applications to ocean engineering Clauss et al. [32]. Using the principle of superposition, the reaction of the body (left hand side of EoM) due to single wave frequency components (right hand side of EoM) can be added. For the left side the body parameters and the hydrodynamic coefficients must be known. These can be found either by model tests or for simple geometries by tabulated coefficients, but nowadays most commonly by numerical methods, e.g. the BEM.

The RAO represent the unit amplitude ratio of motion reaction to excitation and is found by inverting the EoM's left hand side to the excitation force operator. The RAO gives a very efficient tool as the (square of the) motion response can be statistically determined by concatenating the square of the RAO with an irregular wave spectrum. As the evaluation with the RAO is very efficient, the approaches are widely used in marine hydrodynamics.

Considering nonlinear dynamics in the interaction of waves and body motion, the assumption of summing up regular wave components to form irregular sea states is not valid anymore. The equation of motion has to be integrated in time so that the nonlinear wave-wave and wave-body interactions can be appropriately resolved.

Chapter 3

Development of the coupled Boundary Element Method

The outcome of the introduction section indicated that the BEMs applied to marine hydrodynamics focused on:

- the radiation and diffraction analysis of ships and structure in calm water (frequency domain, linearized),
- the seakeeping analysis of ships with forward speed in steady and regular waves (frequency domain, linearized),
- ships in forward speed in irregular and steep waves with nonlinear response of the ship (time domain, nonlinear wave (non)linear body interaction),
- numerical wave tanks for investigation of steep and overturning waves (BIEMH, highly nonlinear wave dynamics, Euler-Lagrange time stepping, either wave paddle and damping zone or periodic BCs),
- the nonlinear wave-body interaction in numerical wave tanks (BIEMH, nonlinear wave linear body interaction, Euler-Lagrange time stepping, either wave paddle and damping zone or periodic BCs).

and lack :

- a direct coupling formalism of HOS and Galerkin BEM for the computation of mixed BVPs,
- an explicit account and handling of discontinuities in boundary domains by incorporating the symmetric Galerkin approach,
- an iterative solving procedure for a coupled problem based on symmetric matrices and block matrix inversion,
- the direct desingularization of singular kernels for mixed BVPs including the case of the Hypersingular BIO,
- a basis for real time capable computations of wave-body interaction in three dimensions,
- a concept of a time domain, nonlinear solver for deterministic wave and motion prediction on the basis of radar measurements and
- a flexible approach with that a more wider spectrum of applications can be covered.

In the global hypothesis, a solver is accounted that close these gaps. With the development of cBEM, the necessary basic requirements for the realization of the global hypothesis, formulated in the research hypotheses, were tested in two dimensions.
In the following, an overview of the concept, the development and implementation steps as well as on the verification procedure of operators and methods is presented. The detailed descriptions of the main parts of the solver are given thereafter.

3.1 Overview of the cBEM development

Recalling the hypothesis that a real time capable deterministic motion prediction solver can be developed on the basis of a coupled BEM approach, the main question was how to efficiently solve for body motions in a real marine environment. It was assumed that the sea state exceeds the linear conditions which made the incorporation of a solver that captures nonlinear deterministic wave dynamics necessary. The input for the wave solver would be based on radar measurements so that the information of the sea state at a location within the radius of 1-2 km from the ship are implicitly given for the waves that are propagated to the location of the ship. For the realization of a wave and motion prediction that meet the industry requirements, the approach would require to solve faster than real time.
With this in mind, an approach was chosen that computes the dynamics of waves and bodies in a coupled solver. With the body in the free surface, a new boundary domain was formed containing the immersed body and the free surface. The discontinuous parts of the boundary domains were no longer considered in the BIOs.

Definition 3.1.1. *(Discontinuity of a boundary, DCB, FSB.) A boundary discontinuity is a subset of a boundary $\Gamma_{disc} \subset \Gamma$ that contains connected elements. The discontinuous boundary (DCB) is surrounded by their complement subset $\Gamma^C = \Gamma \setminus \Gamma_{disc}$. Considering the water domain to be discontinuous, the boundary Γ^C is referred as free surface boundary (FSB).*

This requires the treatment of the boundary intersection and primarily made specific desingularization methods for BIOs of the mixed BVP necessary.

Level 1: Free Surface BEM (fsBEM) As the HOS method is an efficient approach for nonlinear wave dynamics of arbitrary order and suited for wave steepness below the breaking limit (see Subsec. (2.2.2)), this method had been chosen for wave propagation. The computation domain of spectral approaches

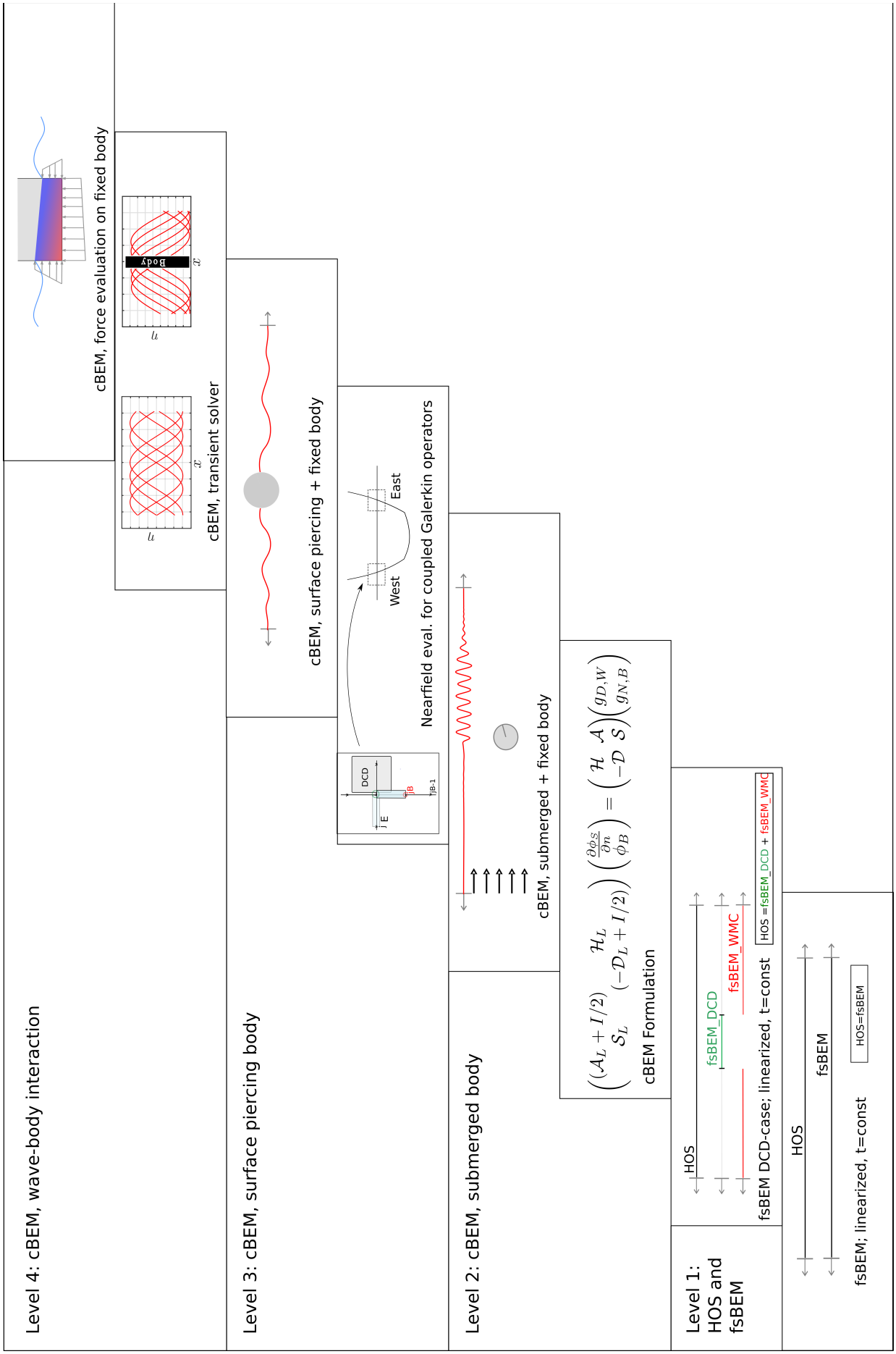

Figure 3.1: Schematic overview of cBEM development with selected steps.

are usually discretized by equidistantly spaced collocation points and limited by lateral borders on that periodic boundary conditions are defined. The HOS method solves for the dynamic and kinematic free surface boundary conditions by considering free surface quantities and applies series expansions to find the velocity potential and the surface elevation at the still water level $z = 0$. Taking the velocity potential and its normal derivative as Cauchy data into account, the incorporation into the BEM framework seems to be straightforward and raised the first research question, if the BEM solution and the first order HOS solution are equal under the assumption of linearity. By assuming the free surface as Dirichlet boundary, the NDBIE had to be solved. This made the assembly of the Hypersingular and the Adjoint BIOs necessary and the evaluation of neighbored element-element (adjacent) and element-element (self) influence required desingularization techniques. For the development of the BIOs, the frequency domain BEM developed by Schwarz [150] could be accounted as a reference and used as basis for the development of the new BIOs.
It was shown that the HOS operators with global support can be replaced by BIOs. The local basis functions allowed to consider the separation of the water boundary domain in a free surface and a discontinuous part. This would not have been possible with the global continuous basis functions built into the HOS approach. The Z-Splines, see [145], with interelement support have been employed as basis functions due to their consistent approximation of discrete Fourier series components.
The discontinuity in the boundary changed the assembly of the BIOs significantly. In general the BIOs (matrices of size n x m) represent the influence of each target domain (or field) point n to each source domain point m. With the discontinuity, a part of the boundary was not considered so that this part did not contribute to the influences. In this context, the elements, at which the water boundary was cutted, required special treatment, because one part of these elements belonged to the discontinuous part and the surrounding part to the free surface domain. As interelement basis functions had been used, this was specifically difficult because the influence of overlapping elements had to be accounted. To account the overlapping contributions at the intersecting elements, the adjacent and self regime evaluation were modified. With this tools the evaluation of one BIO for the free surface and one for the discontinuous surface part was possible and the second research hypothesis could be tested.

Level 2: Direct cBEM formulation and continuous cBEM testing Until this step, only the free surface had been accounted and the addressed task was to solve a Dirichlet BVP by using the NDBIE. In the next level, the coupled solving of wave-body interaction came into the focus. In a first step, the cBEM was formulated. The treatment of the body boundary as Neumann problem and the water boundary as Dirichlet problem resulted in the use of both the CBIE and the NDBIE.
The resulting block matrix system of the mixed BVP included in total eight BIOs, one of each kind in the LHS and the RHS block matrix. The BIOs were separated in four influence types, first and second the body to body (B2B) and water to water (W2W) influencing BIOs, third the water to body (W2B) and fourth the body to water (B2W) BIOs. The last two types covered the coupling between the two boundaries and were thus referred as Coupling BIOs. The boundary conditions were the free surface velocity potential and the normal derivative of the body potential and as unknown densities the normal derivative of the free surface velocity potential and the body potential were accounted.
The block inversion of the LHS operator matrix applied the Schurcomplement and operator identities which required symmetry of the block matrix. As in general the collocation BEM don't ensure a symmetric operator assembly, the symmetric Galerkin method, see Subsec. (2.1.6), was employed. The weighting of the BIEs with the local basis functions required the integration of both the target and the source domain function space. In contrast to the collocation approach, the Galerkin method fulfills the solution not strictly at the collocation points, but over the element in the integral sense. This results in more accurate solution as the linear combinations of boundary quantities by means of the BIE represent the best approximation to the exact solution, see [162]. Moreover, this lowered the requirements for the approximations functions to be C^0 continuous and allowed the account of the intersection points on the element so that the boundary discretization did not need to be rearranged.
The assembly of the BIOs in the symmetric Galerkin formulation was performed with special care on the

desingularization of the Hypersingular BIO. The initial testing of the Galerkin BIOs were performed in a Body BEM and could be directly used for the B2B BIOs in cBEM. Correspondingly, the W2W BIOs had been reformulated as Galerkin BIOs which required modifications in the assembly. Then the setup of the Coupling BIOs followed where the belonging of the target and source domain to different boundaries required new methods. In the first step, the submerged body had been considered where both the body and water surface were accounted as continuous. This step requires only the farfield assembly of the Coupling BIOs as the body was assumed to be sufficiently dived and not in the near influence regime of the free surface elements.
For the operator development, the symmetry of the BIOs was used as a fast check on the consistent assembly. For the sophisticated verification, the LWT equation was employed as analytic reference. By prescribing the velocity potential at the free surface this allowed the derivation of all Cauchy data for the mixed BVP.

Level 3: Discontinuous cBEM For the surface piercing body the assembly of the Coupling BIOs becomes more complex, because the body intersect with the water surface which results in discontinuities in geometry function space (normal and tangent vector are discontinuous) and in neighboring elements of body and water domain. The free surface excluding the discontinuous part and the submerged body geometry form the new boundary. The evaluation of the truncated body geometry and the intersected water boundary as well as the corresponding reduction of the BIOs gave rise to modified approaches for the discretization and the operator assembly.
The weakly and strongly singular Coupling BIOs in Galerkin formulation are regularized in the adjacent regime, because the (Duffy-like) mapping in parametric coordinate space decreases the singularity about one. In contrast, the desingularization of the Hypersingular BIO is necessary for the neighboring regime and gave the subject of the next large development step.
As the structure of the cBEM was too complex for checking the correct treatment of the discontinuous Coupling BIOs, a simplified test environment had been chosen as intermediate step for the development of the desingularization technique for the Hypersingular BIO. A test case from Bonnet & Guigianni [19] that have provided an analytic reference for the hypersingular integral, had been chosen to verify the desingularization technique. The test case had been extended to the case of adjacent elements of different basis function type (one of inter-, one of intraelement type) and to the analysis of the influence of the nearfield integration order.
The implementation of the Coupling BIO assembly in the cBEM framework followed and testing with the analytic reference from the LWT was done. The use of inter- instead of intraelement basis functions at the water surface limited the support of the basis function to one element and made the error analysis more comfortable because the overlapping influence of neighboring elements was avoided. The account of the basis functions of interelement support as representation for the free surface boundary has the advantage of approximating the spectral basis function, see Subsec. (2.1.4). Thus a mapping from one to the other function space representation has been implemented as postprocessing step in the matrix assembly.
By using the box geometry and defining the ratio of body and water elements to one, the discontinuous cBEM solution converged with a reasonable order to the LWT reference. This firstly proved the concept and the implementation of the Coupling BIO assembly including the adjacent regime desingularization of the Hypersingular BIO.
The change of the element size to an arbitrary element ratio ξ and the corresponding corner treatment needed further research. It pointed out that the C^0 interelement continuity requirement plays a significant role, because the endpoint values are of high relevance in the evaluation of the Galerkin type free terms. The use of closed Newton Cotes quadratures with fixed endpoints in an interior problem test case with disk geometry showed correct results with changing element ratio. Considering the box geometry, which added discontinuities in the normal vectors due to the corners, showed again incorrect results.
A general problem when using C^0 interelement continuous basis function is the evaluation of corner values in the case of a normal derivative (Neumann) solution space. As the corner represents a discontinuity

in the normal vectors of neighboring elements, the limiting value at the corner is not unique, because for the computation the corner neighboring elements could be accounted with the consequence to find different results. To overcome this, discontinuous (open) quadrature can be used as the endpoints are not explicitly accounted, but their values are given as extrapolation from the collocation points interior of the element (see Subsec. (2.1.5)). Following, the use of different continuity requirements for the Neumann and Dirichlet solution space (potential and normal derivative) allowed at least to satisfy the continuity requirements partly.
The strategy gave the correct solution for the box test case with varying element ratio. By comparing this with the solution found by accounting open quadratures for both Dirichlet and Neumann solution space it was figured out that adding an element ratio related term that to the free term expression gave converging results for only using open quadratures.

Level 4: Time integration and hydrodynamic test cases As the time domain analysis is one of the key characteristics of the cBEM, the explicit Runge-Kutta scheme was implemented for integration of the time dependent (non autonomous) quantities. The verification of the implementation was done with a fixed body geometry so that only the linear wave dynamic equations were integrated with time. For this the LWT reference was employed and by showing that the transient cBEM solution for the submerged body test case propagated the wave with constant wave form, the implementation of the time stepping scheme was proven. Also, the discontinuous cBEM was verified with the same test.
The time integration scheme was analyzed in terms of linear stability. By computing the eigenvalues of the dynamic system, the eigenvalues-times-timestep could be plotted in the complex plane and comparing with the stability region of the explicit Runge-Kutta scheme of accounted order indicated if the time stepping was stable for the chosen time step.
The applicability of the solver to hydrodynamic problems accounted foremost the radiation and diffraction problem. These cases have been theoretically and experimentally well investigated and suited literature could be found for setting up the test cases. The numerical results obtained with cBEM were compared with the literature and finally allowed to state about the accuracy of the solver.

3.2 Description of cBEM

The cBEM solver required the development of various methods for the pre-, post- and processing part of the program. In the following subsection an introduction and description of these methods follows. Previously, the mathematical foundation of the cBEM is presented.

3.2.1 Mathematical formulation

The BIOs play a significant role in the evaluation of BIEs and were of main priority in the development of cBEM. Following the procedures described in Sec. (2.1.2), the BIOs were defined as

$$\begin{aligned}
\mathcal{S}\gamma_1\phi(x) &= \int_\Gamma G(x,y)\frac{\partial\phi(y)}{\partial n_y}d\Gamma(y) \\
\mathcal{D}\gamma_0\phi(x) &= -\int_\Gamma \frac{\partial G(x,y)}{\partial n_y}\phi(y)d\Gamma(y) \\
\mathcal{A}\gamma_1\phi(x) &= \int_\Gamma \frac{\partial G(x,y)}{\partial n_x}\frac{\partial\phi(y)}{\partial n_y}d\Gamma(x) = -\mathcal{D}'\frac{\partial\phi(x)}{\partial n_x} \\
\mathcal{H}\gamma_0\phi(x) &= -\frac{\partial}{\partial n_x}\int_\Gamma \frac{\partial G(x,y)}{\partial n_y}\phi(y)d\Gamma(y)\,.
\end{aligned} \tag{3.1}$$

wherein the definition of the trace and conormal derivative of the trace operator were defined as

$$\gamma_0\phi = \phi$$
$$\gamma_1\phi = \frac{\partial\phi}{\partial n}\,,$$

the target and source domain were represented by x and y and $\partial\Omega = \Gamma$ is the boundary of the domain Ω on that the Laplace equation $\Delta\phi = 0$ is defined on. The Green Function was chosen to be

$$G(x,y) = \frac{1}{2\pi}\log|x-y|\,, \tag{3.2}$$

see Subsec. (2.1.3) for details.

Formulation of cBEM

The mixed BVP

$$\begin{aligned} -\Delta\phi(x) &= 0 && \text{for } x \in \Omega^c \\ \gamma_0^{ext}\phi(x) &= g_{D,W}(x) := \phi_S(x) && \text{for } x \in \Gamma_{W,D} \\ \gamma_1^{ext}\phi(x_B) &= g_{N,B}(x_B) := \frac{\partial\phi_S(x_B)}{\partial n} && \text{for } x_B \in \Gamma_{B,N} \end{aligned} \tag{3.3}$$

and the representation equation for the limiting case $\Omega \ni \hat{x} \to x \in \Gamma$ gives

$$\phi(\hat{x}) = \phi_0 - \int_{\Gamma_W} G(\hat{x},y_W)\gamma_1^{ext}\phi_S(y_W)ds_{y_W} + \int_{\Gamma_W}\gamma_{1,y_W}^{ext}G(\hat{x},y_W)g_{D,W}ds_{y_W} \tag{3.4}$$

$$- \int_{\Gamma_B} G(\hat{x},y_B)g_{N,B}ds_{y_B} + \int_{\Gamma_B}\gamma_{1,y_B}^{ext}G(\hat{x},y_B)\gamma_0^{ext}\phi_B(y_B)ds_{y_B} \tag{3.5}$$

which yield the corresponding coupled CBIE (cCBIE)

$$\gamma_0^{ext}\phi(x) = \phi_0 + (I/2-\mathcal{D})\gamma_0^{ext}\phi_S(x) + \mathcal{S}_L\gamma_1^{ext}\phi_S(x) + (I/2-\mathcal{D}_L)\gamma_0^{ext}\phi_B(x) + \mathcal{S}\gamma_1^{ext}\phi_B(x) \tag{3.6}$$

and the coupled NDBIE (cNDBIE)

$$\gamma_1^{ext}\phi(x) = +\mathcal{H}\gamma_0^{ext}\phi_S(x) + (I/2-\mathcal{A}_L)\gamma_1^{ext}\phi_S(x) - \mathcal{H}_L\gamma_0^{ext}\phi_B - (I/2-\mathcal{A})\gamma_1^{ext}\phi_B(x)\,. \tag{3.7}$$

Substituting the boundary condition for the Dirichlet and Neumann boundary domains, $\Gamma_{W,D}$ and $\Gamma_{B,N}$ respectively, gives the formulation of the direct cBIE,Gl. (3.8),

$$\begin{pmatrix} (\mathcal{A}_L + I/2) & \mathcal{H}_L \\ \mathcal{S}_L & (-\mathcal{D}_L + I/2) \end{pmatrix} \begin{pmatrix} \frac{\partial\phi_S}{\partial n} \\ \phi_B \end{pmatrix} = \begin{pmatrix} \mathcal{H} & \mathcal{A} \\ -\mathcal{D} & \mathcal{S} \end{pmatrix} \begin{pmatrix} g_{D,W} \\ g_{N,B} \end{pmatrix}\,. \tag{3.8}$$

Formulation of fsBEM

The consideration of the free surface alone, gave the Dirichlet BVP

$$\begin{aligned} -\Delta\phi(x) &= 0 && \text{for } x \in \Omega^c \\ \gamma_0^{ext}\phi &= g_{D,W}(x) := \phi_S(x) && \text{for } x \in \Gamma_{W,D} \end{aligned} \tag{3.9}$$

with the free surface velocity potential ϕ_S. The BIE Eq. (3.9) was calculated by using the NDBIE

$$\gamma_1^{ext}\phi(x) = \mathcal{H}\gamma_0^{ext}\phi_S(x) - \big(\sigma(x)I - \mathcal{A}\big)\gamma_1^{ext}\phi_S(x). \tag{3.10}$$

By reordering and substituting $\gamma_1^{ext} = \partial/\partial n_x$ the linear system Eq. (3.11)

$$\big(\mathcal{A} + \sigma(x)I\big)\frac{\partial\phi_S(x)}{\partial n_x} = \mathcal{H}g_{D,W}(x). \tag{3.11}$$

was found. In the linearized cBEM approach, the free surface was considered to be flat (vanishing normal vector in x direction) with the consequence that the Adjoint BIO vanishes. The two-dimensional version of the solid angle gives for complete elements $\sigma(x) = 1/2$ and was found all other cases by integration over the corresponding element part.

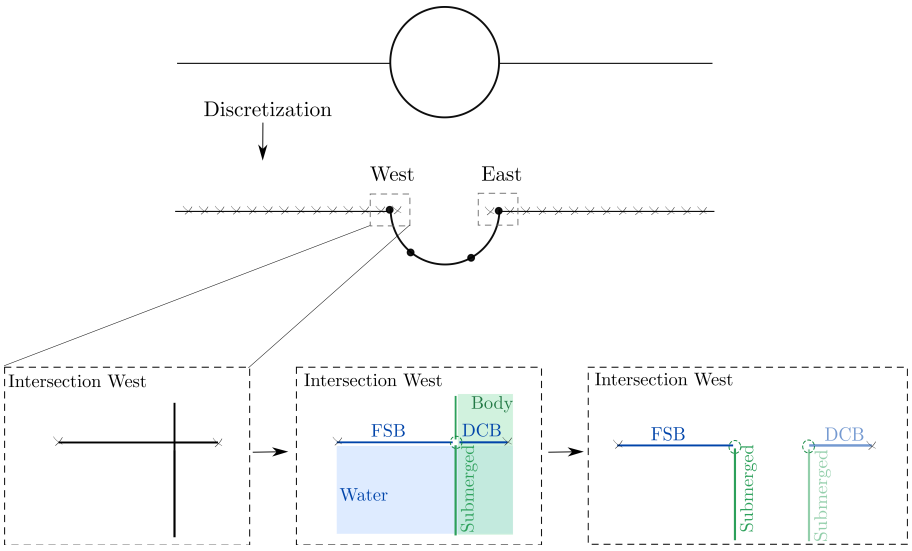

Figure 3.2: Free surface and body geometry, intersection points and consideration for kernel evaluation.

3.2.2 Routines for preprocessing

The preprocessing steps include the definition and discretization of the geometry and the function space as well as the handling of the data sets.

Discretization geometry

The discretization of the geometry required the definition of related properties as shape, size, orientation and location in global coordinates of the accounted geometries. By accounting the discretization parameters as e.g. the number of elements and the number of collocation points per element and a suited geometry representation as outlined in Subsec. (2.1.4), the approximative form of the geometry surface was found on that the collocation point and element related variables as the normal (and tangent) vectors and the element size could be computed.
As the water surface was considered to be flat due to the assumption of linearization, Subsec. (2.2.1), no specific geometry representation was chosen here, and the geometry related parameters could be found by trivial methods. For the body surface the representation functions were based on Bézier curves which gave a high accurate surface approximation.
Special parameters had to be considered for the discontinuous cases. In fsBEM, the discontinuity region was defined explicitly in global coordinates and allowed a straight forward evaluation of the variables at the surface intersections as the size of the element parts related either to the discontinuity or to the free surface region and specific flags for an efficient operator assembly. In cBEM, these variables were found by accounting the intersection of the water and the body surface, Fig. (3.2), and the relative position of the geometries were relevant.
On the basis of the intersection parameters the truncation of the body and the cut out of the discontinuous region from the water surface yielded reduced operators and formed the new mixed boundary domain.

Discretization solution space

For the discretization of the solution space the choice of basis functions and quadrature rule was of relevance. The integration was generally done by the Gauss-Legendre quadrature. The solution space of the body was approximated by basis functions of intraelement support for the standard farfield integration. The upsampling to a higher number of integration points employed the Lagrange polynomial basis function which then were concatenated with the farfield integration values.

In the case of the water surface, the consideration of Z-Splines, see Subsec. (2.1.4), as basis function allowed the local approximation to the continuous periodic functions with global support that are accounted in the HOS method. The influence of the Z-Splines depend on the accounted order and was mostly chosen as two which limited the support to four neighboring elements. For the assembly, the concatenation of the integration values with the Z-Spline basis function had to be evaluated and needed special treatment on the lateral boundaries when the Method of Farfield Extension or periodicity was accounted. Because the interelement basis function approach considered neighboring elements, the value given at one element was equal to the sum of overlapping portions of its neighbors. This complicated the assignment of values to the element and made the error analysis more difficult.
Therefore, an alternative approach was applied, the mapping to the Z-Spline function space, which allowed the subsequent evaluation of the interelement operator version on the basis of the previously assembled intraelement operator sub matrices.

Data handling

The use of various user defined constants in different code subroutines gave rise to the use of containers in which the constants were collect and simple access was guaranteed. Such containers were used e.g. for the group of physical, geometry and time stepping related constants and variables.

3.2.3 Routines for processing

The integration of the Green kernel function and its derivatives under considering the influence of each collocation on each collocation point is one of the main tasks in the core part of the solver, to which as well the time stepping and the solution evaluation belong.

Operator assembly

Setting up the BIOs contains the integration of weakly to hypersingular kernel functions in all influence regions which include the definition of the fundamental solution or its corresponding derivatives and the choice of basis function, the use of images and the decision which BEM formulation is used.
The BIOs contain the influences between collocation points and are assembled as matrices in that row and column dimension represent the target and source domain respectively.
The symmetric Galerkin approach accounts both the source and target domain for integration. The integration of a pair of collocation points requires the evaluation of a double integral that in addition with the concatenation of the source and target domain basis functions resulted in a submatrix. The assembly of all point pair contributions gave then the complete BIO.
The singular property of the kernel function required to distinguish between the influences in the far- and nearfield (more than two element distances) and the adjacent- and self-regime influences. Whereas in the far- and nearfield integration as well as the upsampling of the integration order the standard double integration, similar for all operators, could be applied, the adjacent- and self-regime evaluation required operator specific desingularization methods. By adding these influences, the final and complete operators were set up.
The size of the operators varied firstly due to the number of elements and collocation points and secondly by the type of influences. The B2B and W2W BIOs gave square matrices whereas the Coupling BIOs resulted in non-square matrices.
Using basis functions of interelement support for the water domain made the account of overlapping influences necessary, see Parag. (3.2.2).
For the boundary conditions of the water domain in the lateral direction (x-coordinate), the Method of Farfield Extension was applied.

Definition 3.2.1. *(Images, Method of Farfield Extension.) Images are a virtual extension of a boundary domain. The Method of Farfield Extension is referred as k-times copying the source boundary domain in*

both the positive and negative direction of the extended coordinate(s), where $im = x$ is referred as the x-th image. The central image, $im = 0$, is the original boundary domain. The Method of Images can be used to approximate the solution obtained with periodic boundary conditions. Therefore, the boundary domain is extended in the direction of the periodic dimension/coordinate.

This allowed to satisfy the periodic boundary condition of the HOS approach with the free space fundamental solution. The number of images N_{Im} was chosen to a case specific values for that the solution converged. The farfield influences of the extended domains were added to the corresponding entrances of the BIO. Apart from the adjacent evaluation at the last and first elements on the images, $im = -1$ and $im = 1$, the self and adjacent regime influences only relate to the central image.

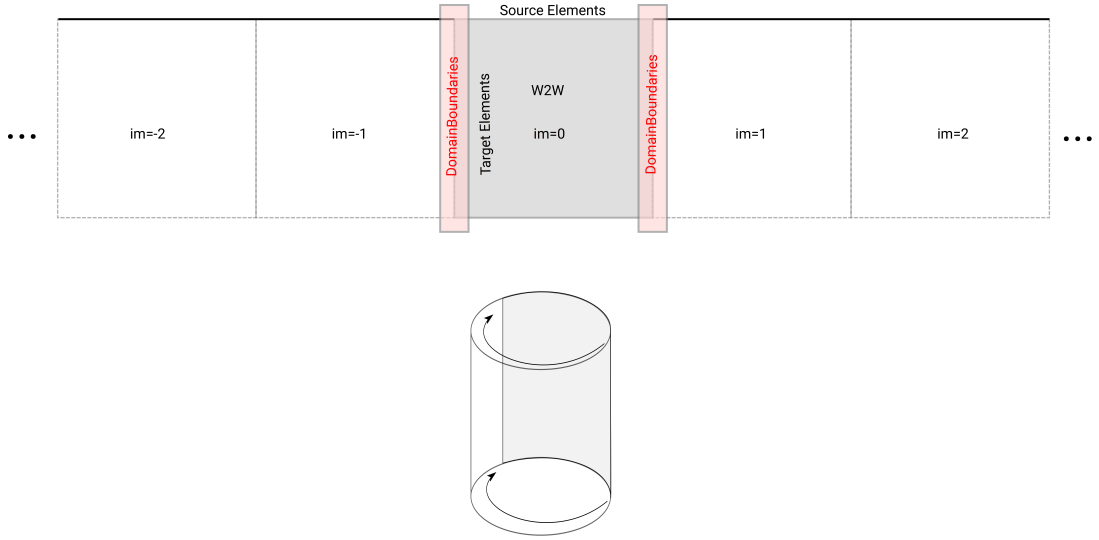

Figure 3.3: Images in the range of $im \in [-2, 2]$ for the Hypersingular W2W BIO. The central image $im = 0$ is shown in gray with the domain boundaries represented in light red. The black dots at both positive and negative end of the images range denote the possible extension of the images to both sides of the domain. The bottom figure illustrates the periodic boundary condition for that the domain boundaries are connected.

Solving procedure

The linear system Eq. (3.8) could be solved either by block matrix inversion which required the symmetry of the LHS matrix or by applying the LU decomposition. Both methods are explained hereafter.

Block matrix inversion Considering the formula for block matrix inversion and by using the inverse of the Schur complement

$$K^{-1} = \left((\mathcal{D}_L - \frac{I}{2}) - 2\mathcal{S}_L\mathcal{H}_L\right)^{-1} \tag{3.12}$$

the inversion of the LHS blockmatrix gave

$$\begin{aligned}
\begin{pmatrix} \frac{\partial \phi_S}{\partial n} \\ \phi_B \end{pmatrix} &= \begin{pmatrix} -I/2 & \mathcal{H}_L \\ \mathcal{S}_L & (\mathcal{D}_L - I/2)^{-1} \end{pmatrix} \begin{pmatrix} -\mathcal{H} & -\mathcal{A} \\ -\mathcal{D} & -\mathcal{S} \end{pmatrix} \begin{pmatrix} g_{D,W} \\ g_{N,B} \end{pmatrix} \\
\begin{pmatrix} \frac{\partial \phi}{\partial n}|_W \\ \phi|_B \end{pmatrix} &= \begin{pmatrix} -2 - 2\mathcal{H}_L K^{-1}\mathcal{S}_L 2 & +2\mathcal{H}_L K^{-1} \\ -K^{-1}2\mathcal{S}_L & K^{-1} \end{pmatrix} \begin{pmatrix} -\mathcal{H} & -\mathcal{A} \\ -\mathcal{D} & -\mathcal{S} \end{pmatrix} \begin{pmatrix} g_{D,W} \\ g_{N,B} \end{pmatrix} \\
\begin{pmatrix} \frac{\partial \phi}{\partial n}|_W \\ \phi|_B \end{pmatrix} &= \begin{pmatrix} 2\mathcal{H} + 4\mathcal{H}_L K^{-1}\mathcal{S}_L\mathcal{H} - 2\mathcal{H}_L K^{-1}\mathcal{D} & 2A + 4\mathcal{H}_L K^{-1}\mathcal{S}_L A - 2\mathcal{H}_L K^{-1}\mathcal{S} \\ 2K^{-1}\mathcal{S}_L\mathcal{H} - K^{-1}D & -2K^{-1}\mathcal{S}_L A - K^{-1}\mathcal{S} \end{pmatrix} \begin{pmatrix} g_{D,W} \\ g_{N,B} \end{pmatrix}
\end{aligned} \tag{3.13}$$

Following Miller [116], the inverse of the Schurcomplement was computed by

$$\begin{aligned} K^{-1} =&(\mathcal{D}-\tfrac{I}{2})_L^{-1} - \frac{1}{1+\text{trace}\big(2\mathcal{S}_L\mathcal{H}_L(\mathcal{D}-\tfrac{I}{2})_L^{-1}\big)}(\mathcal{D}-\tfrac{I}{2})_L^{-1}2\mathcal{S}_L\mathcal{H}_L(\mathcal{D}-\tfrac{I}{2})_L^{-1} \\ =&(\mathcal{D}-\tfrac{I}{2})_L^{-1} - \frac{1}{1+\text{trace}\big((\tfrac{I^2}{2}-2\mathcal{D}^2)(\mathcal{D}-\tfrac{I}{2})_L^{-1}\big)}(\mathcal{D}-\tfrac{I}{2})_L^{-1}(\tfrac{I^2}{2}-2\mathcal{D}^2)(\mathcal{D}-\tfrac{I}{2})_L^{-1} \end{aligned} \tag{3.14}$$

wherein the identity for Single layer and Hypersingular BIOs Eq. (2.28.1)

$$\mathcal{S}\mathcal{H} = \Big(\frac{I}{2}+\mathcal{D}\Big)\Big(\frac{I}{2}-\mathcal{D}\Big) = \frac{I^2}{4}-\mathcal{D}^2. \tag{3.15}$$

was applied. The normal derivative of the free surface could then computed by

$$\begin{aligned} \tfrac{\partial\phi}{\partial n}|_W = \big(2\mathcal{H} + 4\mathcal{H}_L K^{-1}\mathcal{S}_L\mathcal{H} - 2\mathcal{H}_L K^{-1}\mathcal{D}\big)\, g_{D,W} + \\ \big(\quad 2A + 4\mathcal{H}_L K^{-1}\mathcal{S}_L A - 2\mathcal{H}_L K^{-1}\mathcal{S}\big)\, g_{N,B} \end{aligned} \tag{3.16}$$

and the potential on the body

$$\phi|_B = \big(2K^{-1}\mathcal{S}_L\mathcal{H} - K^{-1}D\big)\, g_{D,W} + \big(-2K^{-1}\mathcal{S}_L A - K^{-1}\mathcal{S}\big)\, g_{N,B} \tag{3.17}$$

LU decomposition The LU decomposition, see e.g. [176], is a solving procedure for linear systems with square matrices. In the algorithm, a matrix A is decomposed in a lower and upper matrix, L and U, and with the permutation matrix P, the linear system can be rewritten as

$$\begin{aligned} Ax =& b \\ LUx =& Pb\,. \end{aligned} \tag{3.18}$$

A solution can be found by first solving for y in $Ly = Pb$ with forward substitution and second solve for x in $Ux = y$ by backward substitution. The decomposition of the matrix in a lower and upper triangular matrix is usually found by Gaussian elimination.
For regular matrices A, P equals one. If A contains singular principal submatrices, the LU decomposition fails and the entrances in A have to be inter changed (pivoting). These operations on A are saved in the permutation matrix P with that the modified matrix can be reordered to the original matrix. If not only the rows of A are modified (partial pivoting), the matrix is full pivoted which requires an additional permutation matrix to save the column operations.
The LU decomposition in addition with the substitution and considering partial pivoting requires $\frac{2}{3}n^3 + \mathcal{O}(n^2)$ floating points operations with n the size of the matrix, and is slower than solvers for more structured matrices as the diagonal or the triangular solver, but twice as fast as the QR decomposition applied to non-square matrices as here the Gaussian elimination fails and the Householder transformation is required.

Time integration

The evaluation of the time domain solution in cBEM was realized by the implementation of the explicit Runge-Kutta time integration scheme. The evaluation of linear wave dynamics with non-stiff equations allow using an explicit method. As usual in explicit methods, the new time step variables are computed on the basis of a previous state. The Runge-Kutta scheme is based on a Taylor series expansion of variable time around the previous state and the accuracy is increased by considering higher order terms in the expansion. Intermediate stages at discrete times are calculated representing the local slope respectively the expansion term of the considered dynamic equations in time. After evaluating all terms, they are weighted, summed and multiplied by the time increment and added to the variable of the previous state. This last step represent the Taylor expansion. The Runge-Kutta first order (RK1) scheme also referred

as Euler Explicit and the Runge-Kutta fourth order (RK4) scheme were implemented in cBEM. For the intermediate stages, the wave dynamics and the rigid body motion had been accounted. In the case of a fixed body, only the former was considered.

The implementation is illustrated by taking the RK4 scheme, the discrete time t_n and considering only the target variable y to be integrated in time. Then the four slopes k_i at the discrete times t_n, $t_n + dt/2$ and $t_n + dt$ are given by

$$\begin{aligned} k_1(c) &= f(t_n, y_n, c(t_n)) \\ k_2(c) &= f(t_n + dt/2, y_n + dt/2k_1, c(t_n + dt/2)) \\ k_3(c) &= f(t_n + dt/2, y_n + dt/2k_2, c(t_n + dt/2)) \\ k_4(c) &= f(t_n + dt, y_n + dtk_3, c(t_n + dt)) \\ &\cdot \end{aligned} \tag{3.19}$$

The variable c represents a boundary condition for that an analytical solution exist and a fourth order Taylor series expansion given by

$$c(t_n) = c(t_n) \tag{3.20}$$

$$c(t_n + dt/2) = c(t_n) + \frac{\partial c(t_n)}{\partial t}(dt/2) + \frac{\partial^2 c(t_n)}{\partial t^2}\frac{(dt/2)^2}{2} + \frac{\partial^3 c(t_n)}{\partial t^3}\frac{(dt/2)^3}{6} \tag{3.21}$$

$$c(t_n + dt) = c(t_n) + \frac{\partial c(t_n)}{\partial t}dt + \frac{\partial^2 c(t_n)}{\partial t^2}\frac{dt^2}{2} + \frac{\partial^3 c(t_n)}{\partial t^3}\frac{dt^3}{6} \tag{3.22}$$

has been applied to get the corresponding accuracy at each RK stage.

Linear stability analysis for time integration scheme

The analysis in terms of linear stability was used to indicate if the applied Runge-Kutta order and the resulting stability region matched with the cBEM problem and the considered time discretization. Therefore, the eigenvalues of the linear dynamic equation were evaluated by considering the characteristic equation $det(T - \lambda I) = 0$ with T given in case of a fixed body and LWT by

$$T = \begin{pmatrix} \frac{\partial^2 \phi}{\partial t \partial \eta} & \frac{\partial^2 \phi}{\partial t \partial \phi} \\ \frac{\partial^2 \eta}{\partial t \partial \eta} & \frac{\partial^2 \eta}{\partial t \partial \phi} \end{pmatrix} = \begin{pmatrix} 0 & \mathrm{LHS}^{-1}\mathrm{RHS} \\ gI & 0 \end{pmatrix} \tag{3.23}$$

with the cBEM operator $\mathrm{LHS}^{-1}\mathrm{RHS}$. By checking if λdt was within the stability region of the Runge-Kutta scheme, the time discretization and order of the time integration were indicated to be sufficient for a stable computation in time domain.

3.2.4 Routines for postprocessing

For the analysis of the cBEM solution the postprocessing routines are essential and introduced in the next paragraphs.

Evaluation of analytic reference

The existence of an analytic reference was of high relevance for the development of cBEM, because it enabled to prove that the solution was consistent and accurate and to demonstrate the verification of the implemented methods. As the BEM is in general a highly accurate numerical method, the solution should converge to the analytic reference at a convergence order that is in line with the error convergence order of the quadrature rule and the solution function and geometry representations, see also Subsec. (2.1.4). As analytic reference for cBEM the velocity potential Eq. (2.87) linearized to its free surface quantity is

used. In this case $\phi_S = \phi(x, z = 0; t)$ and considering deep water and a single wave ($\varphi = 0$), the velocity potential and its normal derivative $\partial\phi_S/\partial n$

$$\begin{aligned} \phi_S(x;t) &= -\frac{\hat{\eta}g}{\omega}\,\mathrm{exp}^{i(kx-\omega t)} \\ \frac{\partial\phi_S}{\partial n}(x;t) &= \left\langle \left(\mathrm{Re}(-ik\frac{\hat{\eta}g}{\omega}\,\mathrm{exp}^{i(kx-\omega t)}), \mathrm{Re}(-k\frac{\hat{\eta}g}{\omega}\,\mathrm{exp}^{i(kx-\omega t)})\right)^T, n_W \right\rangle \end{aligned} \tag{3.24}$$

were accounted. Therein, $\langle ., . \rangle$ denotes the scalar product and n_W the unit normal vector of the water surface.
For the development of his numerical wave tank, Xü [188] have used a similar approach for the error analysis, see Sec. (1.2.3).
The projection of the free surface solution to the submerged part of the body, as well gave the potential and its normal derivative

$$\begin{aligned} \phi_B(x_B, z_B; t) &= -\frac{\hat{\eta}g}{\omega}\,\mathrm{exp}^{i(kx_B-\omega t)}\,\mathrm{exp}^{kz_B} \\ \frac{\partial\phi_B}{\partial n}(x_B, z_B; t) &= \left\langle \left(\mathrm{Re}(-ik\frac{\hat{\eta}g}{\omega}\,\mathrm{exp}^{i(kx_B-\omega t)}\,\mathrm{exp}^{kz_B}), \mathrm{Re}(-k\frac{\hat{\eta}g}{\omega}\,\mathrm{exp}^{i(kx-\omega t)}\,\mathrm{exp}^{kz_B})\right)^T, n_B \right\rangle \end{aligned} \tag{3.25}$$

with the coordinates of the collocation points on the body surface (x_B, z_B) and the unit normal vector at the body surface n_B. The knowledge of the complete Cauchy data made it possible to use them in cBEM as boundary conditions and analytic references for the solution.

Error evaluation and convergence testing

The evaluation of the error in cBEM for vector valued variables was usually done with the relative error of the L_2-norm $||\cdot||_2 = (\sum_i(\cdot)_i^2)^{1/2}$, that reads

$$E_{L_2} = \frac{||x - x_{ref}||_2}{||x_{ref}||_2} = \sqrt{\frac{\sum_i(|x_i - x_{i,ref}|)^2}{\sum_i |x_{i,ref}|^2}} \tag{3.26}$$

wherein x_{ref} denotes the vector valued analytic reference and x the solution vector of cBEM. For the Galerkin approach the error is integrated over the boundary of interest yielding

$$\int (E_{L_2}) d\Gamma = \sqrt{\frac{\sum_i(|x_i - x_{i,ref}|)^2 w_i J_i}{\sum_i |x_{i,ref}|^2 w_i J_i}} \tag{3.27}$$

with the Jacobian J and the weights of the quadrature rule w.

The error evaluation was performed only on elements that related to the considered BVP. In the case of the exterior free surface piercing problem, the elements in the region of the discontinuity were not considered, and the error was only computed for the remaining water and the submerged body elements.

By plotting the error over the refined quantity in a logarithmic scaled coordinate system, the convergence order $\mathcal{O}(E)$ is given by the slope m_E of the line through the error points. For two error points, $e_1(x_1, y_1)$ and $e_2 = (x_2, y_2)$, the convergence order is given as $\mathcal{O}(E) := m_E = \log(y_2/y_1)/\log(x_2/x_1)$.

Evaluation of loads on the body

The forces that act on the body were found by integrating the pressure p over the bodies wetted surface $\Gamma_{B,wet}$ and concatenating it with the unit normal vector of the body hull n_B

$$F = \int p n_B d\Gamma_{B,wet}. \tag{3.28}$$

For the evaluation of the pressure the Bernoulli equation (conservation of momentum)

$$0 = -\frac{p - p_a}{\rho_w} + \frac{\partial \phi_B}{\partial t} + g z_B + \frac{1}{2}\nabla\phi_B \nabla\phi_B \tag{3.29}$$

was applied in its linearized form $\frac{1}{2}(\nabla\phi_B)^2 = 0$ and by assuming that the atmospheric pressure p_a vanishes. This was done on the basis of the new time variables right after the evaluation of the time stepping scheme during the processing of the cBEM. As the body potential was considered as unknown density in the cBEM, it contains the information of the transient free surface velocity potential and can be directly used for the pressure evaluation. For the hydrostatic component gz_B the submerged part (wetted surface) of the body was accounted by the vertical collocation point coordinates z_B. The unsteady part in the Bernoulli Eq. (3.29) could be computed by taking the previous value of the body potential into account and applying the first order forward finite difference scheme

$$\frac{\partial \phi_B}{\partial t} = \frac{\phi_B^{t+1} - \phi_B^t}{dt}. \tag{3.30}$$

This first order accurate account of the instationary part lead to inaccuracies in the solution as only the two subsequent solutions are accounted.

A higher order time integration was realized as a postprocessing step. By using the saved body surface potential in the second order forward, central and backward Finite Difference schemes

$$\begin{aligned}
\frac{\partial \phi_B}{\partial t} &= \frac{-\frac{3}{2}\phi_B^t + 2\phi_B^{t+1} - \frac{1}{2}\phi_B^{t+2}}{dt} \\
\frac{\partial \phi_B}{\partial t} &= \frac{\frac{1}{2}\phi_B^{t+1} - \frac{1}{2}\phi_B^{t-1}}{dt} \\
\frac{\partial \phi_B}{\partial t} &= \frac{\frac{1}{2}\phi_B^{t-2} - 2\phi_B^{t-1} + \frac{3}{2}\phi_B^t}{dt}
\end{aligned}, \tag{3.31}$$

the instationary forces at each time step could be calculated after the computations.

3.3 Evaluation of self and adjacent regime influences

The singular kernels in cBEM were desingularized in the self-and adjacent-regime by applying the direct approach introduced by Bonnet & Guiggiani [19], see the description in Parag. (2.1.7). This method was accounted directly in cBEM for the standard case as in the continuous fsBEM and cBEM setups and in a modified or extended manner in the discontinuous Dirichlet and mixed BVP. The new developments are highlighted in the following and starts with the discontinuous Dirichlet problem before coming to the coupled discontinuous problem. Here the hypersingular kernel was considered first as its desingularization is most challenging. For the cBEM approach also the evaluation of the weaker kernel functions is described, and the modification are compared to the standard direct approach.

3.3.1 Direct desingularization in discontinuous fsBEM

In the case of a discontinuous Dirichlet boundary and considering linearized wave dynamics, see Parag. (3.2.1), only the Hypersingular BIO was of interest. A modified approach was required at the elements that hold the intersection because neighbored parts of the boundary did not remain to the same domain with the consequence that their influences had to be assembled in two separate operators.

Definition 3.3.1. *(Intersection, IatE, IinE, IE) Let Γ_{disc} be a two-dimensional discontinuous boundary domain, then an Intersection is referred as the point that remains to both the adjacent boundaries and the Intersection Element (IE) is the element that contains the intersection. Two scenarios of intersection can be distinguished: the Intersection at Endpoint (IatE) represent the case of coinciding intersection and element endpoint and the Intersection in Element (IinE) case mention that the intersection point lies within the element.*

It can be noted that the definition of IatE has the consequence that the full element is assigned to one domain. In contrast, the element is separated in two parts that are assigned to different boundary parts for the IinE case.

Self case at intersection element Considering the IatE case, the same treatment as in the standard case was used and only the assignment to the correct BIO had to be accounted.
For the IinE case, first the geometric properties of the intersection element parts had to be evaluated. To compute the self regime contribution between the collocation points (self_inE), two options were possible. At the element part neighbored to the singularity, the integration was performed by distributing integration points over the accounted part, mapping to parametric coordinates and applying the direct approach for self influence. The corresponding second element part contribution was found as difference of the self regime influence of the complete element (standard case, self_std) and the element part neighbored to the singular point, see Fig. (3.4). The two element contribution were then written to the BIOs of the corresponding domain.

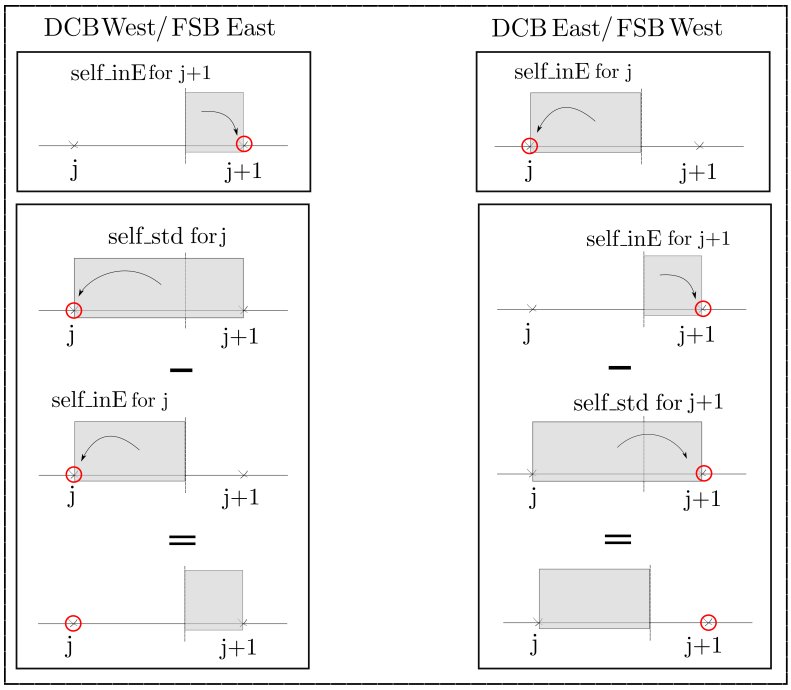

Figure 3.4: Method for the evaluation of the self influences, self_std and self_inE, in the IinE case shown for the discontinuous and free surface operators, CO and WMC, at the West and East intersection elements between the collocation points j and j+1. The gray shadowed element part is considered, the arrow denotes the evaluation to the singular point (red circle).

Adjacent-regime case at intersection element For the IatE case either the adjacent (A) or the transposed adjacent (TA) neighbor did not remain to the same boundary part as the intersection element. The influence of this neighbor element was evaluated with the standard method, but accounted in the operator of the corresponding other domain. This gave two contributions to each of the DCB and the FSB.
The IinE adjacent cases were evaluated by following the self-influence evaluation with the difference that in total six contributions at the intersection element had been accounted, three for each of the DCB and the FSB. The number of six came due to considering the intersection point, and it left and right neighbors

as source elements, then the constellations were

s=IE-1: TA (t=s+1, FSB) A (t=s-1, FSB)

s=IE : TA(t=s+1, DCB) A(t=s-1, FSB)

s=IE+1:TA(t=s+1, DCB) A(t=s-1, DCB)

where s and t are the source and target points, respectively.

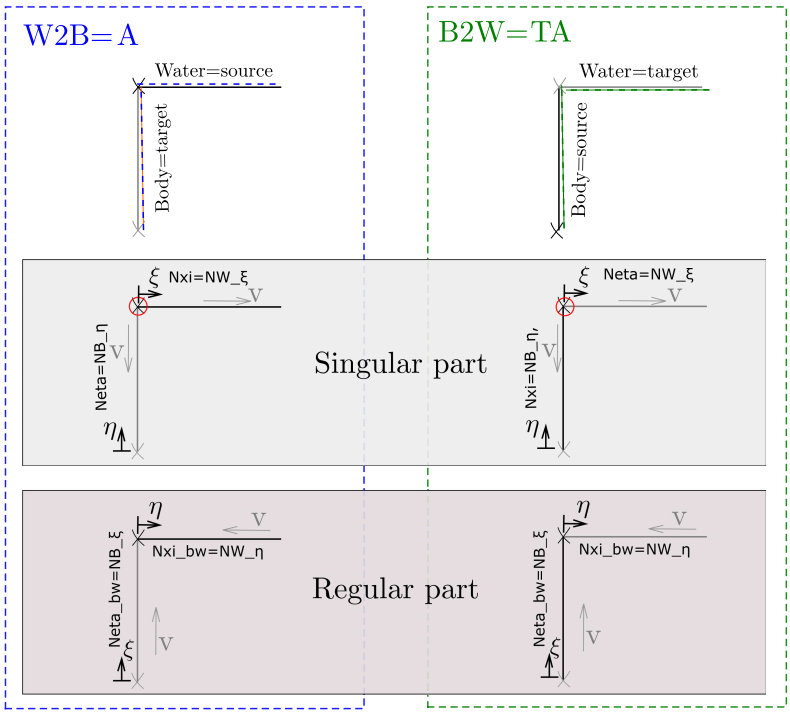

Figure 3.5: For the W2B and the B2W type Coupling BIOs, the adjacent influence evaluation is sketched by means of coordinate and basis function definitions. The latter include Nxi, Neta and their backward counterpart, the former account v, η and ξ and their direction.

3.3.2 Direct desingularization in discontinuous cBEM

The discontinuous coupled approach required modified adjacent desingularization techniques for the Coupling BIOs due to the not inherently same solution function space and same geometry discretization of the boundaries forming the mixed BVP as well as due to the discontinuity of the geometry function space in terms of the tangent/normal vectors. A different solution function space was e.g. given by applying basis functions of interelement type on the one and intraelement type on the other boundary. A leading order difference in geometry was represented by an element ratio χ of the two boundary discretizations that differs from one. The discontinuity of the geometry function space was caused by corners at the intersection of the boundaries. Conclusively, the modified approach had to account potentially varying basis functions and discretization parameters and had to include an appropriate corner handling.
Note that only the direct desingularization approach for the adjacent cases was relevant as in the Coupling BIOs the elements of source and target domain never coincided.
In the following the approaches for weak and strong singular kernel functions are presented before the hypersingular case is considered.

Weak and strong singular integrands By applying the transformation in parametric coordinates with the Duffy mapping, the weak and strong singular kernel function indeed does not require a desingular-

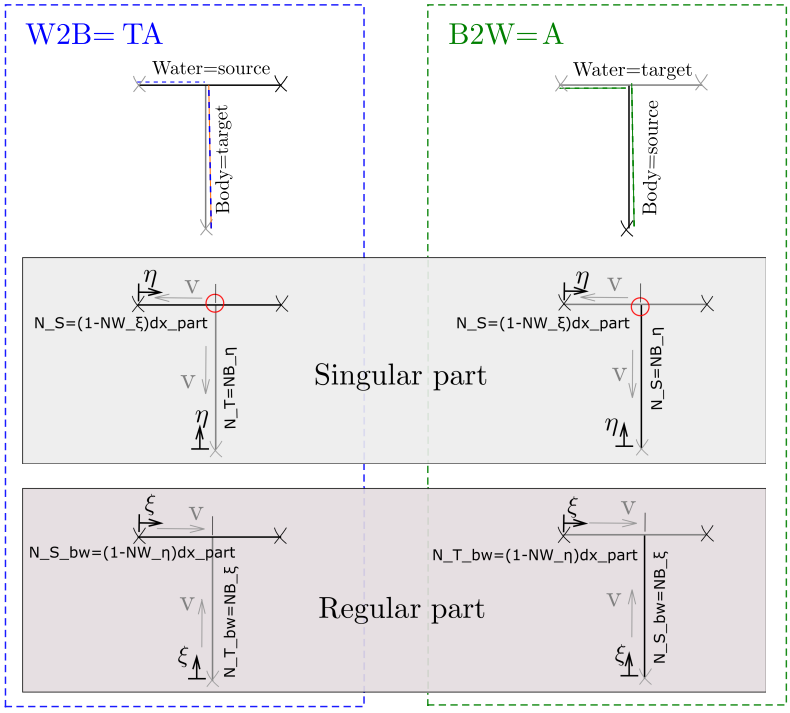

Figure 3.6: Method for the evaluation of the adjacent influence for Coupling BIO in exemplary IinE cases. The definitions at the boundary elements for the West and East intersections are given for the singular and the regular part of the integral kernel contribution. Marked by the red circle, the singularity in the element is highlighted. The coordinates v, η and ξ as well as the source and target basis function N_T and N_S as well as there redirection are shown for the four cases.

ization for the adjacent cases. This is due to the reduction of the singularity about one when the mapping is applied. The regularized integrals and the main steps for the evaluation of the Coupling BIOs similar to the direct approach are highlighted. They include some slight modifications that come from the adaption to the accounted mixed BVP and the above stated consequences as flexibility in terms of geometry and solution function space.
After the mapping to parametric coordinates, routine specific parameters were defined. The specific parameters are e.g. the position of the singular point, the used basis function, the number of integration points or geometric properties of the accounted elements. These parameters varied for the accounted boundary parts and intersection points (West or East IE) and the adjacent cases (transposed adjacent or adjacent) so that a case depending arrangement for the approach was chosen. A relevant geometry property was also the numbering of elements and collocation points, which possibly affected the direction of the parametric coordinate definition used for the two-dimensional domain integration. Based on the routine specific parameters the integration of the kernel functions was performed.
The assignment of the influences to the corresponding operators and location was done afterwards also under account of the specific definitions, as e.g. the basis function type for that the overlapping of influences have to be considered.

Hypersingular integrand The desingularization of the hypersingular kernel function accounts the evaluation of Galerkin specific expressions for the unbounded and bounded free terms that are specifically relevant for the occurence of corners and varying geometrical discretization parameters.
The development of the modified direct approach accounted a flexible choice for the discretization of solution function space and geometry as well as both the IatE and IinE case. As the testing in the cBEM environment was difficult in terms of error attribution, the test case and the analytic reference for the hypersingular kernel of Bonnet & Guiggiani [19] had been used. After implementation of the test case, it was extended to match with the intersection case in cBEM. This included the use of inter- and intraelement

basis function in the same test case setup and the account of both the adjacent and Transposed adjacent case which was given by considering the West and East intersection in the mixed BVP. In Figs. (3.5) and (3.6), the main considerations for the IatE and IinE cases for the Coupling BIOs are visualized. The choice of the basis function for the specific cases, the definition of the direction of the coordinates and the consideration of regular or singular contributions are shown for both the adjacent (A) and its transposed (TA) case. The convergence to the analytic solution, see Subsec.(3.4.2), proves the developed concept.

Free term evaluation For the evaluation of the free terms in cBEM, the expression for isotropic elements, introduced by Bonnet & Guiggiani [19]

$$\phi(z)\psi(z)D_A = \phi(z)\psi(z)\Big(\frac{1}{2\pi} + \frac{(1-\chi^2)\ln(\chi) - 2\chi\beta'\sin(\beta')}{4\pi(1+\chi^2-2\chi\cos(\beta'))}\Big) \tag{3.32}$$

with the element ratio of adjacent elements χ, the enclosing angle β between the adjacent elements, and the trial and test functions, ϕ and ψ, was considered. In the following, first the basis of this free term expression is introduced and second the analysis of the expression in terms of the discontinuous geometry representation and an element ratio different from one is presented.

In Bonnet & Guiggiani [19], the free term at singular end point $y = z$ for the adjacent part D_A considering an isotropic problem is given by

$$\psi(z)\phi(z)D_A = \Pi_{\text{sing, adj}} + \Pi_{\text{FT, adj+self}} + \Pi_{\text{endp, self}} \tag{3.33}$$

and contains three parts, namely the analytic part related to $\ln(|R|) = \ln(s_A)$ of the singular adjacent integral on the neighbor element E', $\Pi_{\text{sing, adj}}$,

$$\begin{aligned}\Pi_{\text{sing, adj}} &= \int_0^1 Q_A(u,0)\ln(s_A(u))du \\ &= \phi(z)'\psi(z)\frac{1}{2\pi}\int_0^{\beta'}\frac{\cos(2\omega-\beta')}{\sin(\beta')}\ln(|s_A(\omega)|)d\omega \\ &= \phi(z)'\psi(z)\frac{1}{2\pi}\int_0^{\beta'}\frac{\cos(2\omega-\beta')}{\sin(\beta')}\ln\Big(\Big|\frac{2aa'\sin(\beta')}{a\sin(\omega)-a'\sin(\omega-\beta')}\Big|\Big)d\omega \quad ,\end{aligned} \tag{3.34}$$

the free term contribution at the shared endpoint of both the adjacent and self parts, $\Pi_{\text{FT, adj+self}}$,

$$\begin{aligned}\Pi_{\text{FT, adj+self}} =& \frac{1}{2}\Big[H^+(E) + H^-(E')\Big] \\ =& \frac{1}{2}\Big[\mathcal{H}_i'(-\pi,0,z)n_i' - \mathcal{H}_i(0,0,z)n_i - \\ &- \psi(z)\phi(z)\int_0^{\beta'}\{\mathcal{H}_i(\theta,0,z)n_i + \mathcal{H}_i(\pi-\theta,0,z)n_i'\}\frac{\cos(\theta-\beta')}{\sin(\beta')}d\theta\Big] \quad ,\end{aligned} \tag{3.35}$$

with

$$\mathcal{H}_i(\omega,0,z) = \frac{1}{2\pi}\Big(\sin(\omega)t_i(z) + \big(1-\cos(\omega)\big)n_i(z)\Big) \quad , \tag{3.36}$$

as well as the endpoint terms of the self parts of elements E and E', $\Pi_{\text{endp, self}}$,

$$\begin{aligned}\Pi_{\text{endp, self}} &= -\Big(F(z,0)\ln(2a) + F'(z,0)\ln(2a')\Big) \\ &= -\frac{1}{4\pi}\Big(\psi(z)\phi(z)\ln(2a) + \psi'(z)\phi'(z)\ln(2a')\Big).\end{aligned} \tag{3.37}$$

The prime indicates quantities of the neighbor element E', n , t and a are the unit normal, the natural tangent and the unit tangent vectors and the superscripts $^+$ and $^-$ give the left and right side on the

boundary to the shared element endpoint z. The self regime type free terms H are given by considering the hypersingular kernel functions $\mathcal{H}(\omega, \varepsilon, z)$ in the vanishing neighborhood $\varepsilon = 0$ and the endpoint values $F(z, 0)$ are considered for the third free term part $\Pi_{\text{endp, self}}$.
For the formulation of the free terms, the solution space of ϕ is required to be C^0 continuous over the elements, also referred as interelement C^0 requirement. This implies the use of basis functions and quadrature rules that account the interval end points of the parametric coordinate space. By defining the values at the shared end points of adjacent elements to coincide, the interelement C^0 requirement is satisfied. An appropriate basis function are e.g. the closed, end-point continuous Newton Cotes formulas, see Subsec. (2.1.5). The requirement of interelement continuity is also relevant for the cancellation of the $\ln(\varepsilon)$ terms which appear in the derivation of the self and adjacent hypersingular integral contributions.
Reviewing the origin of the contributions of the free terms, the first term, $\Pi_{\text{sing, adj}}$, comes from the adjacent contributions and is one part of the analytically evaluated singular integral parts. The explicit expression for $Q_A(u, 0)$ in Eq. (3.34) is derived on the basis of the second cancellation requirement of the $\ln(\varepsilon)$ terms. Whereas this explicit expression just depend on the enclosing angles of the tangent vector and simplifies to unity if the second cancellation requirement holds, the $\ln(s_A)$ term depend on both the element ratio and the enclosing angle.
The second part $\Pi_{\text{FT, adj+self}}$ represents a symmetric Galerkin specific free term. This term vanishes if the tangent vector of the elements have interelement C^0 continuity (geometric function space requirement), see [19]. Consequently, this term is non zero if one of the element endpoints is a corner, because the tangent vectors are no longer continuous over the adjacent, corner sharing elements.
The third term, $\Pi_{\text{endp, self}}$, originating from the hyper singular integral formulation of the self case, contain the endpoint values of the source element and the element ratio.

Error analysis and derivation of new free term formulation The analysis of the free term in cBEM indicated that with an element ratio of one and a discontinuous geometry representation, the solution of cBEM converged to a reasonable small value. With changing the element ratio, the solution became incorrect. Accounting the interelement C^0 continuity requirement and applying a corresponding quadrature rule in a test case environment, the solution converged for an arbitrary element ratio and a discontinuity but only for a Dirichlet BVP. For a Neumann BVP or a mixed BVP the solution function is defined at least partly by the normal derivative of the potential $\partial\phi/\partial n$. The incorrect result was assumed to originate from the non-unique normal derivative at the corners due to the normal vector discontinuity. Consequently, a continuous quadrature that explicitly considered non-unique end point values gave incorrect results. As this case had worked for an element ratio equals one, the use of discontinuous basis function could overcome this problem, because instead of explicitly accounting and fixing the endpoints, in the discontinuous quadrature rules as Gauss-Legendre, the endpoints are extrapolations of the parametric coordinate interval interior collocation points. (A different solution is to split the corner point as done in other BIE approaches, see Sec. (1.2.3), or in the symmetric Galerkin BEM, see e.g. Sutradhar et al. [162].)
Having this in mind the idea was to separate the solution function spaces of the potential ϕ and the normal derivative of the potential $\partial\phi/\partial n$ and apply continuous and discontinuous quadrature rules respectively. This allowed a comparison to the original cases.
The account of $\ln(\chi)$ as additional term in the free term evaluation, Eq. (3.32), gave the correct solution. The new free term formulation is therefore given by

$$\phi(z)\psi(z)D_A = \phi(z)\psi(z)\Big(\frac{1}{2\pi} + \frac{\ln(\chi)}{4\pi} + \frac{(1-\chi^2)\ln(\chi) - 2\chi\beta'\sin(\beta')}{4\pi(1+\chi^2-2\chi\cos(\beta'))}\Big) \tag{3.38}$$

As the additional term had vanished obviously for $\chi = 1$, it was overseen until the element ratio was changed to an arbitrary value.

3.4 Verification of developed methods

In this section the developed methods that have been described in the previous sections are tested according to suited analytic reference solutions. By showing that the results of cBEM had reasonable small error and expected convergence order to the reference, the developed methods, specifically those used for the operator assembly and desingularization, had been verified. The proof of the consistent implementation in cBEM was essential and gave the basis for applying cBEM for hydrodynamic problems.

3.4.1 Verification fsBEM

The first development stages included the implementation of the fsBEM solver which was used to prove the first two research hypotheses which states that a suited BEM approach converge to the first order HOS solution (RH1) and that a boundary separated in two parts can be treated by assembling two operators and their union gives the results in the same order of accuracy as with the continuous approach (RH2). The related research questions addressed the BIE method, the BIO desingularization and the accuracy of the approach. The answers to these questions and the verification of the approach were shown under the assumption of linearity by evaluating the result of the fsBEM and compare it to the first order HOS solution

$$\frac{\partial \phi_S}{\partial n} = W = -\kappa \phi_S \tag{3.39}$$

with the κ-operator, see Eq. (2.95) and West et al. [184], Eq. (17). The equality $\frac{\partial}{\partial n} = \frac{\partial}{\partial z}$, was valid as the evaluation is on the linearized free surface $z = 0$. The minus sign came from the normal definition in negative z-direction which is opposite from that accounted in West et al.'s approach.
The property of this reference solution to rely on a trigonometric function, by defining ϕ_S correspondingly, allowed an error analysis with no minimal error limit due to the inability of any polynomial to exactly approximate trigonometric functions.
In the following, the test cases for the continuous and the discontinuous fsBEM are described and the results presented.

Continuous water boundary

The formulation of the BIE and the desingularization of the Hypersingular BIO were most important for the set up of the continuous fsBEM. To be consistent with the numerical HOS approach of West et al., where the normal derivative is solved for at every subsequent nonlinear order, the NDBIE, Eq. (3.11), was chosen to evaluate. The desingularization of the Hypersingular BIO was done according to the direct approach for symmetric Galerkin BEM following Bonnet & Guigianni [19]. By the application of basis functions of interelement support by means of second order Z-Spline the appropriate approximation of the spectral HOS basis functions was given.

Considering the linearized free surface domain, with a normal component only in the direction of the second coordinate, the Adjoint BIO equals zero so that the final BIE resulted in

$$\gamma_1 \phi_S = 2\mathcal{H}\gamma_0 \phi_S. \tag{3.40}$$

Outline of the problem The paramters for the continuous fsBEM test case are defined in Tab. (3.1). Following the Dirichlet BVP Eq.(3.9) illustrated in Fig. (3.7), the free surface potential was used as Dirichlet datum and the Laplace solution had to be satisfied in the exterior domain. At the lateral boundaries of the free surface, the Method of Farfield Extension was applied to approximate the periodic boundary condition. The integration order for the adjacent and self influence evaluations were chosen to $N_{int,adj} = 20$ and $N_{int,self} = 10$ respectively.
The error was analyzed by accounting the wave length and the domain size as constant so that an increase of the number of elements yielded a decrease of the element size and a higher resolution of the

Table 3.1: Parameters of free surface, discontinuous boundary and computations for verification of continuous fsBEM.

Free Surface		Discont. Boundary		Comp. Param.	
λ	10	discont.	0	N_W	[10, 30, 50, ..., 230]
ε	0.015	West	-		
D	10^5	East	-	N_{Im}	10

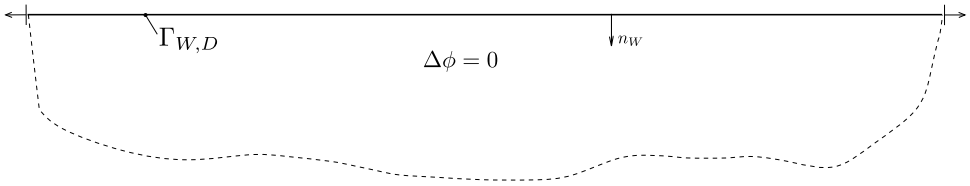

Figure 3.7: Test case fsBEM continuous with the free surface boundary shown by the black line. The arrows on the left and right end of the boundary mark the application of the Method of Farfield Extension.

geometry (h-refinement). The auxiliary lines in the lower left part of the convergence studies shown below indicate the slope for the second and fourth order error decay and should help to quickly determine the order of convergence to the analytical solution.

Results and discussion The error between the fsBEM solution of the Neumann datum at the free surface and the first order HOS solution are presented in Fig. (3.8) by means of the E_{L2} error norm over the increasing number of free surface boundary elements (h-refinement). The convergence order of the error is $\mathcal{O}(E) = -4$ and corresponds to the integration order expected from the use of Z-Splines of second order for the solution representation. The minimal error $E_{L_2,min} \approx 6.3 \cdot 10^{-6}$ was reached after a grid spacing of $dx_W = 0.125$ and corresponds to the error that is induced by the hypersingular kernel approximation. The results indicate that the first research hypothesis could be proven by the fsBEM. Furthermore, the applied assembly of the symmetric Galerkin Hypersingular BIO including desingularization and the use of interelement basis functions, the chosen BIE formulation, the geometry evaluation and the application of the Methods of Farfield Extension could be verified with the reasonable small error between the first order HOS solution Eq. (3.39) and the associated convergence order.

Discontinuous water boundary

The account of a discontinuity on a boundary was of high relevance for the development of the cBEM because it allowed the setup of a mixed BVP containing the free surface domain and the truncated body boundary domain (only submerged body) that replaced the discontinuous water boundary part. From the prove of the first research hypothesis it followed that the global HOS approach was accurately approximated by a local BEM operator. The property of compact support allowed the account of truncated boundaries because the element related influences had been explicitly evaluated and assembled. A truncation of a modal basis function as applied in spectral methods was not an option because there is no solution to continue the function, the requirements on smoothness were not fulfilled anymore and the property of global support would directly affect the rest of the collocation points in terms of the changing contribution associated with the truncation.
The main complexity for the discontinuous fsBEM was the desingularization of the Hypersingular BIO in the presence of the discontinuity, described in Sec. (3.3.1).

Outline of the problem The testing of the developed symmetric Galerkin method was done on a similar test set up as for the continuous approach but with accounting a discontinuous part, see Fig. (3.9). The parameters for the water domain, the discontinuity as well as the simulation parameters are given in Tab. (3.2). The positions of the westish (left) and the eastish water boundary intersections define the coherent, inner discontinuous part and the remaining free surface part of the water domain The

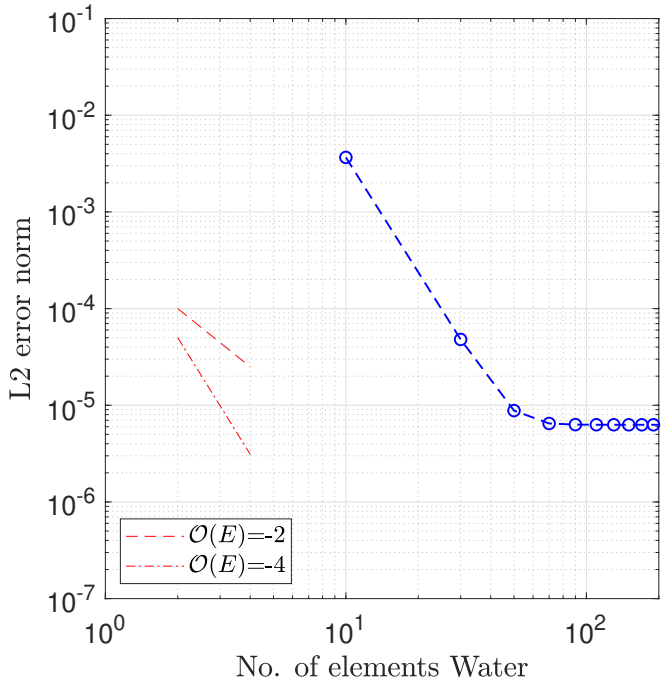

Figure 3.8: Convergence of continuous fsBEM to first order HOS solution. The error according to the L_2 error norm with grid refinement on the water surface for the cBEM solution and the analytic reference is shown by the blue circles. In the south west part of the figure, the red dashed and dash dotted line represent the slope for convergence orders $\mathcal{O}(E) = -2$ and $\mathcal{O}(E) = -4$.

Table 3.2: Parameters of free surface, discontinuous boundary and computations for verification of discontinuous fsBEM .

Free Surface		Discont. Boundary		Comp. Param.	
λ	10	discont.	1	N_W	[10,20,40,80]
ε	0.015	West	0.2 λ		
D	10^5	East	0.8 λ	N_{Im}	10

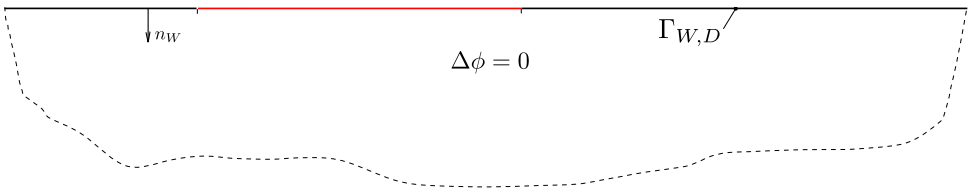

Figure 3.9: Test case fsBEM discontinuous with the discontinuous water boundary domain part highlighted in red and the free surface part in black.

influences that corresponded to the elements of the free surface and the discontinuous boundary part were assembled in two individual Hypersingular BIOs, H_{FSB} and H_{DCB}.

Results and discussion The summation of the operators that represent the two separated domains yielded the full domain operator

$$\mathcal{H} = \mathcal{H}_{\mathcal{FSB}} + \mathcal{H}_{\mathcal{DCB}} \tag{3.41}$$

which was accounted for the Neumann datum. The error E_{L2} was evaluated by considering the first order HOS solution, Eq. (3.39), as reference and the results with h-refinement are shown in Fig. (3.10).

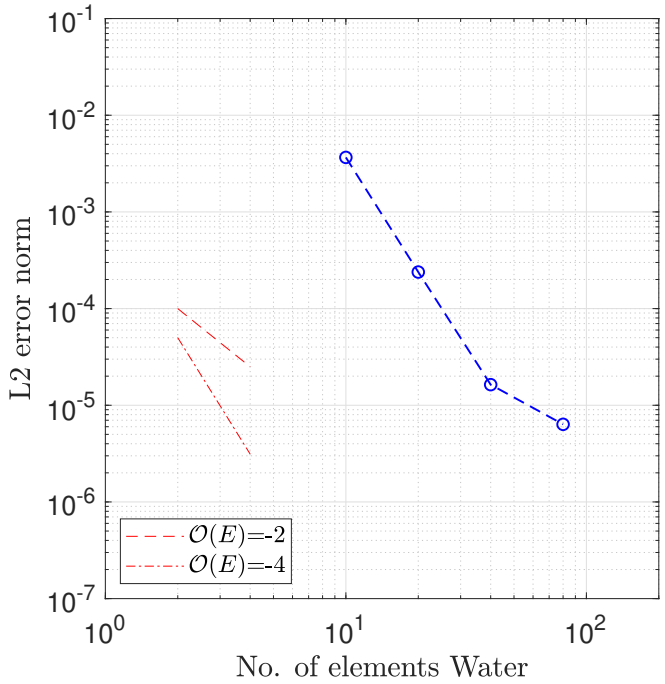

Figure 3.10: Convergence of the error of the Neumann datum at the free surface boundary (blue circles) compared to the first order HOS solution for the discontinuous fsBEM. Slopes for two convergence orders are shown in the south west part of the figure.

Both the convergence of the error and the minimal error level are equal to that shown for the continuous fsBEM and verified the procedures that had been developed for the handling of the discontinuous boundary part, including the geometric evaluation of the boundary intersections and the desingularization approach for the Hypersingular BIO. This proved RH2 as the reunion of the two set of boundary elements before solving the fsBEM gave the same results as accounting the complete set of the boundary elements.

In addition to the results with Z-Splines, the test cases had been repeated with Lagrange basis functions that are of intraelement support. The farfield integration order was chosen to four, in line with the order of the above analyzed interelement basis functions. The result in terms of the L_2 error norm are shown in Fig. (3.11) in that the left panel represents the continuous and the right panel the discontinuous free surface. Compared to the results with Z-Spline solution approximation, given in Figs. (3.8) and (3.10), the error at the lowest resolution $dx_W = 1$ was smaller. As the order of the error decay was same, the minimum error was reached already at a grid resolution of $N_W = 50$. This led to the conclusion that the increase of the influence region of the basis function requires a higher resolution compared to intraelement basis functions. It has to be noted that the error at the lowest resolution with interelement basis functions already represent a reasonable small accuracy level for hydrodynamic problems.
The minimum error is same for both types of basis functions and confirmed that the small error originates not from the solution approximation but from the maximal accuracy that can be found for the integral kernel with the chosen parameter set (integration order for the influences of adjacent and self regime).

3.4.2 Verification cBEM - Stationary solver

The formulation and set up of a monlithic coupling approach for wave and body dynamics defined the next development stage. As the cBEM solves a mixed BVP, the direct formulation, Eq. (3.8), employs all BIOs. Additional to the Hypersingular W2W BIO, therefore the B2B and the Coupling BIOs were necessary. The former ones were taken from the frequency domain BEM developed by Schwarz [150] and modified to the symmetric Galerkin approach. The assembly of the Coupling BIOs considered different

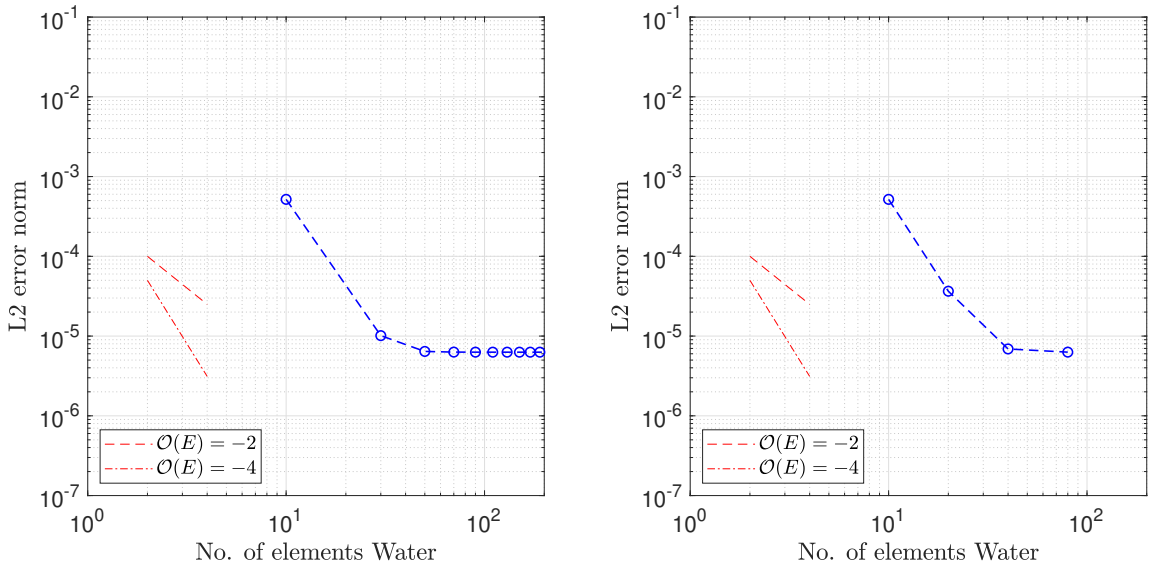

Figure 3.11: Results with intraelement basis functions for the decay of the error (blue circles) between continuous (left panel) and discontinuous fsBEM and first order HOS solution.

discretizations of the solution function space of the Neumann and Dirichlet boundary in terms of using inter- and intraelement type basis functions, see Subsec. (3.2.3).
The considered analytic reference solution was derived from the LWT, see Subsec. (3.2.4). By prescribing the Neumann datum at the body surface and the Dirichlet datum on the free surface the corresponding unknown densities could be evaluated. By this way of defining the boundary conditions the body was treated as invisible for the free surface wave and allowed the verification of the approach in the absence of wave radiation and diffraction. As for the HOS solution, the error of the cBEM solution with respect to the analytic LWT could theoretically decay to machine precision so that a reached error limit would identify another dominant error source.
Again the continuous problem was considered first before stepping forward to the discontinuous case. The latter included the development of an adjacent desingularization procedure and formed the next large development stage.

Continuous cBEM - Submerged body test case

As the fully submerged body with sufficient distance to the free surface was accounted, the following tests addressed the verification of the Farfield assembly of Coupling BIOs, the direct BIE formulation chosen for the cBEM and the method's implementation.

Outline of the problem The general test case setup is illustrated in Fig. (3.12). The distance between the center of the geometry (x_c, z_c) and the linearized $(z = 0)$ free surface boundary $\Gamma_{W,D}$ is denoted by h and the edge length of the rectangular geometry by a. The mixed BVP is defined by Eq. (3.3) and the boundary conditions are of Dirichlet type at the free surface and of Neumann type at the body boundary $\Gamma_{B,N}$.
The parameters of the case are given in Tab. (3.3) and include the body parameters, the free surface and the simulation parameters. The number of body boundary elements per edge length increased with the number of water boundary elements.

Results and discussion The results are shown by means of the error E_{L2} between the analytic reference and the cBEM solution, see Figs. (3.13) and (3.14). Corresponding to the formulation of the mixed BVP, the Neumann and the Dirichlet datum are analyzed at the free surface and at the body surface, respectively.
The Neumann error over decreasing free surface element size is presented in Fig. (3.13). The convergence

Table 3.3: Parameters of free surface, rectangular geometry and computations for continuous cBEM.

Free Surface		Body		Comp. Param.	
λ	10	a/2	1	N_W	[10,20,40,80]
ε	0.015	a/h	0.4	N_B per edge	[5,10,20,40]
D	10^5m	(x_c, z_c)	(5, -5)	N_{Im}	10

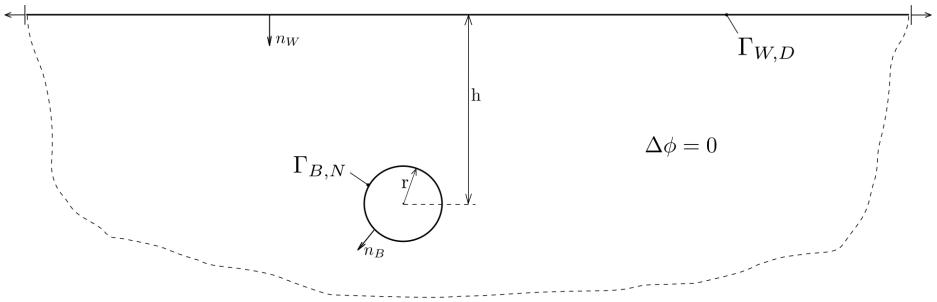

Figure 3.12: Test case submerged body.

order is consistent to the expected integration order from the Z-Splines. The convergence characteristic is similar to that shown for the fsBEM including the minimum error which was also here considered representing the accuracy of the BIO evaluations.
Figure (3.14) show the solution of the Dirichlet error over increasing number of body elements. The rate of convergence decreases before the error reach a minimum which is about one order of magnitude higher than for the water surface.

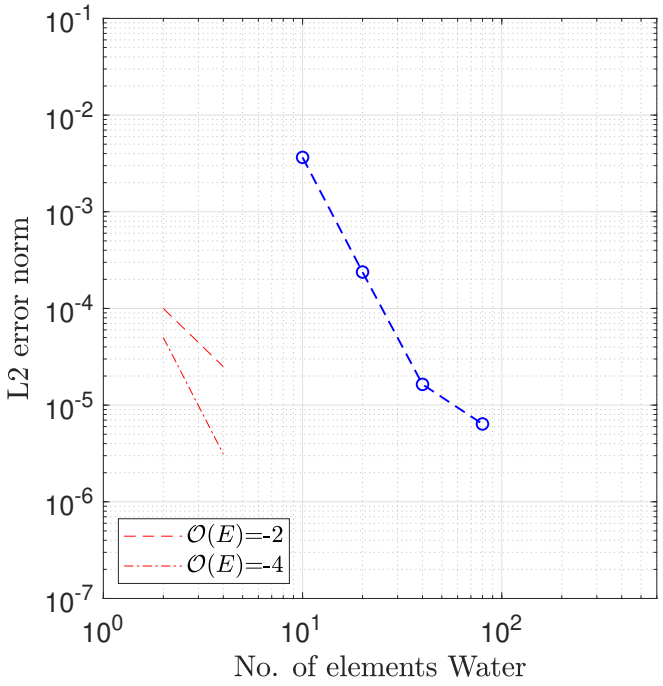

Figure 3.13: Convergence of the free surface error in cBEM (blue circles) with respect to the LWT reference with h-refinement at the water domain. The submerged rectangular cylinder was considered. Slopes for two convergence orders are shown in the south west part of the figure.

The small errors and the reasonable convergence orders with decreasing element size for the solutions at both the body and the water surface verified the cBEM and the developed methods including the

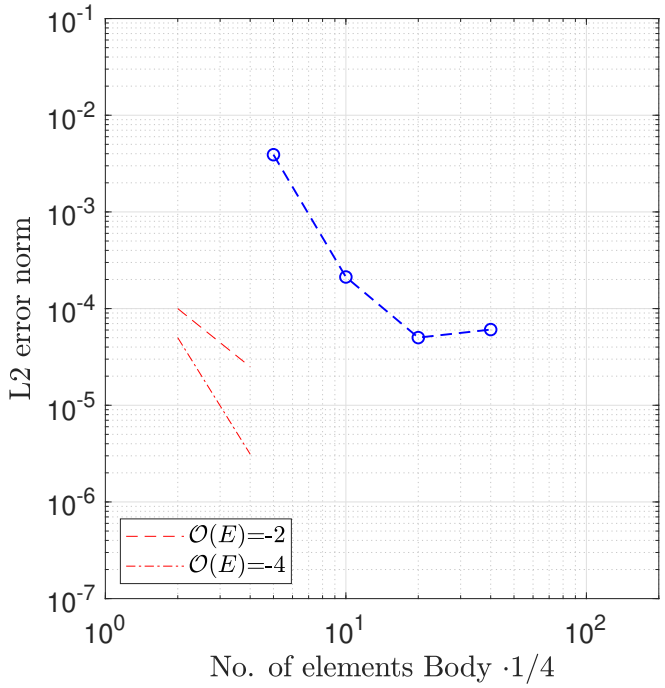

Figure 3.14: Error for the Dirichlet datum (blue circles) at the submerged rectangular body surface with increasing number of body elements. As reference the LWT solution was considered.

assembly of all eight BIOs. This proved the RH3 for that firstly the coupled solver had been considered.

The replacement of the Z-Splines by Lagrange polynomials is presented in Fig.(3.15). The lower error niveau for the solution at the free surface as well as the faster achievement of the minimal error is visible in the left panel and consistent with the results for fsBEM using intraelement basis functions. In the right panel, the constant error with h-refinement at the body surface, highlights that the error is

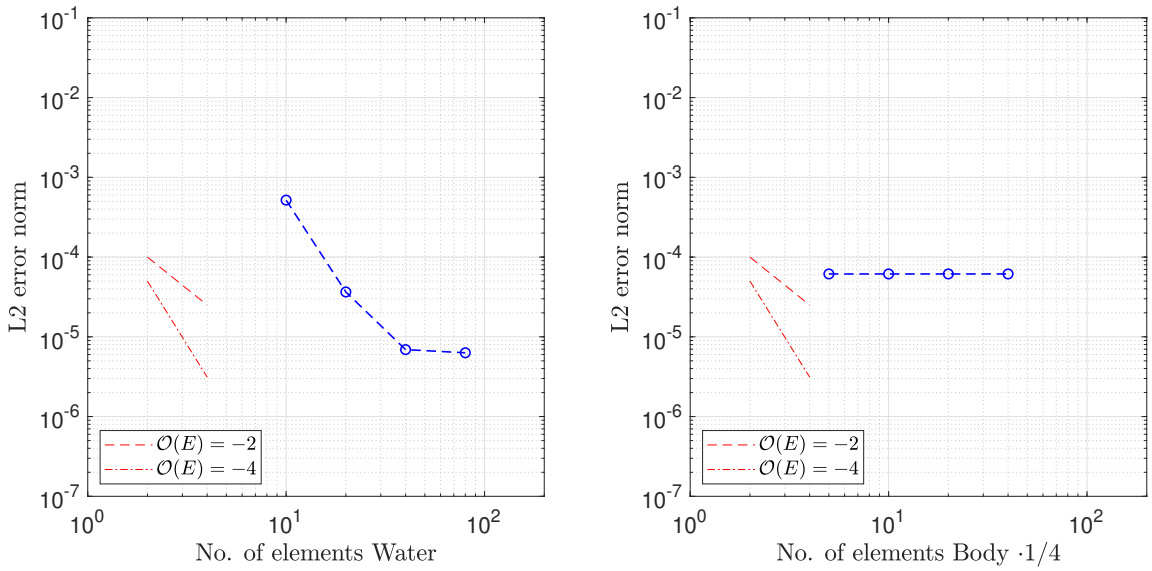

Figure 3.15: Error decay with intraelement basis functions for the submerged rectangular geometry. The numerical solution of cBEM (blue circles) was compared with the reference solution from LWT. In the left panel the solution of the Neumann datum at the free surface is shown over the number of elements on the water domain. The right panel shows the Dirichlet datum at the body surface over body elements.

not dominated by the approximation of the solution, but by an either geometry-, assembly- or setup-related, more dominant error. As the error is constant from the beginning, which was not the case when interelement basis functions had been used for the free surface, the periodic definition of the Z-Splines and the Method of Farfield Extension could give a discrepancy at lower resolution. For the intraelement approximations, the definition of periodicity was not necessary so that the lower error at higher grid spacing is comprehensible.
The matching results for both types of basis function approves the approach of the interelement basis functions for the cBEM.

For the surface piercing case, adjacent and near influence kernel evaluation for the four Coupling BIOs were required.

Verification cBEM - Near and adjacent-regime of coupling operators

The testing of the coupling kernel evaluations in the near and adjacent regime, see Sec. (3.3.2), required a simplified test environment that allowed the verification in the case of the Hypersingular BIO.
For this, a test case introduced in Bonnet & Guiggiani [19] was considered. It gives an analytic reference for Hypersingular BIO in symmetric Galerkin formulation that was found by the analytic integration of the kernel. The solution depend solely on the element ratio χ and the enclosing angle β. The account of the corner and the variable element size in the setup, represented the intersection elements in cBEM already quite well.

Outline of the problem To take basis functions of interelement support into account and to analyze the influence of a nearfield element, the original test case was modified and used as sketched in Fig. (3.16).
The highlighted case in Fig. (3.16), exemplary show five W elements resulting from four W elements to account the interelement influence of the Z-Spline basis functions of second order (adjacent element W_{III} with influences on W_{II} to W_V) and one additional element for switching to the nearfield element (here W_{II} with influences on W_I to W_{IV}). On the element B_I an intraelement basis function was chosen for that three collocation points was considered as in the original set up in [19]. The boundary data are given

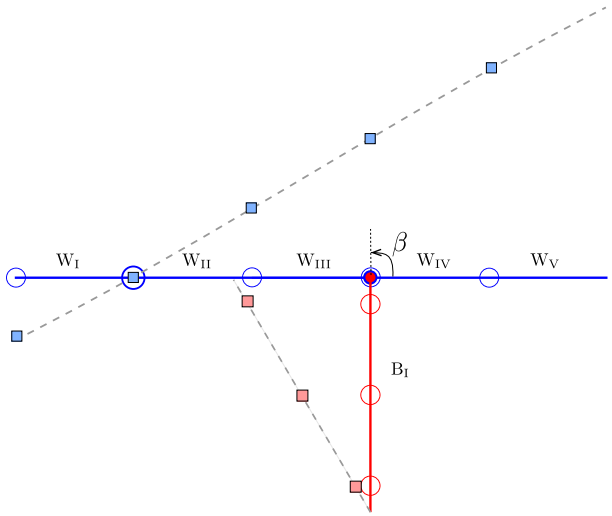

Figure 3.16: Test case desingularization for Coupling BIOs (hypersingular, adjacent case, nearfield influence).

as linear functions (dashed gray line). The collocation point values are indicated by the colored quaders, where red and blue denote the relation to the B and W boundary elements.

Results and discussion The verification of the implementation of the Hypersingular BIO can be shown by Figs. (3.17) where the absolute error of the Hypersingular integral value $|(H_{ref} - H)|$ is plotted over the integration order of the Adjacent element on the left panel. The decay of the error up to $1 \cdot 10^{-8}$ at a sufficiently large integration order at the adjacent (W_{III}) and near element (W_{II}), $N_{Int,adj} = 5$ and

$N_{Int,near} = 12$ indicated the correct implementation. The right panel in Fig. (3.17) represents the error at varying integration order at the near and adjacent element. It is shown that a minimum number of integration points on both the near and adjacent element is required ($N_{Int,adj} > 8$, $N_{Int,adj} > 3$) for a sufficiently small error. In Tab. (3.4) the results of the convergence study are presented and the errors

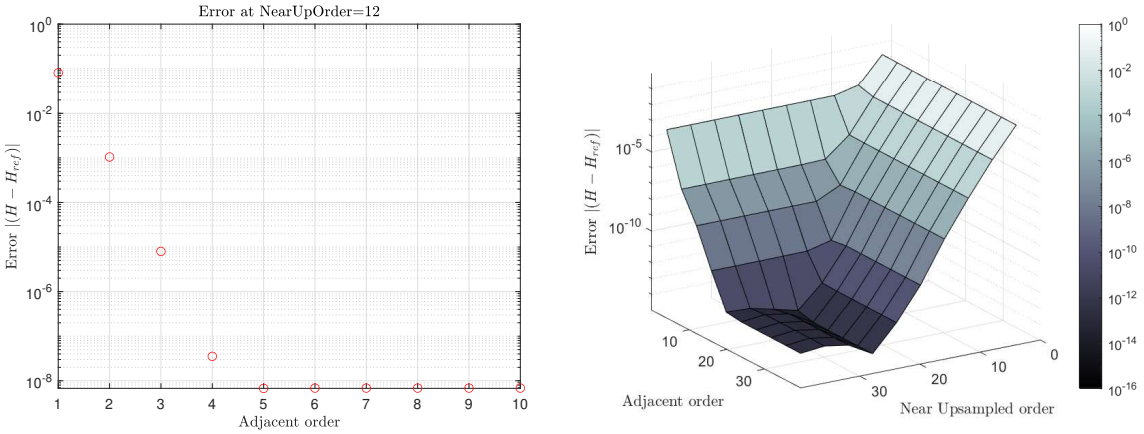

Figure 3.17: Results of test case for direct approach. Left figure represent error (red circles) for near-regime integration order of 12 and corresponding convergence to the analytic reference with increasing adjacent order. Right figure shows absolute error for different integration orders of the adjacent and near-regime element.

for the Hypersingular BIO with respect to the reference given in Bonnet & Guiggiani [19] for varying integration orders of the near and adjacent element are given. Additionally, the integrated values of the Single, Double and Adjoint Boundary Integral Operators are presented. As the verification of the Hypersingular BIO was in focus in Bonnet & Guiggiani [19], these explicit values for the weaker singular BIOs in connection with this test case are firstly presented to the author's knowledge. The verification

Table 3.4: Error of integrated value of Hypersingular BIO to reference given in [19] and integrated values of other BIOs for various integration orders.

Integration order Near	Adjacent	$\lvert\mathcal{H} - \mathcal{H}_{ref}\rvert$	$\mathcal{S}$	$\mathcal{D}$	$\mathcal{A}$
2	2	0.401	-0.164437312929550	0.003103390475837	
4	4	0.081	-0.164544356950061	0.002876039154965	
8	8	0.001	-0.164541112820128	0.002909644415416	$-\mathcal{D}$
16	16	4.215E-08	-0.164541113932961	0.002909632358876	
32	32	1.399E-13	-0.164541113932968	0.002909632358646	

of the adjacent desingularization method for the Coupling BIOs allowed to step forward to the testing of the discontinuous cBEM.

Discontinuous cBEM - Surface piercing body test case

The discontinuous cBEM test case marked a significant step in the development of cBEM as thereby the target set up, the modeling of a surface piercing body in waves was checked. The account of the problem as mixed BVP and the application of a direct BIE approach in symmetric Galerkin formulation, cBEM, represent an innovative numerical approach in terms of tailored desingularization methods, treatment of the free surface discontinuity and the coupled account of the free surface boundary and the body boundary.

Outline of the problem The formulation of the problem is given in Eq. (3.3) and the computational details, the wave and body specification are listed in Tab. (3.5). The test case to the exterior problem

Table 3.5: Parameters of free surface, rectangular geometry and computations for discontinuous cBEM test case.

Free Surface		Body		Comp. Param.	
λ	32	a/2	4	N_W	[32,64,128,256]
ε	0.015	a/h	-	N_B	[4,8,16,32]·2
D	$1 \cdot 10^5$m	(x_c, z_c)	(16,0)	N_{Im}	10

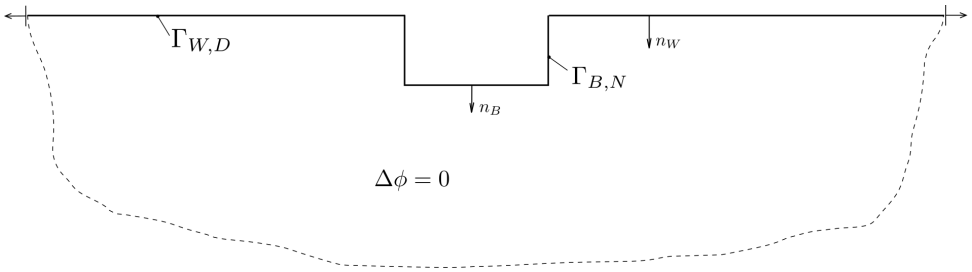

Figure 3.18: Test case cBEM with surface piercing body.

is sketched in Fig. (3.18) and provides the definitions of the normal vectors and the boundaries. For the lateral boundary conditions of the free surface again the Method of Farfield Extension was used.

Results and discussion As reference, the analytic LWT solution was used and the Dirichlet and Neumann datum were defined on the free surface and body boundary domain respectively.
For the Neumann datum at the free surface, the comparison to the previous plots indicate a larger error for $dx_W = 1$ and a lower convergence order about $\mathcal{O}(E) = -2$. Both are related to the here considered mixed boundary domain representing the union of the free surface $\Gamma_{W,D}$ and body boundary $\Gamma_{B,N}$, see also Fig. (3.18). The truncation of the boundary domain and the consideration of the Dirichlet-Neumann corners increase the error and lowers the integration order. But still the error at the free surface and the body surface, Figs. (3.19) and (3.20) respectively, is low.

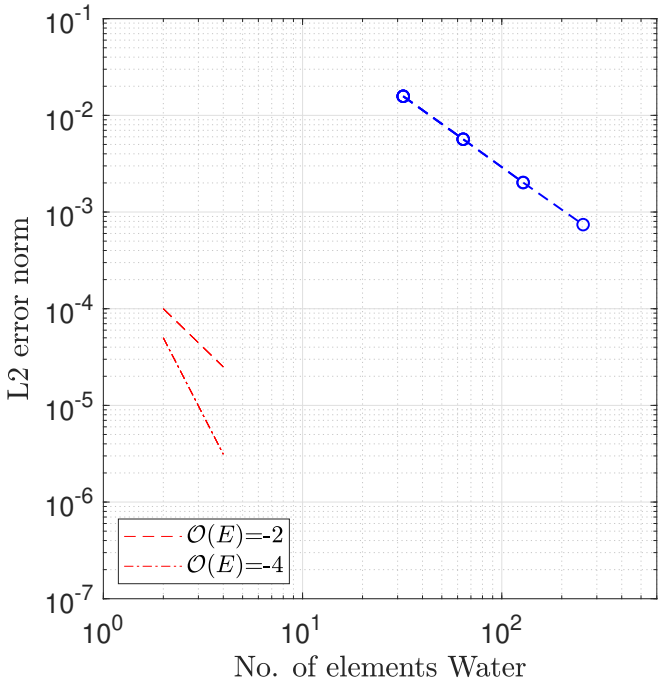

Figure 3.19: Results of cBEM for the Neumann datum at the free surface in terms of the L_2 error norm shown by blue circles for the surface piercing body.

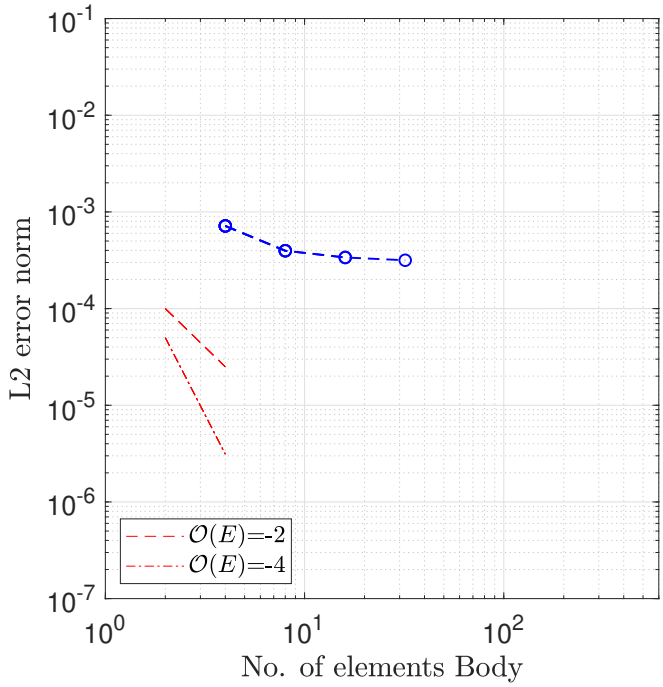

Figure 3.20: Results of cBEM for the Dirichlet datum at the body surface in terms of the L_2 error norm shown by blue circles for the surface piercing body.

The Dirichlet datum at the body surface is only slightly influenced by the h-refinement of both the water and body boundary and reach already at a lower resolution the error level of $E_{L_2,min} = 3 \cdot 10^{-4}$. As this is one order of magnitude higher than the error level shown for the submerged body test case, also here the neighboring Dirichlet-Neumann boundaries and the related evaluation influenced the solution.

The Method of Farfield Extension affected the solution which is shown in Fig. (3.21). The decrease of the number of images caused a decrease in the convergence order and an increase of the error minimum when considering the interelement basis functions, presented in the left panel. The latter can be seen from the right panel as well. Here the shift towards higher L_2 errors clearly indicate the sensitivity to the choice of the number of images. Conclusively, the number of images set the error niveau and their choice remain a balancing between efficiency and accuracy.
Employing basis function of intraelement support for the solution approximation of the free surface, did not affect the error for the body solution, shown in the right panel of Fig. (3.22). In contrast, the error for Neumann solution at the free surface shows no convergence with h-refinement for this type of basis function and the error at higher grid resolutions is larger compared to the solution found with Z-Splines. It was concluded (with respect to this case) that the application of interelement basis function and the related convergence with h-refinement yielded lower error solutions at the cost of a higher number of elements. The account of the neighboring elements' influences (increase of the region of compact support) explained the favorable convergence characteristic for this basis function type. The reasonably small error for the initially unknown Dirichlet and Neumann datum, shown in Figs. (3.20) and (3.19), highlights the valid implementation of all eight BIOs for the discontinuous cBEM approach. This step marked a relevant proof of concept and allowed to close the stationary assembly development and step forward to the transient case.

3.4.3 Verification cBEM - Time domain solver

In the following section, the verification of the time stepping in cBEM is tested and the transient solutions computed are presented and analyzed. The governing research questions was the stability of the

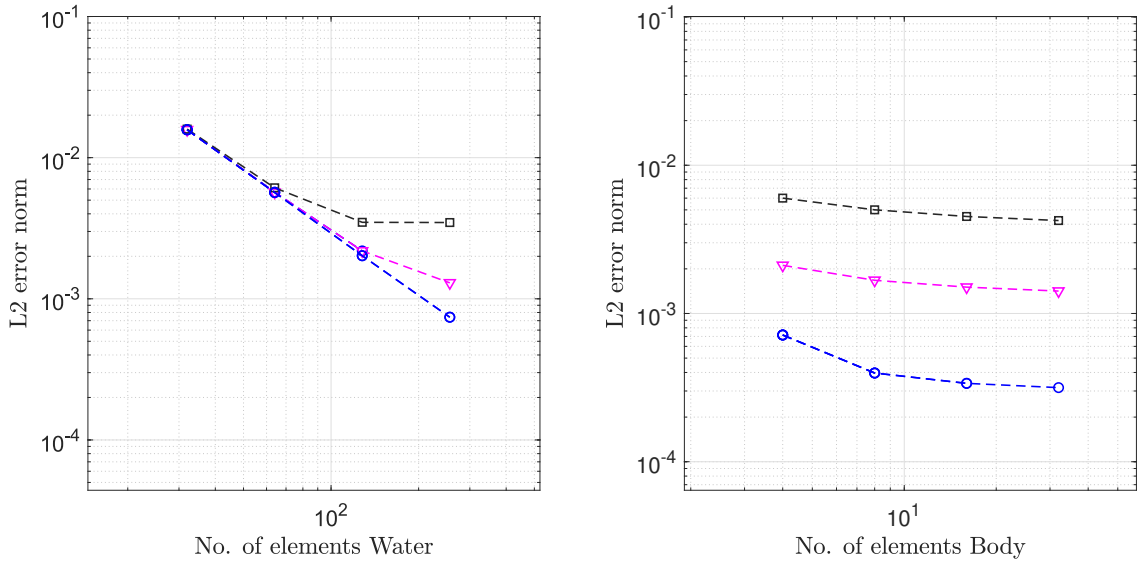

Figure 3.21: Error for different number of images for the Neumann datum (left panel) and Dirichlet datum (right panel). The blue colored circles represent $N_{Im} = 10$, the magenta triangles $N_{Im} = 5$ and the dark gray squares $N_{Im} = 3$.

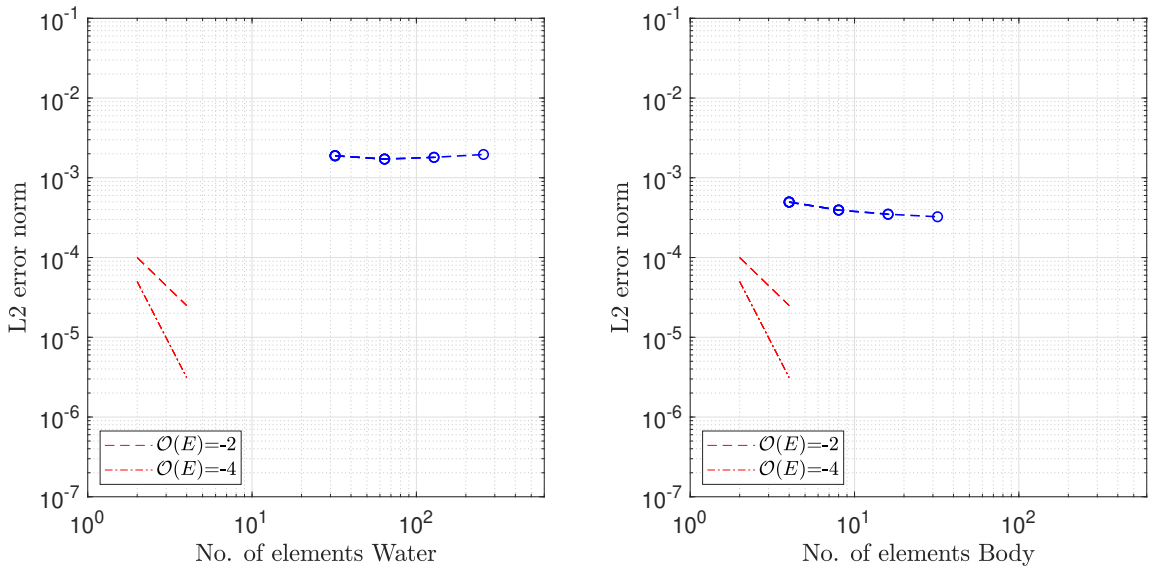

Figure 3.22: Error decay with intraelement basis functions for the surface piercing rectangular geometry. The numerical solution of cBEM (blue circles) was compared with the reference solution from LWT. In the left panel the solution of the Neumann datum at the free surface is shown over the number of elements on the water domain. The right panel shows the Dirichlet datum at the body surface over body elements.

implemented RK4 method, see Subsec. (3.2.3) and Eq. (3.19), for the time integration of the considered wave dynamics.

The investigations were made by using again the analytic LWT reference, Eqs. (3.24) and (3.25). At every time step, the Neumann condition on the submerged body surface had been defined accordingly to the updated free surface boundary condition so that the body was defined to be transparent for the wave. To be consistent with the fourth order time stepping scheme, a Taylor expansion was used to compute the Neumann value at the three time stages of the RK4 scheme, see Eq. (3.20).

The time domain results of the continuous and discontinous cBEM are analyzed next by means of stability

and accuracy.

Continuous transient cBEM - Submerged body test case

Submerged cylinders in unsteady potential flows and their effect on the free surface are treated in a variety of standard test cases for hydrodynamic solvers. The evaluation of the forces in the diffraction or radiation problem, e.g. Ogilvie [133], or the stationary wake behind the body in a current flow, e.g. Tuck [166], are three typical examples and are used for the validation of cBEM in Sec. (4). The analysis of the transient solutions of these problems in terms of stability and accuracy are therefore of relevance for the targeted application of cBEM to hydrodynamics.

Outline of the problem For the verification in time domain a single wave with wave length equal to the length of the computational domain was considered. The parameters used for the simulations are shown in Tab. (3.6)

Table 3.6: Parameters of free surface, body and computations for continuous transient cBEM.

Free Surface		Body		Comp. Param.		Comp. Param. Time	
λ	64m	r	1m	N_W	64	dt	1E-2
ε	0.015	r/h	0.2	N_B	16	t_{sim}	20
D	10E5	(x_c, z_c)	(32,- 5)	N_{Im}	10	RK order	4

Results and discussion In Fig. (3.23) the free surface elevations at five time steps within the simulation

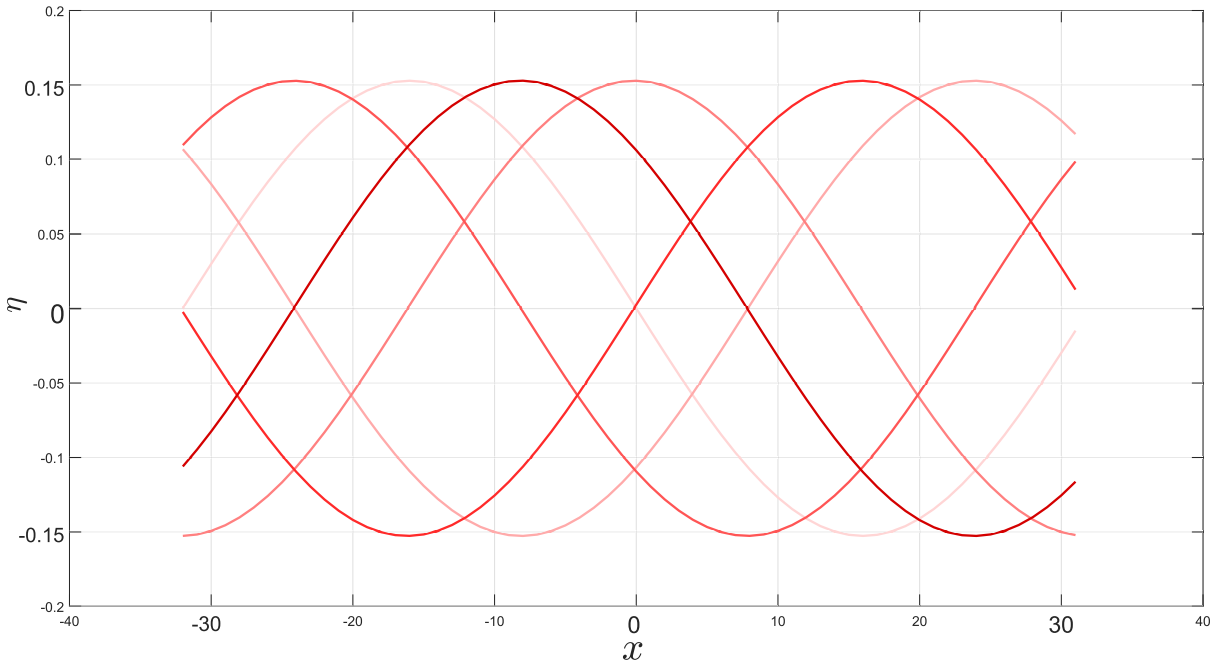

Figure 3.23: Results of cBEM discontinuous in terms of free surface elevation in space domain at five distinct time steps (light to dark indicate the time evolution). The body is located below the free surface at $x_c = 0$.

time of $t_{sim} = 20\,\mathrm{s}$ are presented. It is shown that the shape and the amplitude of the free surface did not change with time which implies that the computation of the time integrated wave variables and the update of the body Neumann condition according to LWT worked. As the surface elevation was directly evaluated by the RK4 scheme, this result indicate the stability of the time domain solver.

Discontinuous transient cBEM - Surface piercing body test case

The prove of the stability for the transient solver in the surface piercing case is of even more interest as the discontinuous case depict the target application of cBEM, the analysis of ship motion in time domain. As derived from the results of the stationary solver, the accuracy of the solution was slightly reduced due to the truncation of the boundary domain and the solution behavior was more unclear for the time integration.

Outline of the problem For the verification of RH5, the test computational setup was chosen similar to the continuous transient test case with some changes in the discretization parameters, see Tab. (3.6). The characteristic length to domain length ratio was $a/\lambda = 1/8$ which represent a relative high value

Table 3.7: Parameters of free surface, body and computations for discontinuous transient cBEM.

Free Surface		Body		Comp. Param.		Comp. Param. Time	
λ	32m	a/2	2m	N_W	128	dt	7.81E-3
ε	0.015	a/h	-	N_B	32	t_{sim}	10
D	10E5	(x_c, z_c)	(16, 0)	N_{Im}	10	RK order	4

of this ratio. In more realistic scenarios, the boundary domain will be extended as higher wave length are relevant to capture and cause a decreasing ratio. On the other hand, the fictitious resolution of the discontinuous boundary part $a/dx_W = 16$ is moderate and could be reduced down to a ratio of $a/dx_W \geq 2m_{ZS}$ as this ensures that enough ghost elements for the interelement basis functions are given.

Results and discussion The results in terms of the free surface elevation in space domain are given

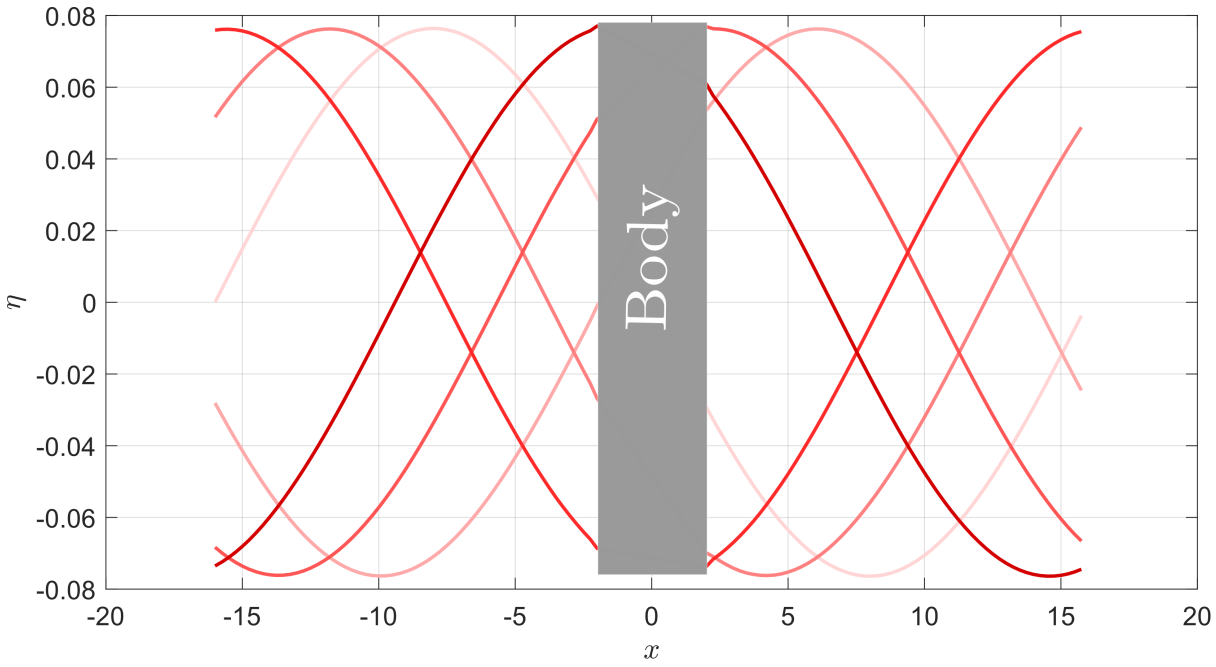

Figure 3.24: Surface elevation in space domain for cBEM discontinuous at five distinct time steps (light to dark indicate the time evolution). The body is located in the middle of the computational domain and its horizontal dimension is illustrated by the gray rectangle.

in Fig. (3.24) at five discrete time steps. As in the case of the submerged body, the surface elevation was constant over the simulation time and represent the stability of the transient solution for the surface piercing body.

The accuracy was analyzed by evaluating the error at the body and water surface at the shown time steps, see Figs. (3.25). The upper panel displays the difference of the normal derivative of the LWT reference

and the cBEM solution in terms of the L_2 error norm. After an increase of the solution in the first to measures, the error stayed below 10^{-2} on relatively constant level. The error of the Dirichlet value at

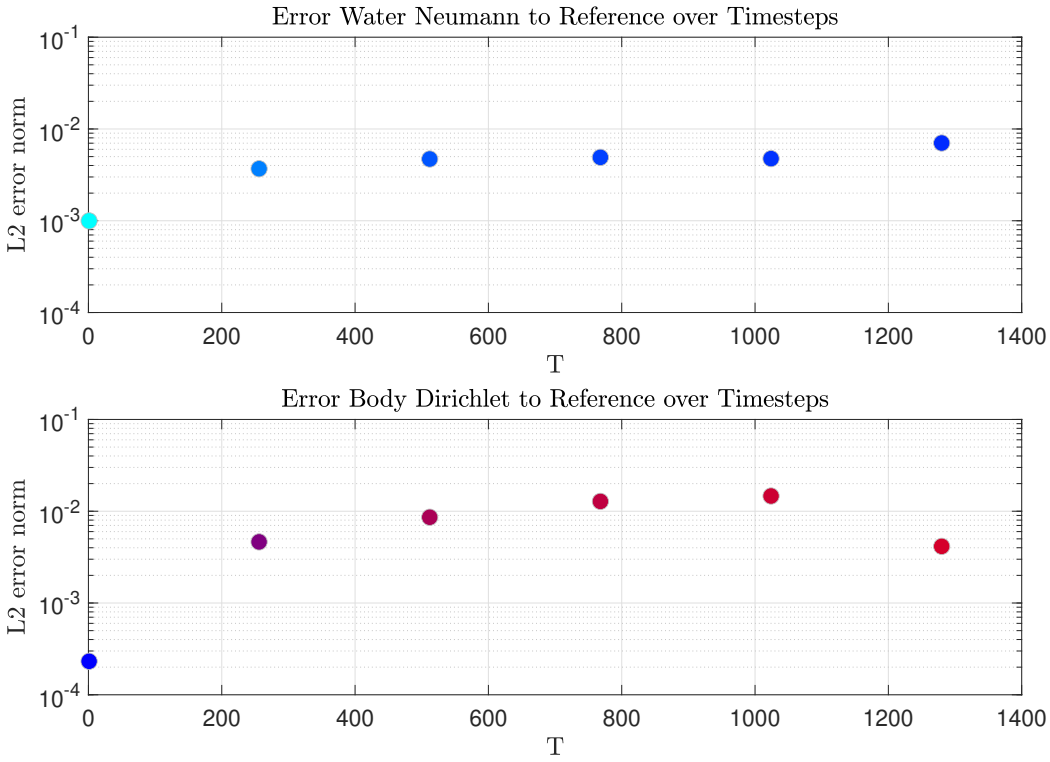

Figure 3.25: L_2-error for the normal derivative of the velocity potential at the free surface (top) and the potential at the body surface (bottom).

the body surface is on a comparably small level as the free surface quantity error, also it shows slightly more deviations between the discrete measuring points.
The step from the stationary error (t=0) to the next measure was explained by the account of the actual velocity potential as free surface boundary condition. The error decrease represents the error due to the time integration.
Conclusively, the presented results highlight the proof of research hypothesis RH5. The time stepping allowed stable computation of the dynamics accounted in cBEM and gave accurate results which are valuable in the modeling of wave-body interactions.
By proving the time integration scheme, the development steps subjected to this thesis were finalized and the testing of cBEM in the field of hydrodynamics is presented in the next chapter.

Chapter 4

Validation of cBEM for hydrodynamic applications

In the following section, the results of the validation of cBEM according to hydrodynamic problems of academic character are presented. The problems were restricted to two dimensions (assuming infinitesimal long cylinders in long crested waves), the intersection occured at element end points, and the amplitudes of the structure or body (hereafter referred as body) motions and the free surface elevation were assumed to be small which allowed the application of the linearized solver. The motivation was to demonstrate the applicability of cBEM to standard problems arising in marine hydrodynamics as well as to illustrate the accuracy and the stability of the coupled solver.

The solution was obtained by using the basis functions of interelement support for the water domain and intraelement basis functions for the body domain. By using the Z-Splines for the free surface the results were directly linked to the HOS solution as this basis functions approximated the global functions used in the spectral method, see Subsec. (2.2.2). The integration orders had been held constant for the test cases and chosen to four for the farfield of both domains, see also Tab. (4.1) that summarize the integration orders for the near and self regime evaluation as well. For the time integration, the RK4 scheme was applied including the linearized dynamic and kinematic boundary condition for the free surface. The force evaluation was performed by using second order FD scheme, Eq. (3.31), for the integration of the body potential in time.

At the boundary of the water domain, the periodic like boundary condition was applied throughout all test cases by using the Method of Farfield Extension.This test case setup differed from standard numerical wave tanks that include a wave imposing and wave energy damping boundary condition. As the solution at the free surface was influenced by incoming and outgoing waves, the computational domain had been chosen sufficiently long and the results were obtained before waves reenter the computational domain.

The main considered hydrodynamic cases represented the modification of the free surface in terms of wave radiation and diffraction due to the presence of the submerged and the surface piercing body. For the analysis of the accuracy of the solver, well-established literature had been chosen and used as guideline for the design of the test cases. The comparison of the cBEM solutions with the results from the literature is presented and discussed throughout the next paragraphs.

Table 4.1: Integration orders for free surface, body and coupled BIOs used for the validation testcases.

Free Surface		Body		Coupled	
Far W2W	4	Far B2B	4		
FarUp W2W	20	FarUp B2B	20	FarUp Coupl.	20
Adja. W2W	20	Adja. B2B	20	Adja. Coupl.	20
Self W2W	10	Self B2B	10		

Limitation of comparitive studies In the following the numerical results found with cBEM are compared with the results from the literature. The reference results from the publications were extracted with the tool *xyscan*. This was indicated as a reasonable method because the analytical solutions were not available to the specific problems. Nevertheless, it should be noted that the extraction of the values might include smaller errors so that in the consequence here presented reference values might deviate slightly from the values in the papers.

4.1 Submerged body

The submerged body was tested in terms of wave diffraction and radiation as well as in an opposing uniform flow. The theoretical solutions related to these problems in two dimensions have been investigated over a long period. The related reports and the obtained results were well suited as reference for numerical approaches as cBEM, because the various mechanisms of wave-body interaction have been analyzed and reported in a detailed manner. The test cases for the diffraction and the radiation of waves due to a submerged circular cylinder was done according to the paper of Ogilvie [133], whereas for the uniform flow test case paper of Tuck [166] and Scullen & Tuck [152] was considered.

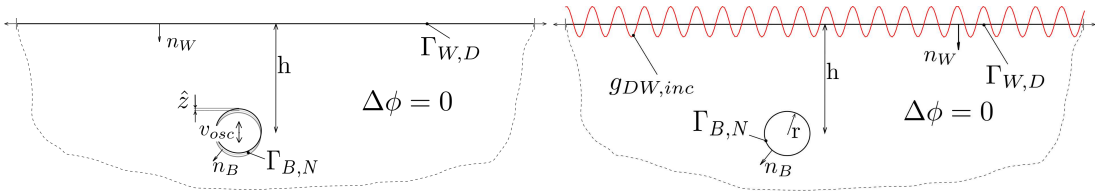

Figure 4.1: Forced oscillation and Diffraction testcase for submerged body.

4.1.1 Forced oscillations

Starting with the radiation problem of waves due to a harmonically oscillating body in small amplitudes around a fixed position, brings the papers of Ursell [168, 169] and Ogilvie [133] on the table. By using mulitpole distribution that represent the submerged body and accounting the velocity potential as a superposition of symmetric and anti-symmetric part, Ursell applied the method of infinite determinants to solve the algebraic system to find a solution for the velocity potential. Accounting a pulsating source, a solution for the radiation problem have been found. Ogilvie [133] has extended the approach of Ursell [168] and applied it to the three problems accounting a fixed, a forced and a free moving, neutrally buoyant, submerged circular cylinder. The derivation of the second order force and its evaluation in the three

test cases has been in the focus of the work. Furthermore, and most relevant for the cBEM validation, was the investigation of the first order force and its added mass and damping part at different body submergence depth to wave length and characteristic length scale to wave length ratios, expressed as $2kh$ and ka respectively. The wavenumber k, the submergence depth or the vertical distance between the bodies center and the still water level $z = 0$, $h = z_{B,c}$, and the characteristic length of the circular cylinder $a = r_B$ have been varied and the hydrodynamic coefficients were shown. At this point it might be asked, why the analytical value for the added mass and a circular cylinder section, $A_{ij} = \rho\pi r_B^2$ (see e.g. Patton, 1965) was not considered first. The investigation of Ogilvie have accounted the case of a cylinder approaching the free surface and indeed with increasing submergence the results approach the analytical values. From this perspective the presented solution in Ogilvie [133] represent a good test case for the accuracy of cBEM in the narrow submergence regime.

Added mass

The concept of added mass in hydrodynamics refer to a virtual mass equivalent to the portion of water that is displaced due to the motion of the body, see Ursell [167], Weinblum [183] and Newman [129]. It is the component of the hydrodynamic force that is in phase with the body's acceleration. In the differential equation describing the body motion, this virtual mass is added to the body mass. The notation A_{ij} describe the added mass caused by the mode i and reacting in direction j. The added mass Matrix **A** include all uncoupled and coupled contributions and simplifies by considering e.g. the symmetry of the body or the coincidence of the centers of rotation and gravity.

Damping coefficient

The hydrodynamic force part in line with the velocity is referred as damping. For an applied force to a body in water which is initially in its equilibrium position, the resulting body motion is reduced with time according to the damping coefficient of the dynamical system. The damping is highest if the velocity is maximal and vanish in the position of maximal amplitudes as the body velocity reach zero. Correspondingly to the added mass, the damping coefficients D_{ij} are defined and form the damping matrix **D**.

The contributions for the hydrodynamic coefficients and considerations for simplifications and vanishing of certain coupling components are given e.g. in Mei et al. [115] for two- and three-dimensional problems.

Outline of the problem The computational setup was chosen with respect to the parameter range of $2kh$ and ka used in Ogilvie [133]. For the derivation of the wavenumber, the oscillation frequency was used under the assumption that a wave of angular frequency $\omega = \omega_{osc}$ induce the same motion to the body. In Tab. (4.2) the relevant parameters for a radius of $a = r_B = 1$ m are presented and it's shown that the submergence to wave length ratio was in the range of $2kh \in [2, 10]$ and the radius to wave length was $ka \in [0.2, 0.4, 0.5, 1.0, 2.0]$. The computational parameters are given in Tab. (4.3). As no

Table 4.2: Parameter space accounted for the test case of a fixed body forced to harmonically oscillates with angular frequency ω_{osc} submerged at depth h.

ka	$\omega_{osc} = \sqrt{gk}$ [rad/s]	$\lvert h\rvert_{2kh=2}$ [m]	$\lvert h\rvert_{2kh=4}$	$\lvert h\rvert_{2kh=6}$	$\lvert h\rvert_{2kh=8}$	$\lvert h\rvert_{2kh=10}$
0.2	1.401	5	10	15	20	25
0.4	1.981	2.5	5	7.5	10	12.5
0.5	2.215	2	4	6	8	10
1.0	3.132	1	2	3	4	5
2.0	4.429	(0.5)	1	1.5	2.0	2.5

hydrostatic components were accounted (body fixed at its center of gravity), the equation of motion for the forced oscillation was given by

$$A_{ij}\frac{d^2z}{dt^2} + D_{ij}\frac{dz}{dt} = F_{ij} \tag{4.1}$$

Table 4.3: Parameters of the free surface, body and computations in the submerged circular cylinder radiation test case of .

Free Surface		Body		Forc. Oscill.		Comp. Param.		Comp. Param. Time	
L_W	64m	r	1m	$\hat{z}$	0.02	N_W	128	dt	10^{-2}s
ρ_W	1000kg/m^3	r/h	var.	Mode	z	N_B	16	t_{sim}	20s
D	10^5m	(x_c, z_c)	(32,h)	ω_{osc}	var.	N_{Im}	10	RK order	4

wherein $z = \hat{z}\cos(\omega_{osc}t)$ is the displacement of the circular cylinder with amplitude $\hat{z}$ and F_{ij} is the instationary part of the hydrodynamic force.
For the evaluation of the added mass and the damping coefficient, the phase angle ϵ between the force and the oscillation velocity was evaluated in terms of

$$\epsilon = \frac{nTdt}{T_{osc}}2\pi \quad , \tag{4.2}$$

with the number of time steps representing the phase difference nT, the oscillation period T_{osc}. From that the contributions for added mass and damping are found by

$$A_{zz} = \sin(\epsilon)\frac{F_{zz}}{\omega_{osc}^2\hat{z}} \tag{4.3}$$

$$D_{zz} = \cos(\epsilon)\frac{F_{zz}}{\omega_{osc}\hat{z}} \tag{4.4}$$

as for the case of hydrodynamic force and velocity being in phase, $\epsilon = 0, \pi, 2\pi$, the added mass vanished and only the damping component remained. Correspondingly, for a phase shift of $\epsilon = \pi/2, 3\pi/2$ the damping part vanished and the hydrodynamic force due to the instationary pressure contribution was only added mass. In frequency domain, the added mass is the real part of the hydrodynamic force whereas the damping component is the imaginary part.

Results and discussion The results of the time domain simulation for distinct submergence to wave length ratios and the corresponding absolute values of Ogilvie results [133] for the added mass are shown in Fig. (4.2) and for the damping coefficient in Fig. (4.3). The results obtained from the time domain simulation with cBEM fitted well to the absolute values of the theoretical results from Ogilvie, shown by the rhombuses and connected by the dashed lines. The reduction of the added mass by approaching to the free surface and the increase of the effect with increasing body length scale are well reproduced by the numerical results. In contrast to the approach of Ogilvie the free surface was explicitly discretized which gave a more restrictive limit for approaching smaller $2kh$ values as the body was assumed to be submerged.
The decrease of the added mass from the analytical value ρA was due to the free surface that affected the pressure distribution on the body surface, when the submergence depth was considerably small. Accounting the streamlines around the body and of the waves propagating symmetrically from the position of the body, this was explained as the streamlines were modified close to the free surface due to the decrease of the amount of fluid above the body. Due to the increase of the surface section, on that the pressure change occurred, the decrease of the added mass became more significant for bodies of larger radius. The damping part of the hydrodynamic force acting on the cylinder is shown in Fig. (4.4). The numerical results from cBEM vary from the absolute results of Ogilvie especially at vanishing damping coefficients that occur for larger body submergence. Here, the decreasing capability of the free surface to damp the body motion is reflected and only the added mass cause the instationary force on the cylinder in the case of forced oscillation.The deviations of the numerical cBEM results are an indicator that the temporal discretization was to coarse in the simulations so that the phase difference of the harmonic velocity oscillations and the hydrodynamic force was not refined appropriately. Nevertheless, the results are satisfactory when damping became more dominant. In this case, the inertia of the body motion and

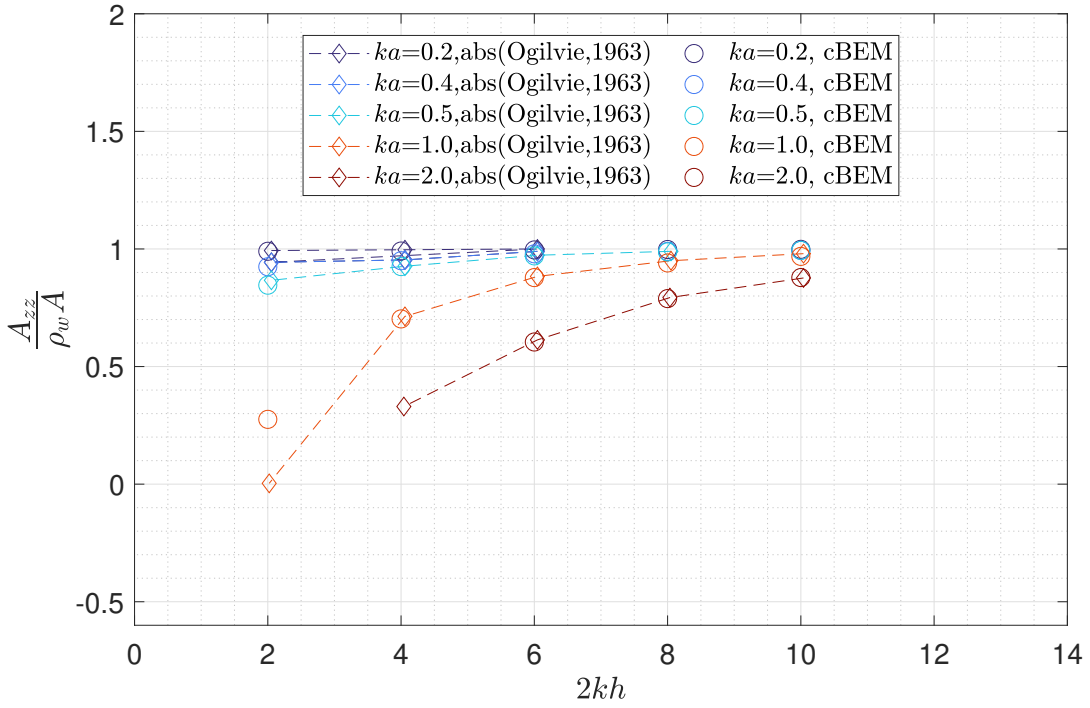

Figure 4.2: Added mass for forced oscillation

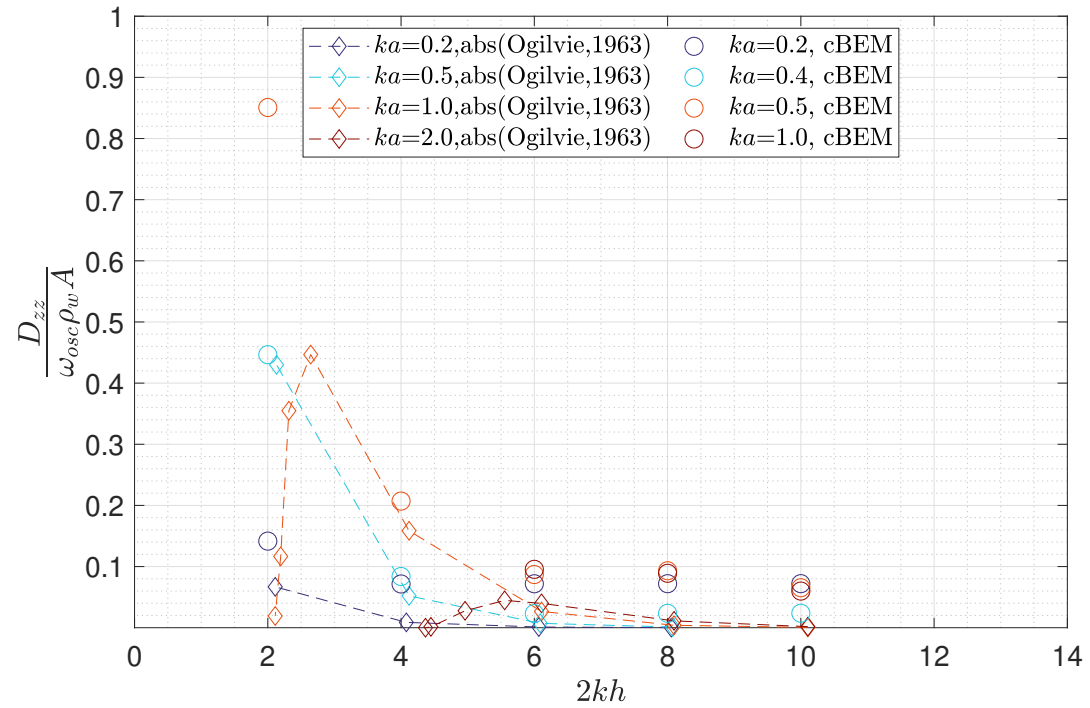

Figure 4.3: Damping coefficient for forced oscillation

the gravitational field, determining the dynamic free surface boundary condition, came in conflict. For certain submergence depth and body dimension the gravitational force dominated which resulted in an increase of the motion damping. These combinations of wave and body parameters indicated a strong interaction between the body and the free surface. For the design of wave making devices or WECs these

parameter combinations might be accounted favorably.
Summarizing the findings of this validation case, the time domain simulation with periodic like boundary conditions on the water domain was successfully applied for this test case. The procedure for evaluating the hydrodynamic coefficients was introduced and the cBEM results for the added mass were well comparable to Ogilvie's theoretical results. For the damping coefficient, the results were shown to be sensitive to the chosen discretization, which was indicated by the deviations from the theoretical values in the range of vanishing damping. Due to the time domain simulations (in frequency domain it's simply the differentiation of the real and imaginary part), the evaluation of the phase difference between the force and motion signal, Eq. (4.2), was crucial to find the hydrodynamic coefficients, Eq.(4.3). By these equations, it became obvious that the temporal discretization especially for small damping values ($\epsilon \rightarrow n\pi/2 \Rightarrow \cos(\epsilon) \rightarrow 0$) was relevant as the gradient of the cos functions was high near $n\pi/2$ and thus sensitive to the phase angle ϵ. In contrast, the added mass was evaluted by the sin function and the small gradient around $n\pi/2$ made it less sensitive to the temporal discretization. It followed, that the damping parameter was well suited as indicator for a sufficient time discretization.

4.1.2 Diffraction

Dean [44] has shown firstly that a submerged cylinder cause no wave reflection for the case of an incident wave propagating upon the cylinder. Instead, it has been shown that the transmitted wave has a phase difference to the incident wave. He has used an infinite set of linear equations from that a solution for the unknown free surface velocity potential has been found. Ursell [168] has obtained similar results by applying the multipole approach and also Ogilvie has shown the pure transmission characteristic of the waves in the presence of a submerged circular cylinder in his first considered case in Ogilvie [133].

Outline of the problem Ogilvie's results [133] in terms of wave diffraction were considered as second test case for the validation of the cBEM. Again, the decrease of the submergence depth was accounted as the test case parameter in addition with the ka ratio. The parameter space of the derived test case was chosen in terms of the submergence height as already done in the forced oscillation test case, see Tab. (4.2) . In order to realize the analysis of the diffraction problem in the cBEM environment, regular

Table 4.4: In variation of the number of waves to realize the ka parameter range in the wave diffraction test case. The depth of the body was chosen according to Tab.(4.2)

ka	0.2	0.4	0.5	1.0	2.0
nWaves/L_W	2	4	5	10	20

Table 4.5: Parameters of free surface, body and computations in test case diffraction due to submerged circular cylinder.

Free Surface		Body		Diffraction		Comp. Param.		Comp. Param. Time	
L_W	63m	r	1m	k	var.	N_W	126 (252)	dt	10^{-2}s
ρ_W	1000kg/m^3	r/h	var.	ε	0.015	N_B	16 (24)	t_{sim}	20s
D	10^5m	(x_c, z_c)	(32.5, h)			N_{Im}	10	RK order	4

wave trains of various wave length according to Tab .(4.4) were defined as initial boundary condition for the velocity potential of the free surface. The initial body Neumann boundary condition was defined according to the analytic linearized free surface potential, see Sec. (3.2.4) and Eq. (3.25), which implied that the body initially did not affect the wave dynamics. Within the first number of time steps, the body Neumann boundary condition was progressively decreased linearly to zero. After this initial ramp that the fixed body affected fully the free surface waves. The computational parameters that have been used for the test case are summarized in Tab.(4.5).

The investigated variables chosen for the comparison with the results from Ogilvie, were the maximum of the first order hydrodynamic force on the fixed circular cylinder and the phase shift between the force and the incident wave. For the evaluation of the phase lag, the procedure described in the previous subsection had been applied, see Eqs. (4.2) and (4.3), and only the instationary part of the pressure integrated over the cylinder was accounted as hydrodynamic force.

Results and discussion In Fig.. (4.4), the phase difference between incident wave and force are shown

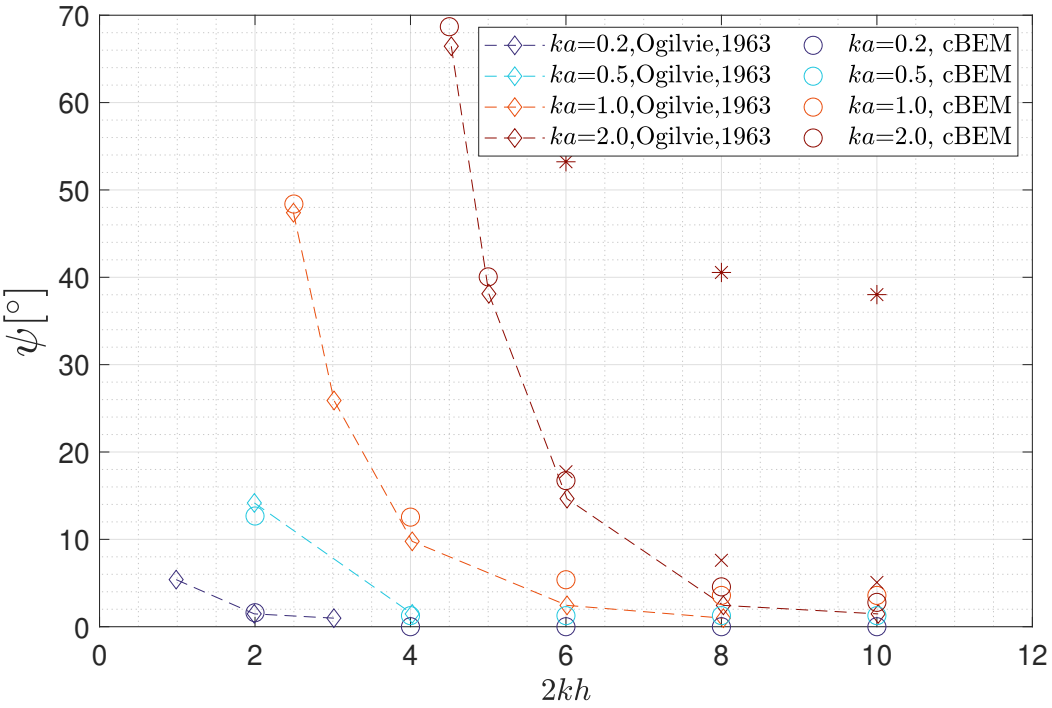

Figure 4.4: Phase shift between incident wave and maximum of first order hydrodynamic force according to cBEM and Ogilvie [133].

with respect to the submergence depth. The numerical and theoretical results match well. The effect of body depth and radius to the phase shift is demonstrated clearly and indicate the influence of the body to the wave system. Coming closer to the still water level, the influence of the body was strong, the phase speed of the wave decreased, and consequently the transmitted wave had a larger phase lag behind the cylinder, see Ogilvie [133]. Ogilvie has compared this effect with a wave approaching in shallow water. This influence of the body to the wave system above is also indicated by the amplitude of the hydrodynamic force, presented in Fig. (4.5). For the larger body dimension $ka = 2$, the force reach a maximum and decay with high gradient. The same occurs for $ka = 1$ as shown in Ogilvie [133]. This was again caused by the influence of the free surface on the body and was explained as the small fluid layer on top of the body cause significant deceleration of the fluid on the upstream side from the cylinder center axis and an acceleration to the other side. The previously dominant vertical force due to the free surface dynamics was therefor compensated by increasing horizontal forces in this limiting case.
The cBEM results and the corresponding results from Olgilvie were well comparable over all body to wave length ratios and submergence depths. The increase of the hydrodynamic force on the cylinder surface due to the wave above was well approximated. Also the decay of the force in the case of large body to wave dimension near the free surface was represented accurately.
A convergence study was made for the case of $ka = 2$, shown in Tab. (4.6) and indicated that especially for the phase difference $\psi - \psi_{ref}$, the refinement in time and space was necessary to find the appropriate values. With respect to the amplitude of the hydrodynamic force the refinement became more important at smaller submergence depth which was due to the higher influence of the free surface do-

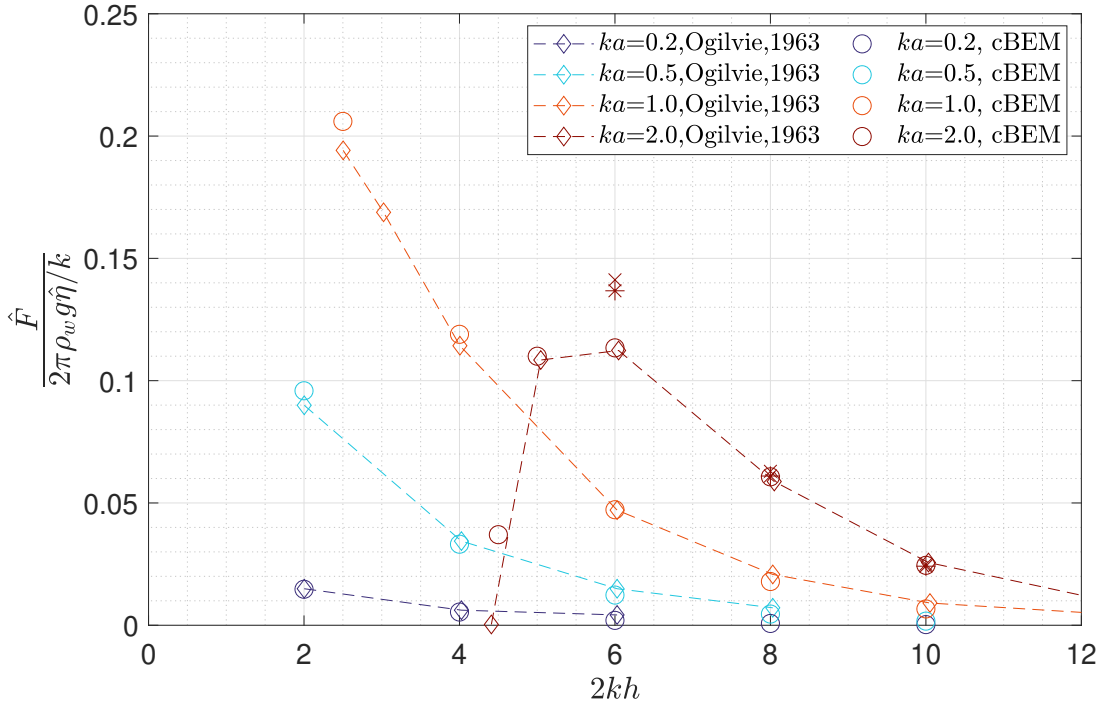

Figure 4.5: cBEM computational results for maximum hydrodynamic force and corresponding results from Ogilvie [133].

main. The higher temporal and spatial resolution led to a more accurate result and allowed an evaluation closer to the free surface shown by the results in the range $4 < 2kh < 6$ in Fig. (4.5). To put the differ-

Table 4.6: For $ka = 2$ the effect of time and space resolution to the values of force amplitude and phase difference are shown and compared to the reference values obtained from the diagrams given in Ogilvie [133].

	dxW	dt	$\psi - \psi_{ref}$	$\frac{\hat{F}-\hat{F}_{ref}}{2\pi\rho_W g\hat{\eta}/k}$
2kh=6	0.5	1E-2	53.22-14.66	0.14-0.11
	0.25	1E-2	17.74-14.66	0.14-0.11
	0.25	1E-3	16.73-14.66	0.11-0.11
2kh=8	0.5	1E-2	40.52 - 2.44	0.061-0.059
	0.25	1E-2	7.60 - 2.44	0.063-0.059
	0.25	1E-3	4.56 - 2.44	0.061-0.059

ences between the computational and reference values of the phase difference $d\psi = \psi - \psi_{ref}$, given in Tab. (4.6), in the context of the used approach, one find that e.g. the difference in phase at $2kh = 8$, $d\psi|_{2kh=8}$, was related to a difference in time of $\approx 8.5 \times 10^{-3}$ s (as $d\psi|_{nT=1} = \frac{2\pi nTdt}{T}\frac{180}{\pi} = 0.254°$ and $d\psi|_{2kh=8}/d\psi|_{nT=1} \approx 8.5$). This small time range compared to the much larger period of the incident wave of $T = 1.419$ s, indicated a reasonable accuracy for this case.

Notes on further findings in Ogilvie [133] Ogilvie's results have indicated other phenomena that occur for the considered hydrodynamic problems and in the regime of small submergence depth. One is the sign change of the added mass for specific ka values and for small submergence depth. In these cases, the mass of the cylinder reduces due to the added mass and the force on the body decrease so that moving the body in the fluid becomes easier. Another one is related to the investigation of the radiation problem in terms of circular motion. Here, the results of Ogilvie have indicated that for counterclockwise

rotation, the waves propagate only to the left side from the vertical cylinder axis and vice versa for the clockwise rotation. This has been explained by accounting for the antisymmetric and symmetric surface elevation due to the horizontal and vertical oscillation respectively. The combined circular motion has resulted in a phase lag of the generated waves that has caused a destructive interference of the radiated waves to one side of the cylinder. On the corresponding other side, the constructively interfered wave components have radiated away from the cylinder.

4.1.3 Uniform flow

In addition to the radiation and diffraction problems, the uniform flow around a fixed submerged circular cylinder was investigated. Early contributions for the analysis of the problem in terms of wave resistance and theoretical solutions has been made e.g. by Lamb [102] and Havelock [77, 78, 79]. Both authors have applied the method of images in that the body has been represented by a suited distribution of source and dipols. Tuck [166] has considered higher-order terms for the evaluation of wave resistance and wave lift. Scullen & Tuck [152] have taken further nonlinear mechanism into account and presented the ratios of wave and oscillation amplitudes of Stokes waves and nonlinear surface elevations of the free surface past the submerged cylinder for different Froude numbers.

Outline of the problem In the following analysis, the surface elevation of the linear problem for different Froude numbers was considered and the cBEM results were compared to the linear solution of an internal method for the evaluation of drag and lift around submerged profiles validated by the method of Scullen & Tuck [152].
To consider the uniform flow, the stream terms were added to the linear dynamic and kinematic free surface boundary condition, Eq. (2.91) yielding

$$\frac{\partial \phi_s}{\partial t} = -g\eta - \tau u \frac{\partial \phi_s}{\partial x} \tag{4.5}$$

$$\frac{\partial \eta}{\partial t} = \frac{\partial \phi_s}{\partial z} - \tau u \frac{\partial \eta}{\partial x} \tag{4.6}$$

with the current velocity $u = (u, v)$ and the spatial derivatives $\frac{\partial}{\partial x}$. For the derivatives, a finite difference scheme of fourth order with an up- and down-wind stencil at the domain boundaries and the central rule in the rest of the domain was applied to the wave variables .
The uniform stream was achieved over an initial gradual increase of the velocity normal to the body surface and accounted in the Neumann Boundary condition

$$g_{N,B} =< u, n_B > \ . \tag{4.7}$$

The ramp was defined as an S-Curved blend-in function that follows the modified tangens hyperbolicus function

$$\tau = (\tanh\left(t/dt - nT_\tau\right)/s + 1)/2 \tag{4.8}$$

with the actual time step t/dt and the number of time steps nT_τ at the center of the ramp. The factor s was used for scaling the tanh function. The number of time steps was chosen here to $nT_\tau = 100$ and the scaling factor to $s = 25$. The function Eq. (4.8) asymptotically reach one for time steps larger than $2nT_\tau$ and was therefore used over the whole simulation time in contrast to the linear initial ramp used for the diffraction problem, Subsec. (4.1.2) that was applied to Eq.(4.5) only for the time of the ramp. For the test case the Froude number $Fr = \frac{u}{\sqrt{gh}}$ was varied yielding to different current velocities u. The parameters for the test case and the computations are given in Tabs. (4.8) and (4.7).

Results and discussion The cBEM results in terms of the surface elevation in the neighborhood of the submerged cylinder are presented in Fig.(4.6)- Fig.(4.8) for the three considered Froude numbers. The space domain results for Froude number Fr=0.4, Fig. (4.6) show deviations to the reference. Nevertheless, the amplitudes of the surface waves are similar and also the wave length is In Figs. (4.7) and (4.8) the surface elevation at four distinct time steps are shown. By presenting the earlier stage of the simulation and the steady state solution in the two top and bottom panels respectively, the transition to the steady state solution is demonstrated. The results of cBEM are well comparable to the reference.

Table 4.7: Parameters of free surface, body and computations in test case uniform flow around a submerged circular cylinder.

Free Surface		Body		Comp. Par.		Comp. P. Time	
L_W	256 m	r	1m	N_W	512	dt	$0.5 \cdot 10^{-2}$s
ρ_W	1000 kg m^{-3}	r/h	0.2	N_B	24	t_{sim}	var
D	10^5m	(x_c, z_c)	($L_W/2$, -5)	N_{Im}	10	RK ord.	4

Table 4.8: Froude number, corresponding stream velocity u and varied simulation time for the uniform flow test case.

Fr	$u = Fr\sqrt{gh}$ [m s^{-1}]	t_{sim} [s]
0.8	5.60	75
1.0	7.00	50
1.2	8.40	

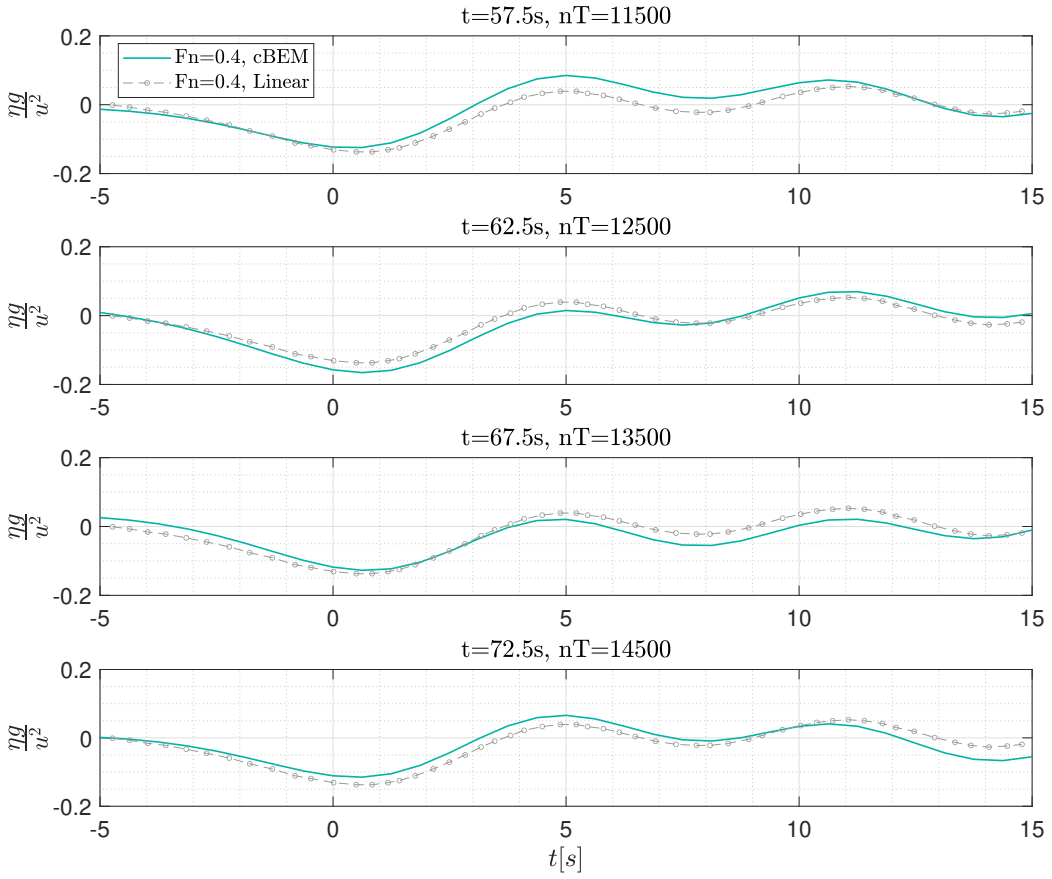

Figure 4.6: Normalized surface elevation at distinct time steps for Fr=0.4. Linear solution is shown by grey circels and cBEM results in green solid line. The circular cylinder is horizontally located at $x = 0$.

4.2 Free surface piercing body

For the validation of the surface piercing body, the radiation of waves due to forced body oscillation were analyzed and the results compared with literature are presented below.

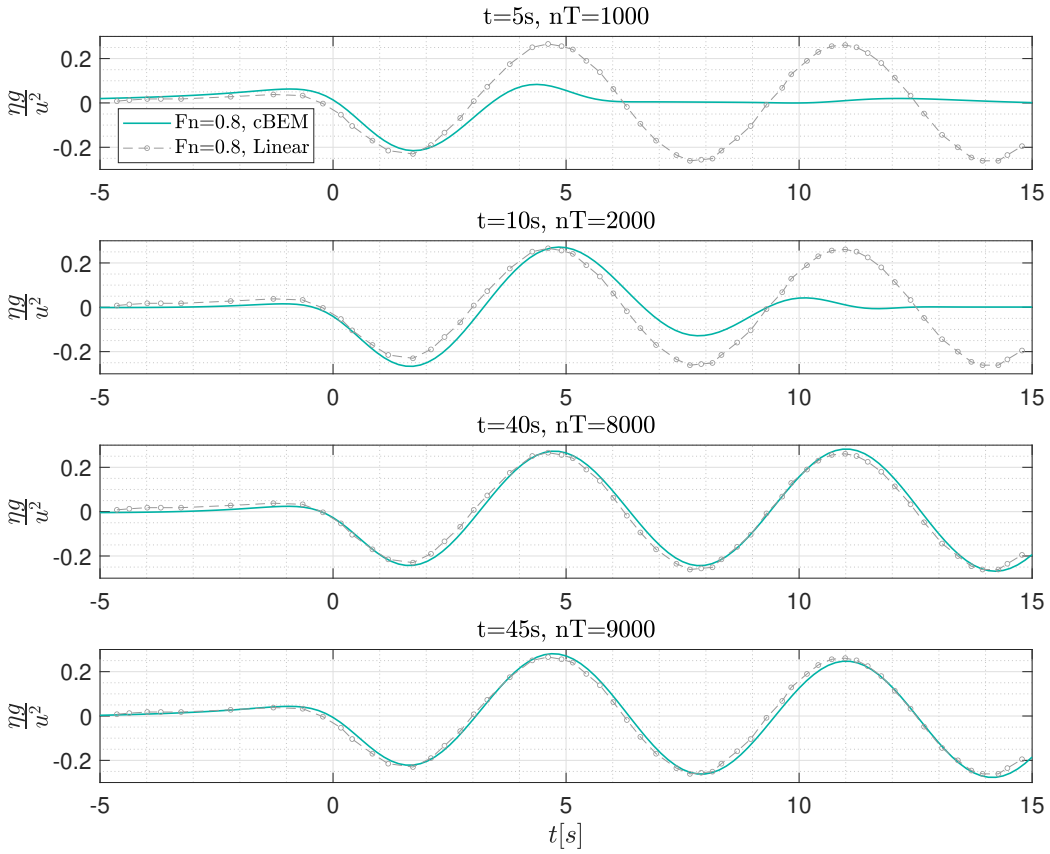

Figure 4.7: Normalized surface elevation at distinct time steps for Fr=0.8.

The radiation problem of bodies on the free surface in two dimension have been solved theoretically e.g. by Ursell [167], see Subsec. (1.2). By using polynomial sets, Ursell have found solutions for the BVP of a forced harmonic oscillating circular cylinder for different oscillation frequencies. The added mass coeffficients as well as amplitude ratios of radiated waves and oscillation have been presented.
Vugts [177] have conducted experiments with cylinders of various cross-section and the eigen and coupled modes of sway, heave and roll motion. The results for amplitude ratios, added mass and damping coefficients have been compared with computations based on linearized equations for that Ursell's approach have been applied to arbitrary shaped cylinders, see De Jong [43]. Furthermore, the wave diffraction have been investigated experimentally. The horizontal and vertical wave excitation forces, the wave excitation moment and the phase angle between incident wave and hydrodynamic forces have been compared with the approaches of Newman [124] and Motora [117]. Motora have corrected the Froude Krylov force to obtain an approximation for the excitation force of the diffracted waves whereas Newman extended the farfield approximation, introduced by Haskind [76] and based on the damping coefficient, to two dimensions.

Outline of the problem For the comparison with the cBEM results, the forced oscillation test case in heave and sway modes were conducted with a rectangular cylinder with a breadth to draught ratio of $B/T_B = 2$. The oscillation frequency was varied so that a non dimensional frequency range comparable to the one used in the experiments of Vugts was reproduced, see Tab. (4.9). The analysis of the results was done in terms of the amplitude ratio of the radiated wave and the oscillation amplitude, the added mass and the damping coefficient.
The amplitudes of the radiated waves were found by considering a stationary surface elevation in a reasonable distance from the body ($\approx$10 m to 20 m). The hydrodynamic coefficients for added mass and

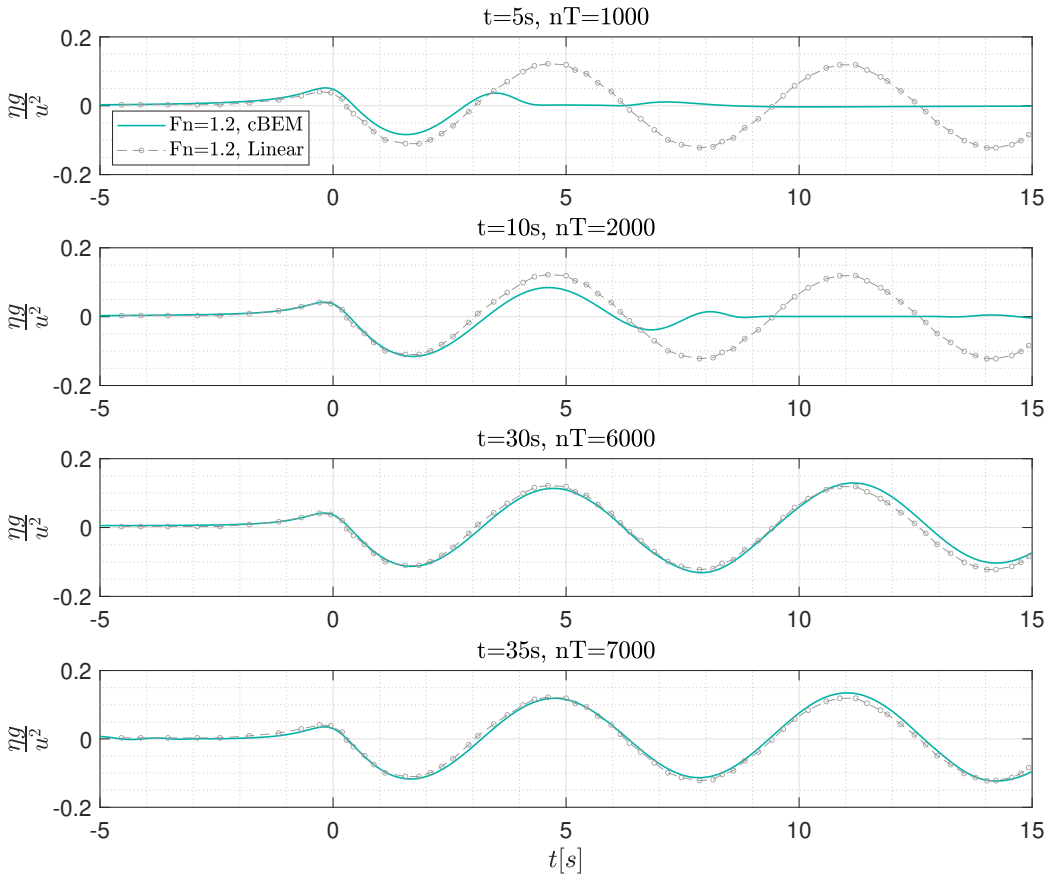

Figure 4.8: Normalized surface elevation at distinct time steps for Fr=1.2.

Table 4.9: Parameter space of forced oscillation test case with free surface piercing rectangular cylinder.

$\omega_{nd} = \omega\sqrt{B/2g}$	0.5	0.75	1.0	1.25	1.75
ω [rad/s]	1.566	2.349	3.132	3.915	4.698

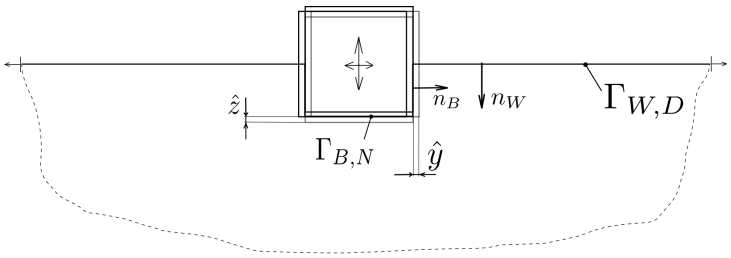

damping were evaluated as in the case of the submerged body, Subsec. (4.1.1) and the phase angle ϵ between the oscillatory velocity and the hydrodynamic force was applied according to Eq. (4.3) to find the coefficients for the radiation problem. The simulations had been performed with the computational parameters shown in Tab. (4.10).

Results and discussion The comparison of the cBEM results based on time domain computations and the experimental and computational results presented in Vugts are shown in Figs. (4.9)-(4.11) for the heave motion. The amplitude ratio for the heave mode, given in Fig. (4.9), shows a good match to the experimental values obtained from Vugts. Compared to the computational results, the amplitude

Table 4.10: Parameters of free surface, body and computations in test case of free surface piercing rectangular cylinder forced to harmonically oscillate.

Free Surface		Body		Forced Oscill.		Comp. Param.		Comp. Param. Time	
L_W	128m	a=B/2	1m	$\hat{y}, \hat{z}$	0.02m	N_W	256	dt	10^{-2}s
ρ_W	1000kg/m^3	T	1m	Mode	y,z	N_B	16	t_{sim}	20s
D	10^5m	(x_c, z_c)	(64, 0)	ω_{osc}	var.	N_{Im}	10	RK order	4

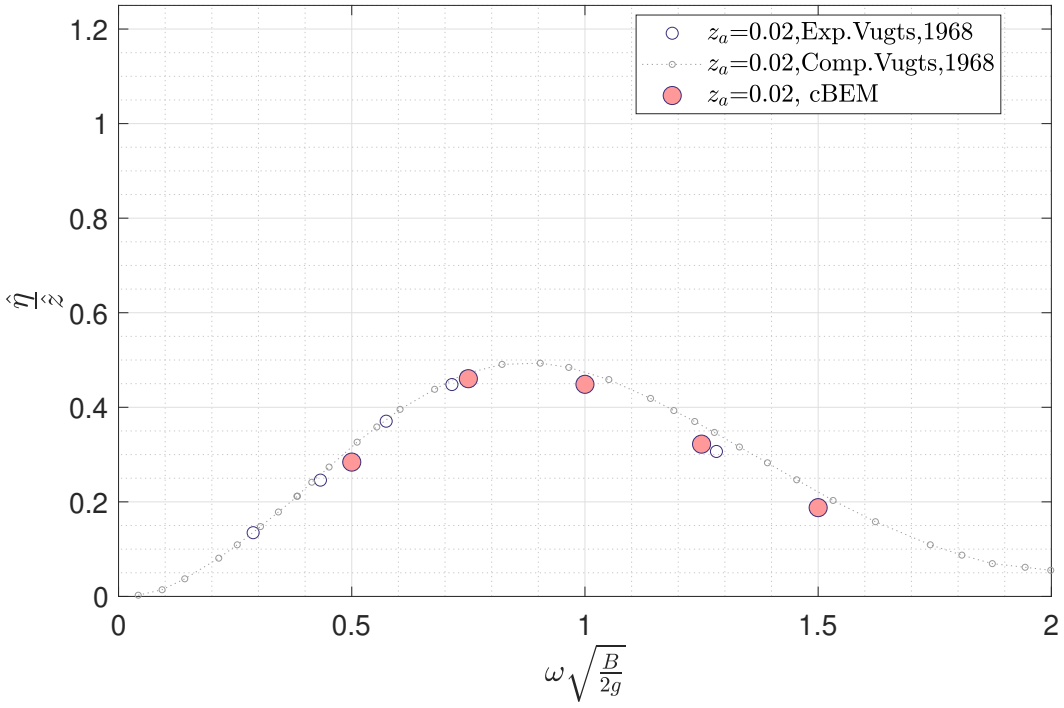

Figure 4.9: Ratios of the amplitudes of surface elevation and oscillatory motion for heave motion over normalized angular frequency. Numerical results from cBEM (red filled circs) and computational (light gray circs and dotted line) as well as experimental results (small cirs) from Vugts [177] for rectangular cylinder on the free surface with breadth to draught ratio of $B/T_B = 2$ are shown.

ratios are slightly smaller at the higher frequencies. In the computations for the amplitude ratios of the rectangular geometry, Vugts have accounted two parametrizations for the geometry. One was related to the best section fit and the other to a Lewis form, here the latter was considered as the best fit was more specific to the conducted experiments. The related computational results, as well have shown small deviations at higher frequencies and thus indicated a sensitive behavior to the geometry parametrization in this frequency range. Keeping this variances in mind, the mentioned differences between the cBEM results and the results of Vugts could considered as explainable and were still within an acceptable accuracy range. In Fig. (4.10), the cBEM results for the added mass are again well comparable to the experimental results but fit especially at higher oscillation frequencies better to the computations given in Vugts.

A small departure from the results of Vugts at higher oscillation frequencies can be identified for the damping shown in Fig. (4.11). This was, as discussed in Subsec. (4.1.1), due to the sensitivity at small phase angles between the signal of the hydrodynamic force and the oscillation velocity. The effect of an increase of the spatial resolution about factor two is demonstrated here by comparing the cBEM results for dxW=0.5 m (blue crosses) and dxW=0.25 m (red filled blue circles). The differences became more significant as the angular oscillation frequency increased.

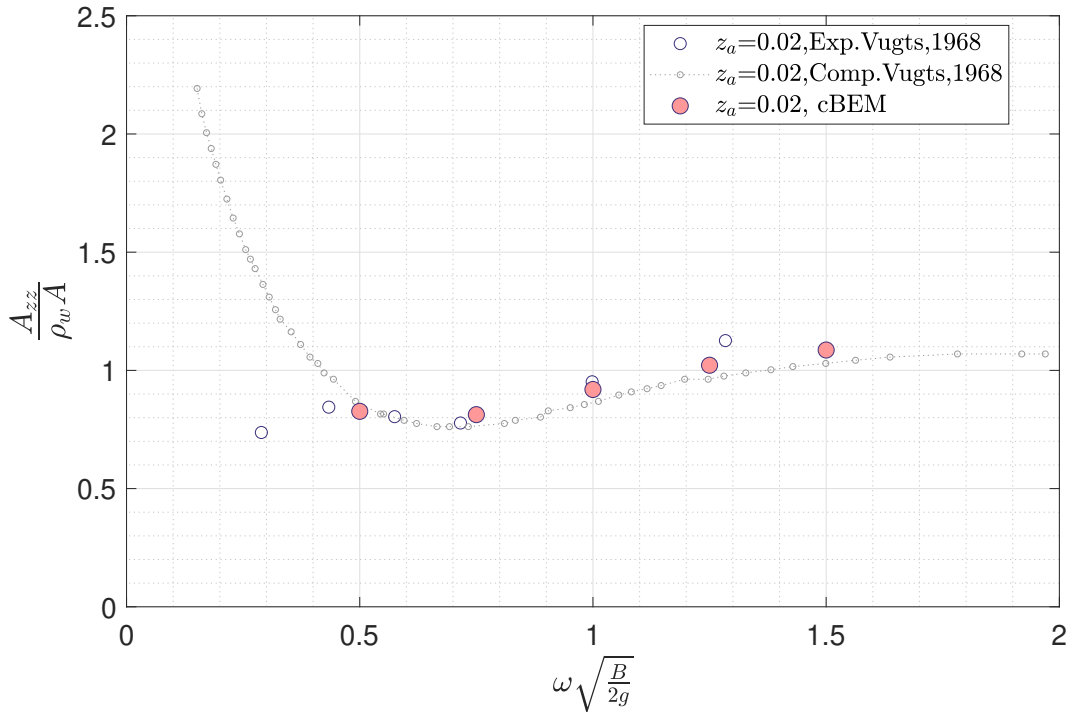

Figure 4.10: The added mass in heave mode is given over a normalized frequency range for the rectangular cylinder with $B/T_B = 2$. The experimental and computational results of Vugts [177] are shown in comparison with the numerical cBEM results.

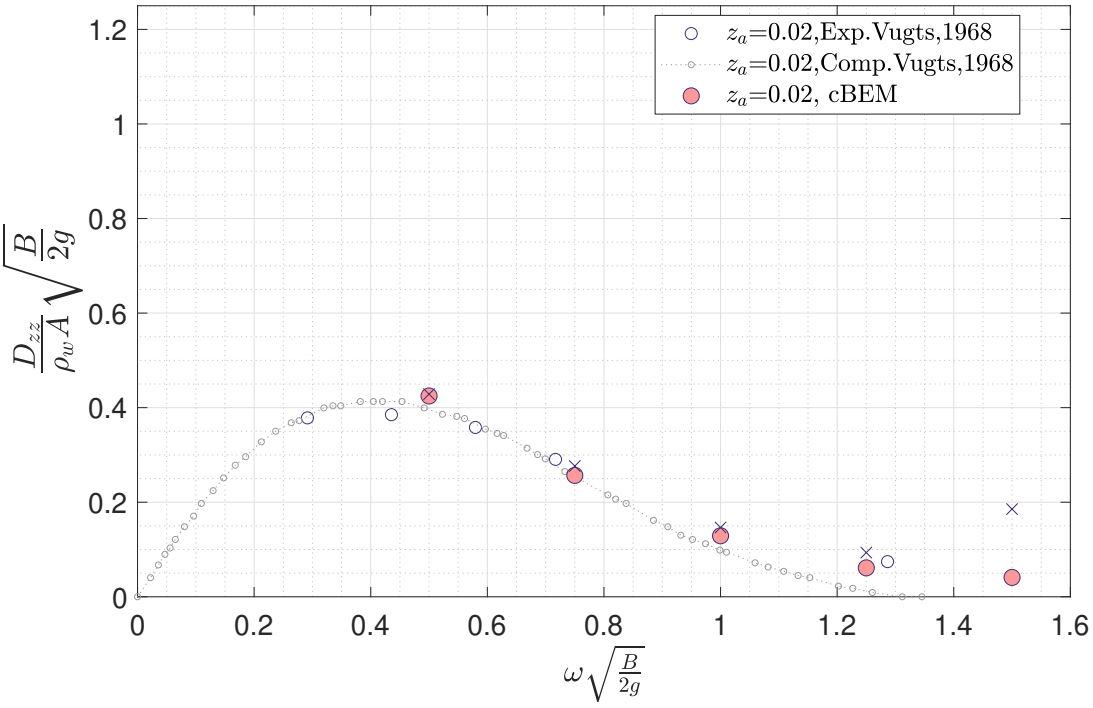

Figure 4.11: The variation of the damping coefficient with normalized angular frequency is presented for the heave motion and according to results from cBEM and results given in Vugts [177]. The cylinder is of rectangular cross-section and the breadth to draught ratio is $B/T_B = 2$.

As for the heave motion, the results in sway mode had been compared with the literature reference. The

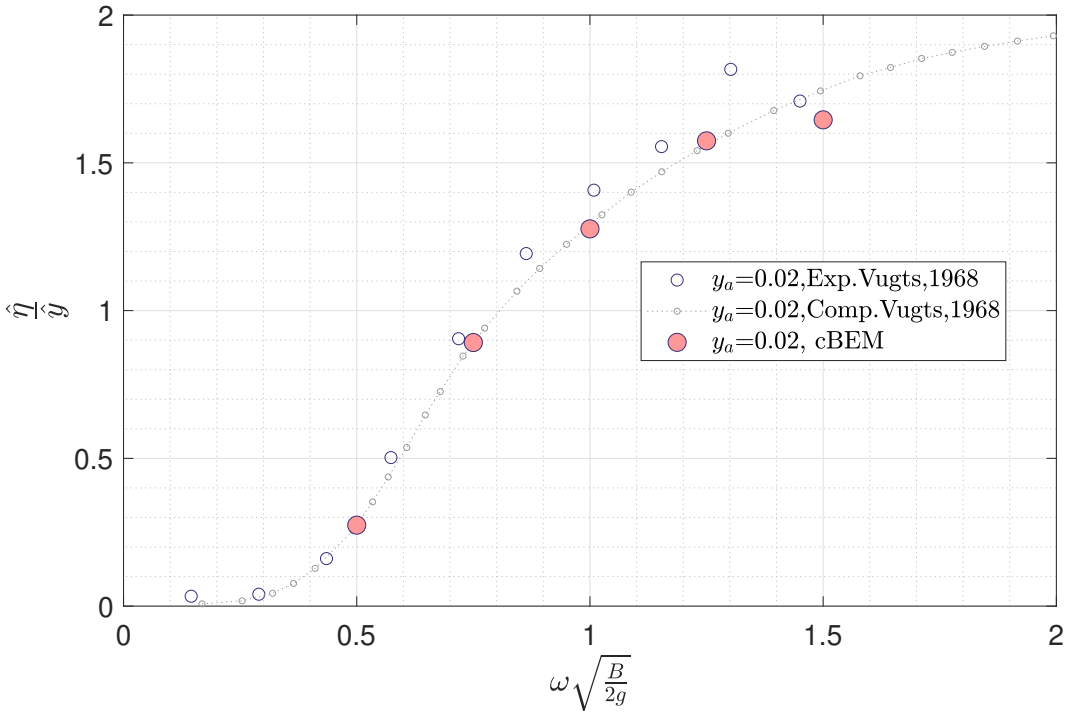

Figure 4.12: Amplitude ratios of surface elevation and oscillatory motion for sway motion over normalized angular frequency. Numerical results from cBEM and computational as well as experimental results from Vugts [177] are shown for the rectangular cylinder on the free surface with $B/T_B = 2$.

increase of the amplitude ratio with oscillation frequency, presented in Fig. (4.12), shows a good match to the experimental and computational results that have been given by Vugts [177]. The deviation at the highest frequency might be related to the sensitivity of the computational results with respect to the accounted geometry in Vugts [177] and discussed above for the amplitude ratio in heave.
The cBEM results for the added mass and the damping coefficient, given in Figs. (4.14) and (4.14) respectively, indicate a good agreement to the computational results. The experimental results deviate from that, especially for the damping coefficient the experiments show an offset to the computations. Vugts has explained the devitaions of experimental to theoretical results by the effect of viscosity in terms of skin friction and eddy formation along the rectangular geometry in the experiments and has shown that for higher B/T_B ratios the deviations decrease as the viscous effects are less dominant for the damping at smaller submergence depth [177].
In summary, the numerical results of cBEM were well comparable with the results of Vugts [177] for the considered modes and frequency range. The hydrodynamic coefficients and the amplitude ratios were captured with good accuracy by the introduced evaluation methods, see Eq. (4.3). Thereby, a consistent procedure for testing the linear time domain solver with frequency domain results was presented. Limitations for the comparison of these approaches were indicated at higher frequencies for the amplitude ratios and the damping coefficients. The location of the gauges and the influence of the spatial and temporal discretization played a role. Considering these aspects, the comparison of time and frequency domain result might be used as indicators for sufficient grid resolution in future investigations. These results confirm that cBEM is well suited for analyzing the interaction of waves with a surface piercing body forced to small amplitude motions. Based on this, future steps can address the analysis of forces in rolling and coupled modes, and the consideration of DoF's in body motion.

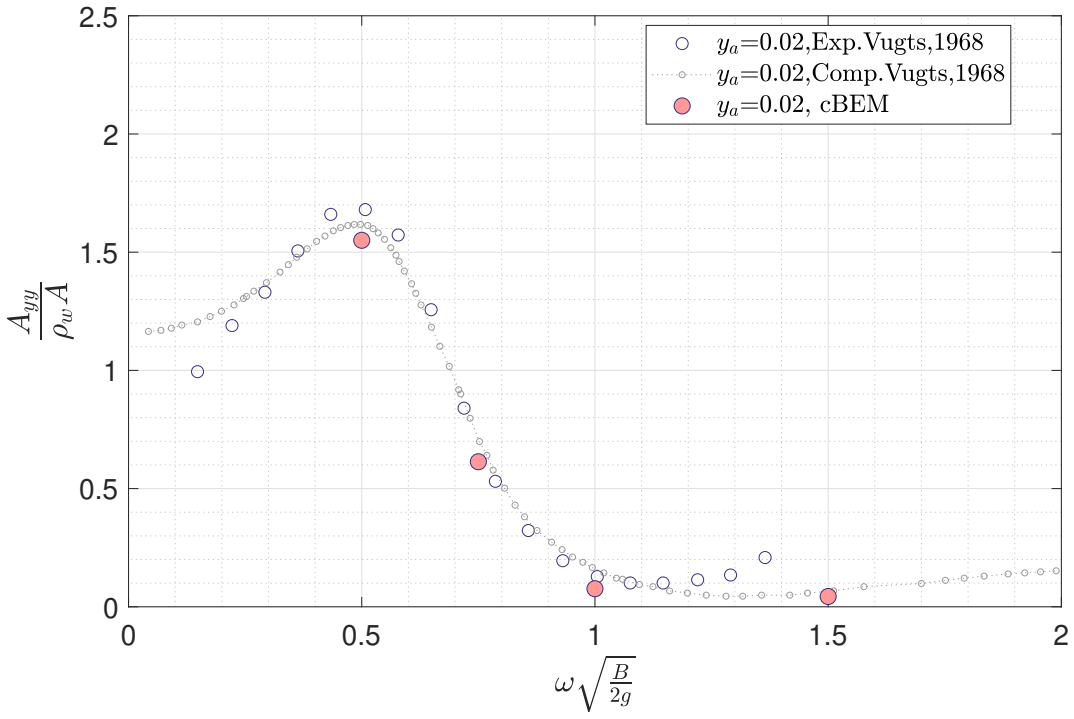

Figure 4.13: The added mass in Sway mode is given over a normalized frequency range for the rectangular cylinder with $B/T_B = 2$. The experimental and computational results of Vugts, [177] are shown in comparison with the numerical cBEM results.

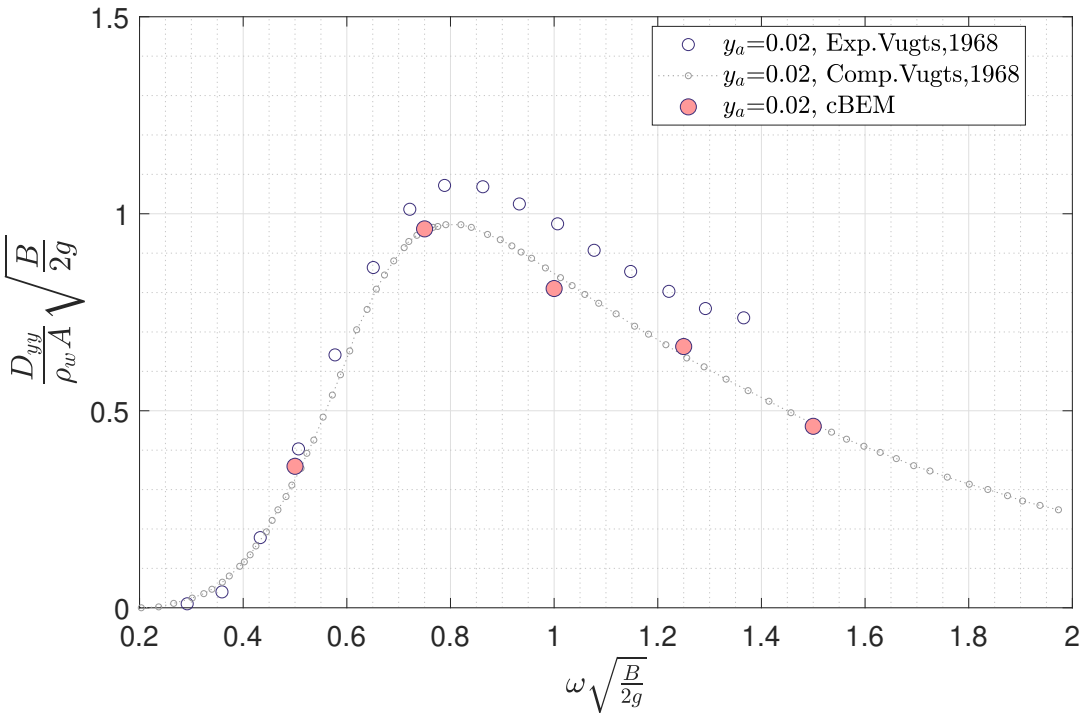

Figure 4.14: The variation of the damping coefficient with normalized angular frequency is presented for the sway motion and according to results from cBEM and results given in Vugts [177]. The cylinder is of rectangular cross-section and the breadth to draught ratio is $B/T_B = 2$.

Chapter 5

Final discussion and conclusions

The thesis is completed by giving a final discussion on the results in terms of the research hypotheses. It follows the conclusion and finally, possible further development steps and perspectives for future applications are outlined.

5.1 Final discussion

The final discussion on the accomplished results is done by reviewing the research hypotheses.

Review on research hypotheses

The motivation of this work is represented by the global hypothesis which is based on the research gap derived from the literature review, see Sec. (1.3). To realize the BEM solver, addressed in the GH, in the future, some novel concepts required proof of validity and new numerical methods. These tasks were separated into the research hypothesis RH1-RH6 and gave the frame for this thesis and the development of cBEM. The two-dimensional solver cBEM is the proof of concept and the foundation for the targeted three-dimensional BEM solver.

RH1: By replacing the κ-operator of global support with a Hypersingular BIO, the BEM solution converges to the first order HOS solution.

In the HOS method, κ represents the operator on which the evaluation of the nonlinear velocity potential and the vertical velocity at the free surface are based on, see West et al. [184]. After substituting the variables in the modified nonlinear free surface boundary condition, the integration in time gives the updated free surface velocity potential and surface elevation. The κ-operator of the velocity potential is evaluated by using the FFT justified by assuming the vector identity related to the surface Laplacian [184]. It states that the squared κ operator and the surface Laplacian of the velocity potential as well as

the product of the wavenumber vector with the potential's Fourier transform are equal, see Eq. (2.95). As it has been described by West et al. in [184], the use of only the FFT is favored over a combination of the FFT and the Finite Difference Method as it remains stable over the full wavenumber spectrum. The application of the FFT brings high efficiency, but also the limitation in terms of the global, continuous, modal basis functions used for the approximation of the solution space.
Because of this limitation, RH1 asks for a BIE formulation that represents the first order HOS approach, and the second applies a BEM approach to solve it. In the view of solution function space approximation, this represents the replacement of global basis functions by basis functions of compact support. This step was of relevance as it was the first proof of the concept and the basement for the next development steps. The NDBIE, Eq. (3.11), was considered for this problem and compared with the first order HOS solution, Eq. (3.39), indicated the representation of the κ-operator by the Hypersingular BIO in the BIE formulation. As this operator represents the influences of the water domain on itself, the assembly of the BIO included the self-, adjacent-, and far-regime evaluation of the hypersingular kernel function. The symmetric Galerkin approach incorporated the integration of both source and target domains and the modifications in the solution evaluation. To approximate the periodicity, the Method of Farfield Extension was applied.
In Subsec. (3.4.1) the convergence of the fsBEM solution to the first order HOS solution is demonstrated. The order of convergence and integration were the same and consistent with the polynomial degree of the second order Z-Spline function.
This represents both the validity of the BIE formulation and verified the fsBEM solver and the related BIO assembly. The proof of the ability of the interelement basis functions of compact support (Z-Splines) to approximate the solution obtained with the basis functions of global support, prepared the ground for the account of the free surface discontinuity.

RH2: Let Γ be a boundary with a discontinuous manifold $\Gamma_d \subset \Gamma$ (:= a set of connected elements where no solution function is defined on) then there exists a method that can assembly two operators one for the discontinuous domain Γ_d and one for the rest of the boundary domain $\Gamma_{FS} = \Gamma \setminus \Gamma_d$ so that the union of the two operators gives a solution that is equal to the solution of the full domain.
The consideration of a subset of connected elements referred to as discontinuity inside the water boundary domain was the next step for that a numerical solution was searched. This stage was of high relevance for the surface piercing body application. It introduced the theoretical method and contributed to the practical handling of the discontinuity and how it affected the solution. The involvement of the complex Hypersingular BIO represented a reliable test of the approach.
The separation of the discontinuous part from the free surface domain was modeled by truncating the basis function of compact support at the two occurring intersection points. A new method was developed for the evaluation of the self, adjacent and far regime in symmetric Galerkin formulation. The evaluation of the Hypersingular BIO was modified in such a manner, that for both subdomains individual operators had been assembled. The truncation of the water domain required the description of the position of the discontinuity for that new variables had to be introduced and evaluated in the preprocessing.
The BIE and the solving procedure were the same as used for RH1, with the difference that for the evaluation of the fsBEM, the sum of the free surface and discontinuous part of the Hypersingular BIO had been considered. After the assembly of the operators and the incorporation in the BIE formulation, the linear system was solved and the error between the first order HOS solution and the numerical results were evaluated.
It is shown in Subsec. (3.4.1), that the convergence for the truncated fsBEM was similar to that obtained for the continuous fsBEM. The verification of the methods related to the interelement basis functions proved the second hypothesis RH2.

RH3: Assume a mixed BVP that contains two separate boundary parts on that either a Dirichlet BVP or a Neumann BVP are defined and consider that a reference solution exists that employs a sufficiently differentiable analytic function to find the complete Cauchy data of the problem. Then the solution of a suited BIE system can be found by accounting for the Dirichlet and Neumann boundary data at the corresponding boundary parts and the error between the solution and the analytic Neumann and Dirichlet

datum of the reference is sufficiently small and converges at considerable order with increasing resolution.

After the two first hypotheses had been proved, the mixed BVP came into focus intending to solve hydrodynamic problems associated with submerged bodies interacting with waves. For the verification of RH3, the direct cBEM formulation, Eq. (3.8), was derived. This allowed the straightforward use of the evaluated densities without any postprocessing.

The eight BIOs represented the W2W, B2B, and coupled influences and had been individually assembled before being put in place in the cBEM block matrix. As the body was in this step considered to be submerged, no intersection of the boundaries occurred and only the farfield influences had to be taken into account for the Coupling BIOs. For the continuous water surface, the Hypersingular BIO assembly developed in RH1 was applied.

For the verification of the procedure, a suited reference solution was found by considering the analytic solution related to LWT, see Eqs. (3.24) and Eqs. (3.25). This procedure allowed to derive all densities at the boundaries and their employment as Neumann and Dirichlet boundary conditions at the body and water domain. Furthermore, the incorporation of the trigonometric function allows, as in RH1 and RH2, a reliable convergence analysis concerning the polynomial basis functions because no minimal error limitation occurs due to the inability of the polynomial bases to represent the trigonometric function exactly. The comparison of the numerical solution with the analytical solution indicated a reasonable error decay with h-refinement and proved the formulation of the coupled approach and the assembly of the BIOs in the symmetric Galerkin formulation.

RH4: Assume a mixed BVP that contains a combined boundary with a Dirichlet BVP and a Neumann BVP boundary part and consider that a reference solution exists that employs a sufficiently differentiable analytic function to find the complete Cauchy data of the problem. Then the solution of a suited BIE system with the Dirichlet and Neumann boundary data as boundary conditions at the corresponding boundary parts exists and the error between the solution and the analytic Neumann and Dirichlet datum of the reference is sufficiently small and converges at considerable order with increasing resolution.

RH4 faced the most typical problem that will be addressed with cBEM, the free surface piercing body. The considered discontinuity of the water boundary rose the complexity of the evaluation of the BIOs. Along with the submerged part of the body surface, a new boundary was formed and neighboring elements of Dirichlet and Neumann type asked for an adjacent regime evaluation method for the Coupling BIOs. The highest complexity was associated with the Hypersingular BIO. The testing of the developed approach was done with an analytic reference introduced in [19] and modified to account for interelement support and nearfield influence, see Subsec. (3.4.2). Based on this method also the weak and strongly singular kernels had been evaluated.

The verification of RH4 accounted again for the analytic LWT reference with which the boundary conditions could be defined and the cBEM solutions compared.

The error of the Neumann solution at the free surface was shown to decrease with second order and in the order of $\mathcal{O}(10^{-3})$ at the higher grid resolutions. This was reasonably small for the targeted application. The reduction of the convergence order and the increase in the error level originated from the account of the newly formed Dirichlet-Neumann boundary. The analysis of error influencing factors and their reduction should be accounted for in future studies.

The lower error on the body surface with an increasing number of body elements was subjected to the fact that intraelement basis functions were applied at the body boundary domain. The nearly constant error indicated that a lower accuracy limit was reached, not dominated by the representation of solution or geometry. The dominant factor for this error was related to the evaluation procedure of the combined Dirichlet-Neumann boundary.

By representing the solution of the cBEM method and showing that the obtained error was small, the RH4 was verified. Thereby, the stationary cases, where the proof of concept of the BIOs and the fsBEM and cBEM had been in focus, were completed and opened the field to the transient solver.

RH5: The application of the explicit Runge-Kutta time integration scheme for the wave dynamics

allows stable computations with high accuracy for submerged and surface piercing bodies in regular, small amplitude waves.
The evaluation of a transient solution made the integration of the variables in time necessary for that the explicit Runge-Kutta scheme to be employed. In this scheme, the wave variables had been updated by considering the linear kinematic and dynamic boundary conditions at the free surface. For the proof of the hypothesis, the LWT reference solution was considered again and gave the updated boundary conditions at the body surface. To have a consistent accuracy with the time stepping scheme, the boundary conditions were evaluated with a Taylor expansion of the corresponding order.
The stability of the transient cBEM solution was demonstrated by showing the constant shape of the wave in the space domain at distinct time steps. The accuracy was analyzed in terms of the time evolution of the error between the Cauchy data and the analytic reference. It was shown that the error reached a reasonably small error level around the error varied with small deviations.
For the practical use of the solver, it's of interest to identify the stability of the solution before the simulation started. This was realized by analyzing the linear stability of the dynamic system from which the eigenvalues of the wave dynamic system were derived, see Subsubsec. (3.2.3). By the multiplication of the eigenvalues with the time step, a comparison with the stability region of the Runge-Kutta time integration scheme was possible. This helped to identify insufficient discretization for resolving the dynamics right after the operator assembly and gave the possibility to cancel the simulation to improve the choice of the corresponding parameters.
The error evolution over a reasonable time range showed that the error stayed in a range around $\mathcal{O}(10^{-2})$ from that the sufficient stability and accuracy of the time stepping scheme was concluded. This verified RH5 and allowed to use cBEM for practical applications.

RH6: The monolithic coupling including the wave and body dynamics in the time domain by using a direct BIE formulation for mixed BVPs (incorporation of all BIOs) in symmetric Galerkin formulation is realizable and gives accurate results in hydrodynamic applications.
The use of cBEM for the analysis of typical two-dimensional hydrodynamic problems completed the levels of development considered within this thesis. The last research hypothesis, RH6, states the ability of cBEM to compute the dynamics of waves and their interaction with the body in hydrodynamic applications.
To prove the statement of RH6, the wave radiation due to a forced oscillating cylinder and the influence of the body on waves had been tested and compared with references from the literature. For the analysis in the time domain, evaluation methods for the hydrodynamic forces and coefficients had been implemented. The time stepping scheme was extended for the treatment of forced small amplitude motions of the body.
In the region of small submergence depth, it was found for the radiation problem that the hydrodynamic coefficients were well evaluable by cBEM, but were sensitive to the discretization parameters specifically for the damping coefficient. The use of this test case as an indicator for grid refinement could be considered in the future use. Also in the diffraction problem, the change of the phase of the transmitted wave due to the submerged fixed cylinder at rest and the amplitude of the hydrodynamic force agreed well with the theoretical values.
The uniform flow around the submerged cylinder was compared with the result of a linear solver by means of the resulting surface elevation. In the regime of subcritical Froude number deviations were indicated, but the comparability in terms of amplitude and wave length was good. For higher Froude numbers the results were promising. The account of the stream terms in the free surface boundary conditions and a suited ramp for the Neumann body condition were shown to be successfully implemented. For the surface piercing geometry, the comparison with computations indicated good accuracy as well. The considered oscillation in heave and sway mode and the resulting amplitude ratios as well as the added mass and the damping coefficient were treated well by cBEM.
Conclusively, the validation of cBEM in terms of different hydrodynamic applications and accounting submerged and surface piercing cylinders showed good comparability with the references over the range of accounted parameters and thus proved the last research hypothesis.

5.2 Conclusion

The presented work describes the development and testing of the novel symmetric Galerkin BEM solver cBEM that incorporated the HOS equations for the monolithic coupling of wave and body dynamics. This required the consideration of a discontinuity in the water domain that formed with the body boundary a mixed BVP. A solution for the coupled approach was found by a direct formulation that considered new evaluation methods for BIOs.
The review and categorization of previous literature on the topic of BEMs in the research field of hydrodynamics allowed the identification of the research gap and the derivation of the global hypothesis. For the scope of this work, six specific research hypotheses had been pointed out and framed the development of a two-dimensional linear solver version.
Based on integral equations, the formulations for the free surface solver, fsBEM, and the coupled solver cBEM were derived. The employment of BIOs required to evaluate weak, strong, and hypersingular kernel functions in the far-, near- and self-regime.
The favorable inversion with symmetric matrices, the lower requirements for continuity on the boundary domains, and the higher flexibility in the evaluation of surface intersections represented the arguments for the choice to the application of symmetric Galerkin formulation in cBEM. The integration of both source and target domain was considered for the assembly of the BIOs and the direct approach of Bonnet & Guiggiani [19] was applied for the desingularization of the kernel functions.
By expanding parametric coordinates in the Taylor series around the singularity, in this approach the hypersingular kernels have been decomposed in an analytic part and a numerically integrable part so that regular expressions were found for the self and direct neighbor influence for all types of singularity.
The incorporation of the HOS method in the BEM approach required approximating the spectral basis functions by locally valid representations. This was possible by employing Z-Splines [145] as basis functions which by construction meet this requirement. Thus, the continuous functions were replaced by solution representations of compact support.
The periodic boundary conditions were approximated by the Method of Farfield Extension. Here the computational domain was extended virtually and allowed the influence evaluation at a far distance. The solution remained valid only on the original domain, but by considering the extended farfield influences at this domain, a periodic-like solution could be found.
Showing that the solution of the integral method converged to the first order HOS solution proved the related hypothesis. The use of the HOS formulation in a BEM gives the basis for considering the nonlinear method without relying on spectral functions. It introduced the flexibility that was required for formulating a coupled approach for wave and body dynamics and allowed to consider a discontinuous surface as a boundary domain. In the context of this work, a discontinuous surface was referred to as a boundary domain that contained connected internal elements which did not belong to the rest of the domain. The assembly of independent BIOs for this part and the rest of the water domain and their subsequent summation to full domain BIOs resulted in the same solution that was obtained in the continuous case. Hereby, the necessary proof for stepping forward to the coupled approach was given as the main concern was about how to implement a HOS like BEM with a body inside the water domain.
The mixed BVP accounted for the body and water domain and was formulated in terms of a direct BIEM. The occurring coupling BIOs, representing the influence of water on the body and its reverse, had to be assembled. In the case of a surface piercing body, the union of the free surface and the submerged part of the body formed a mixed boundary domain. At the intersection points of the continuous original boundaries, Dirichlet and Neumann boundary parts are directly connected, and sharp geometries had to be considered. These locations required adjacent regime evaluation for the Coupling BIOs. Their development, implementation, and testing was major task as all kind of singular kernels had been considered and applications with other methods were possible only under restrictions.
For the analysis of the coupled motions in the time domain, the integration of the dynamic variables in time was added in cBEM. The Runge-Kutta scheme was chosen and the Taylor expansion terms up to the fourth order were used. The time stepping approves to be stable for the mixed BVP with submerged and

free surface piercing geometries. The simulations in the time domain allowed us to validate the solver in terms of academic (two-dimensional) test cases. Here the radiation and the diffraction problem, as well as a uniform flow were in the focus of the submerged body cases and the forced oscillations in heave and sway motion had been considered for the surface piercing body. The comparison with the literature in terms of hydrodynamic coefficients, and wave modifications due to the body and free surface elevations, showed accurate results that proved the ability to apply cBEM to marine hydrodynamics.
A recurring question was how to verify the developed methods. For the verification, analytic solutions were foremostly used, either by accounting for the first order HOS or LWT equations, or considering published work. Only with these reference solutions, the testing in cBEM and the proving of the hypotheses was feasible. Even small deviations from the correct BIE formulation, incorrect parts in the operator assemblies, or the desingularization of self and adjacent regime influences failed the test. Only with fully consistent approaches reasonably small errors were reached which indicated the correct implementation. With the LWT equation, all densities at the water surface were available and could be derived at the body surface. By defining the body boundary data consistent with the free surface boundary conditions an optimal test setup for the approach was found that also gave a strong test case for the transient solver.
The limitations of the here developed cBEM solver are at first the account of only two spatial dimensions and linearized wave dynamics. The body motion is considered to be of small amplitude and occurs around an equilibrium position which yields a solution without solving the rigid body motion and updating the BIOs. Furthermore, cBEM was implemented in a non optimized test environment and consequently, an analysis of the optimal ratio between accuracy and efficiency was not in focus.
The focus of this thesis was the proof of basic hypotheses to realize an innovative BEM solver. For this, the use of the HOS approach for integral equation approaches was realized so that an efficient solution of wave propagation with subsequent integration of nonlinear terms is achievable. The consideration of surface discontinuities and the presentation of associated highly accurate solutions represents an innovative step in the research field. Hereby, a way to integrate the HOS-like approach in a BEM solver is found. The potential of such an approach was presented by obtaining accurate time domain solutions with cBEM.
cBEM includes a toolbox on that basis a wide field of applications in marine hydrodynamics could be reached. Plausible future applications for the solver are highlighted and their potential in research and industry is described in the next section. The missing steps in the actual solver for accomplishing the specific approaches are outlined, and from that the main future development stages in cBEM are derived.

5.3 Future perspectives

The potential of cBEM in the field of Marine Hydrodynamics can be manifold. This reflects the idea outlined in the introduction of not committing to one of the three main BEM streams, but allowing a more flexible choice of scope.

Applications cBEM

The field of potential applications of cBEM include:

- hydrodynamic analysis in numerical wave tanks,
- modeling of fluid-structure interaction in an open ocean environment,
- support in the design of ships, boats and structures,
- and deterministic wave and motion prediction.

Concerning the first field, the boundary conditions for the wave board, the wave energy absorption, and the bathymetry are not considered yet in the actual solver. By their inclusion in the solver,

experiments in model scale could be prepared with cBEM and a direct comparison with wave tank measurements would be feasible. A possible application could be the analysis of wave-ice interaction for the water boundary would be partly modified to consider bending, inertia, and compression of the modeled ice and would give in addition to the free surface a new mixed BVP.
With the implementation in three dimensions, the account of nonlinear terms, and the use of computationally highly efficient methods an even more relevant test setup would be available and short crested sea states could be considered.
The successive increase of complexity in the numerical wave tank would open cBEM to a wide research area for the analysis of nonlinear wave-body dynamics, see Sec. (1.2), and introduce it as a competitive solver in the field of BIEMHs.

The application of the solver in the open ocean environment requires the nonlinear HOS approach and the implementation in three dimensions. Ducrozet et al. [54] have introduced an open source HOS solver for open ocean simulations and the wide use of such approaches in the research field indicates the interest in realistic sea state modeling.
With the ocean environment, a setup for analyzing the seakeeping behavior of ships in the open sea would exist. Recently, Choi et al. [29] have presented a coupled HOS-CFD approach and have indicated the potential of the approach in the field of the analysis of ship and nonlinear wave interaction.
In contrast to coupling approaches that account for different solvers, a three-dimensional cBEM solver would have the potential to solve the mixed BVP more efficiently, because the monolithic coupling approach accounts for the complete problem at once and no transition between two solutions of different solvers would be required. Investigation for that typically nonlinear RSGF methods are used, e.g. wave resistance evaluation could be extended as the incorporation of the HOS method allows for testing ship maneuvers in deterministic sea states. The analysis of operations under speed, with the ship at a rest and during dynamic positioning, would be feasible and could support the planning and optimization of ship operations.

These environmental test setups are of relevance from the perspective of digital twins and software in the loop (SiL) applications. The role of digital twins as a mirror image of real ships plays an increasing role in testing different load cases, optimizing ship performance, and planning ship routes. By using highly accurate geometry approximations, the performance of complex ship hulls and structures can be well analyzed and cBEM represents an optimal environment for testing the digital twins.
The embedding of cBEM in SiL test benches will be reasonable as the fast interaction of the solver and the experimental setup will be viable due to high computational efficiency. A possible SiL experiment could be to include cBEM in a study on the operating limits of machines. The hydrodynamic loads determined with cBEM from different sea state scenarios could be transferred to a hexapod. The operation of the machine mounted on the hexapod could then be analyzed for varying wave heights or roll accelerations, and limits for the trouble-free operation could be derived.

The performance of a design should be known best before the start of the construction phase of the ship. All previous facets for the use of cBEM could be used in the very early project phases, e.g. in cooperation with hull optimization tools, to test different designs and then in accompany by a model test to choose the final candidate. The support in the design phase would be in principle beneficial for a wider range of ship classes and offshore structures and could be useful for different stakeholders in the maritime industry.

The prediction of waves and motions by a deterministic approach, see e.g. linear methods of Naaijen et al. [118] and Kusters et al. [101] for commercial applications and of Clauss et al. [31], Kosleck [98] and Fucile [60] in the field of research, is probably the most innovative field for that cBEM would be applicable and that is a target within the global hypothesis. The term 'deterministic' in the context of sea state prediction accounting for the phase resolving ability of the method and intends the use of observations for the input to wave propagation methods.
Three main concerns make innovations towards nonlinear methods in this field very challenging. First the reconstruction of wave properties from the radar signal and second the coupling of wave and body dynamics in a nonlinear time domain approach. Third, the computation of wave inversion, propagation,

and motion response faster than real time, to end up with a true prediction, has to be realized.
A novel method for the nonlinear reconstruction of waves has been introduced in Desmars et al. [48, 49], where a grid based method has been used in that the wave variables have mapped to the radar observations and have propagated in space and time by accounting the nonlinear HOS equations. For the second challenge, cBEM gives the optimal basis approach as it considers wave and body dynamics in a coupled approach. The incorporation of the HOS procedure in the BEM environment was proved by this thesis.
The holistic concept would use the regular HOS grid as the HOS method has shown to be favorable compared to other methods, see Klein et al. [95], due to its efficiency and the consideration of nonlinear and broad banded ocean waves. The HOS grid would be thus used as the central element in the approach where the reconstruction and propagation lands and the motion solver starts. The applicability of acceleration techniques and the use of GPU give rise to expect that also the third challenge can be handled and computation times faster than the simulation time can be realizable with the holistic approach.
The potential of this approach for the offshore and ship industry is high. Nowadays most applied statistical approach account for the significant wave heights with a safety factor and use the wave forecast for deciding operability. Alternatively, linear methods for wave and motion prediction are available and in use, see e.g. Naaijen et al. [118] and Kusters et al. [101].
Replacing these methods with a nonlinear holistic physic-based approach, give the chance to assess the situation at the location with higher accuracy compared to the linear prediction methods. Both the security and the days of operations per year could be increased, yielding an optimization of offshore operations.

Coming back to the future development steps, the implementation of the method in three dimensions and the use of acceleration techniques are most relevant and give the track to many applications in the context of marine hydrodynamics.

With the proof of the research hypotheses, the conceptual foundation for the three-dimensional BEM solver is finalized and cBEM can be used as a platform for further developments. The conceivable steps in the short to medium term period are categorized into four parts, namely the

Future developments

1 account of rigid body dynamics,

2 the implementation in three dimensions,

3 the utilization of acceleration techniques,

4 and the account of nonlinear phenomena.

Stage one implies first the incorporation of a motion solver in cBEM. The body's acceleration is evaluated by the equation of motion accounting for the body characteristics, hydrodynamic coefficients, and hydrostatic restoring. Employing the time integration scheme will yield the velocity at the body surface. Therefore secondly, the relative positions of the free surface and body geometries will be updated and the BIOs will be assembled newly. Under the assumption of small motions, this concerns only the near and adjacent Coupling BIOs. The consideration of the body dynamics requires a review of the stability and accuracy of the solver before this task is completed.

By the future development step two, the approach is extended to three dimensions. This fore mostly requires a numerical method that handles the free surface discontinuity. The efficient evaluation of the Dirichlet-Neumann intersection of the mixed BVP, represented by a closed curved line in three dimensions, with the constraint to not significantly decrease the accuracy will be a challenging task and represent a relevant step toward the global hypothesis. The desingularization of the BIOs will be a further complex task that has to be completed for the successful implementation in three dimensions.

The highly efficient computation of hydrodynamic problems is a key specification of the new solver. To realize time saving computations up to real time capability, the use of acceleration techniques is required. The FMM and pFFT techniques are well integrable in BEM environments and represent potential methods for cBEM. The applicability of these approaches for the discontinuous solver has to be checked

and necessary modifications have to be accomplished before implementation in cBEM will follow. The efficiency of the solver could then be highlighted by suited benchmark tests and checked for real time capability.

The last task for the proof of the global hypothesis is the account of nonlinear mechanisms related to wave dynamics and the interaction between waves and bodies. This is assumed to significantly increase the accuracy first in modeling wave physics due to the account of the correct wave shape, the Stokes drift, and the interaction between wave components. Second, the small resistance of the floating body to roll motion cause sensitive reactions to wave excitation in this mode and results typically in nonlinear motions. As these considerations play a relevant role in the ship's safety, the accurate modeling of these cases is of special interest and might be applied in the design process.

As a first step, the increase in accuracy will be obtained by accounting for the actual wetted body surface. The incorporation of the nonlinear equations for the wave dynamics will follow. This requires the indirect BEM approach and the use of the HOS method in a postprocessing step. The consideration of nonlinear body motion will be included thereafter and parameterized models for capturing viscous effects might be considered.

Alongside these larger development stages, the optimal ratio between efficiency and accuracy has to be found. The definition of benchmark cases and their systematic analysis for varying computational parameters and characteristic numbers will allow a detailed study of the error influencing parameters and the identification of the ideal setup for highly efficient simulations.

By reviewing these stages according to the global hypothesis, the consistency of this conjecture is indicated and approved for future developments.

Bibliography

[1] R. A. Adams and J. J. F. Fournier. *Sobolev spaces*. Elsevier, 2003.

[2] J. H. Ahlberg, E. N. Nilson, and J. L. Walsh. Best approximation and convergence properties of higher-order spline approximations. *Journal of Mathematics and Mechanics*, 14(2):231–243, 1965.

[3] J. H. Ahlberg, E. N. Nilson, and J. L. Walsh. Convergence properties of generalized splines. *Proceedings of the National Academy of Sciences*, 54(2):344–350, 1965.

[4] G. B. Airy. On tides and waves: Encylopaedia metropolitana, vol. 5 (mixed sciences), 1845.

[5] X. Antoine and M. Darbas. *Numerical Methods for Acoustics Problems*, chapter Integral equations and iterative schemes for acoustic scattering problems. Saxe-Coburg Editors, 2016.

[6] J. J. M. Baar and W. G. Price. Evaluation of the wavelike disturbance in the kelvin wave source potential. *Journal of Ship Research*, 32(01):44–53, 1988.

[7] A. Babarit and G. Delhommeau. Theoretical and numerical aspects of the open source bem solver nemoh. In *11th European wave and tidal energy conference (EWTEC2015)*, 2015.

[8] C. Balakrishna, L. J. Gray, and J. H. Kane. Efficient analytical integration of symmetric galerkin boundary integrals over curved elements; elasticity formulation. *Computer methods in applied mechanics and engineering*, 117(1-2):157–179, 1994.

[9] C. Balakrishna, L. J. Gray, and J. H. Kane. Efficient analytical integration of symmetric galerkin boundary integrals over curved elements: thermal conduction formulation. *Computer methods in applied mechanics and engineering*, 111(3-4):335–355, 1994.

[10] G. Beer, B. Marussig, and C. Duenser. *The isogeometric boundary element method*. Springer, 2020.

[11] V. Bertram. Ship motions by a rankine source method. *Ship Technology Research*, 37(4):143–153, 1990.

[12] V. Bertram and H. Yasukawa. Rankine source methods for seakeeping problems. *Jahrbuch Schiffbautechn. Gesellschaft*, pages 411–425, 1996.

[13] P. Bézier. Mathematical and practical possibilities of unisurf. In *Computer aided geometric design*, pages 127–152. Elsevier, 1974.

[14] P. E. Bézier. How renault uses numerical control for car body design and tooling. Technical report, SAE Technical Paper, 1968.

[15] G. Birkhoff and H. L. Garabedian. Smooth surface interpolation. *Journal of Mathematics and Physics*, 39(1-4):258–268, 1960.

[16] G. Bonnet. A general regularization of the hypersingular integrals in the symmetric galerkin boundary element method. *International journal for numerical methods in engineering*, 80(8):1110–1123, 2009.

[17] M. Bonnet. Regularized direct and indirect symmetric variational bie formulations for three-dimensional elasticity. *Engineering Analysis with Boundary Elements*, 15(1):93–102, 1995.

[18] M. Bonnet. Boundary integral equation methods for solids and fluids. *Meccanica*, 34(4):301–302, 1999.

[19] M. Bonnet and M. Guiggiani. Direct evaluation of double singular integrals and new free terms in 2d (symmetric) galerkin bem. *Computer methods in applied mechanics and engineering*, 192(22-24):2565–2596, 2003.

[20] M. Bonnet, G. Maier, and C. Polizzotto. Symmetric galerkin boundary element methods. *Applied Mechanics Reviews*, 1998.

[21] B. Borgarino, A. Babarit, and P. Ferrant. Extension of free-surface green's function multipole expansion for infinite water depth case. *International Journal of Offshore and Polar Engineering*, 21(03), 2011.

[22] J. Bremer. On the nyström discretization of integral equations on planar curves with corners. *Applied and Computational Harmonic Analysis*, 32(1):45–64, 2012.

[23] J. Bremer and Z. Gimbutas. A nyström method for weakly singular integral operators on surfaces. *Journal of computational physics*, 231(14):4885–4903, 2012.

[24] I. N. Bronstein, K. A. Semendjajew, G. Musiol, and H. Mühlig. *Taschenbuch der Mathematik*, volume 1. Springer-Verlag, 9 edition, 2013.

[25] C. Canuto, M. Y. Hussaini, A. Quarteroni, and T. A. Zang. *Spectral methods: Evolution to Complex Geometries and Applications to Fluid Dynamics*. Springer Science & Business Media, 2007.

[26] C. Canuto, M. Y. Hussaini, A. Quarteroni, and T. A. Zang. *Spectral methods: Fundamentals in Single Domains*. Springer Science & Business Media, 2007.

[27] S. K. Chakrabarti. *Hydrodynamics of offshore structures*. WIT press, 1987.

[28] X. B. Chen. Free surface green function and its approximation by polynomial series. In *in: Bureau Veritas' research report No 641 DTO/XC*, 1991.

[29] Y. M. Choi, B. Bouscasse, G. Ducrozet, S. Seng, P. Ferrant, E. S. Kim, and Y. J. Kim. An efficient methodology for the simulation of nonlinear irregular waves in computational fluid dynamics solvers based on the high order spectral method with an application with openfoam. *International Journal of Naval Architecture and Ocean Engineering*, 15:100510, 2023.

[30] J. M. Clarisse. *On the numerical evaluation of the Neumann-Kelvin Green function*. PhD thesis, Massachusetts Institute of Technology, 1989.

[31] G. F. Clauss, M. Klein, M. Dudek, and M. Onorato. Deterministic non-linear wave forecast and motion prediction for short-term offshore operations. In *The Twenty-fifth International Ocean and Polar Engineering Conference*. International Society of Offshore and Polar Engineers, 2015.

[32] G. F. Clauss, E. Lehmann, and C. Östergaard. *Meerestechnische Konstruktionen*. Springer Verlag, 1988.

[33] A. H. Clément. A second order ordinary differential equation for the frequency domain green function. In *28th International workshop on water waves and floating bodies*, 2013.

[34] J. W. Cooley and J. W. Tukey. An algorithm for the machine calculation of complex fourier series. *Mathematics of computation*, 19(90):297–301, 1965.

[35] M. G. Cox. The numerical evaluation of b-splines. *IMA Journal of Applied mathematics*, 10(2):134–149, 1972.

[36] W. E. Cummins. The impulse response function and ship motions. Technical Report 1661, Department of the Navy, David W. Taylor Model Basin, Hydromechanics Laboratory, 1962.

[37] P. J. Davis and P. Rabinowitz. *Methods of Numerical Integration*. Academic Press, 2nd edition edition, 1984.

[38] C. W. Dawson. A practical computer method for solving ship-wave problems. In *Proceedings of Second International Conference on Numerical Ship Hydrodynamics*, pages 30–38, 1977.

[39] C. De Boor. Bicubic spline interpolation. *Journal of mathematics and physics*, 41(1-4):212–218, 1962.

[40] C. De Boor. On calculating with b-splines. *Journal of Approximation theory*, 6(1):50–62, 1972.

[41] C. De Boor. *A practical guide to splines*. Applied mathematical sciences. Springer, New York, Heidelberg u.a., rev. ed., 1. hardcover print. edition, 2001. Literaturverz. S. 331 - 339.

[42] P. De Casteljau. Outillages méthodes calcul. *Andr e Citro en Automobiles SA, Paris*, 4:25, 1959.

[43] B. De Jong. Berekening van de hydromechanische coëfficiënten van oscillerende cilinders. *TUDelft, Faculty of Marine Technology, Ship Hydromechanics Laboratory, Report No. 174*, 1967.

[44] W. R. Dean. On the reflexion of surface waves by a submerged circular cylinder. In *Mathematical Proceedings of the Cambridge Philosophical Society*, volume 44, pages 483–491. Cambridge University Press, 1948.

[45] G. Delhommeau. Amélioration des performances des codes de calcul de diffraction-radiation au premier ordre. *Proceedings of the 2èmes Journées de l'Hydrodynamique, Nantes, France*, pages 13–15, 1989.

[46] G. Delhommeau. Seakeeping codes aquadyn and aquaplus. *19th WEGMENT School, numerical simulation of hydrodynamics: ship and offshore structures*, 1993.

[47] J. D'Elía, L. Battaglia, and M. Storti. A semi-analytical computation of the kelvin kernel for potential flows with a free surface. *Computational & Applied Mathematics*, 30:267–287, 2011.

[48] N. Desmars, M. Hartmann, J. Behrendt, M. Klein, and N. Hoffmann. Reconstruction of ocean surfaces from randomly distributed measurements using a grid-based method. In *International Conference on Offshore Mechanics and Arctic Engineering*, volume 85161, page V006T06A059. American Society of Mechanical Engineers, 2021.

[49] N. Desmars, M. Hartmann, J. Behrendt, M. Klein, and N. Hoffmann. Nonlinear reconstruction and prediction of regular waves. In *41st International Conference on Offshore Mechanics and Arctic Engineering*, June 2022.

[50] J. W. Dold and D. H. Peregrine. Steep unsteady water waves: an efficient computational scheme. In *Coastal Engineering 1984*, pages 955–967. 1985.

[51] E. Dombre, M. Benoit, D. Violeau, C. Peyrard, and S. T. Grilli. Simulation of floating structure dynamics in waves by implicit coupling of a fully non-linear potential flow model and a rigid body motion approach. *Journal of Ocean Engineering and Marine Energy*, 1(1):55–76, 2015.

[52] E. Dombre, J. C. Harris, M. Benoit, D. Violeau, and C. Peyrard. A 3d parallel boundary element method on unstructured triangular grids for fully nonlinear wave-body interactions. *Ocean Engineering*, 171:505–518, 2019.

[53] D. G. Dommermuth and D. K. Yue. A high-order spectral method for the study of nonlinear gravity waves. *Journal of Fluid Mechanics*, 184:267–288, 1987.

[54] G. Ducrozet, F. Bonnefoy, D. Le Touzé, and P. Ferrant. Hos-ocean: Open-source solver for nonlinear waves in open ocean based on high-order spectral method. *Computer Physics Communications*, 203:245–254, 2016.

[55] L. Ehrenpreis. Solution of some problems of division: Part i. division by a polynomial of derivation. *American Journal of Mathematics*, 76(4):883–903, 1954.

[56] B. O. el Moctar, T. E. Schellin, and H. Söding. *Numerical Methods for Seakeeping Problems*. Springer, 2021.

[57] L. M. Faria, C. Pérez-Arancibia, and M. Bonnet. General-purpose kernel regularization of boundary integral equations via density interpolation. *Computer Methods in Applied Mechanics and Engineering*, 378:113703, 2021.

[58] A. Frangi. Fracture propagation in 3d by the symmetric galerkin boundary element method. *International Journal of Fracture*, 116(4):313–330, 2002.

[59] W. Frank. Oscillation of cylinders in or below the free surface of deep fluids. Technical report, David W Taylor Naval Ship Research and Development Center Bethesda MD Dept of Hydromechanics, 1967.

[60] F. Fucile. *Deterministic sea wave and ship motion forecasting: from remote wave sensing to prediction error assessment*. PhD thesis, University of Triest, 2017.

[61] G. E. Gadd. A method of computing flow and surface wave pattern around full forms, trans. *Royal Institution of Naval Architects*, 18, 1976.

[62] L. J. Gray. Evaluation of singular and hypersingular galerkin integrals: direct limits and symbolic computation. *Singular Integrals in Boundary Element Methods, Comp. Mech. Publ., Southampton*, pages 45–84, 1998.

[63] S. T. Grilli, P. Guyenne, and F. Dias. A fully non-linear model for three-dimensional overturning waves over an arbitrary bottom. *International journal for numerical methods in fluids*, 35(7):829–867, 2001.

[64] S. T. Grilli and J. Horrillo. Numerical generation and absorption of fully nonlinear periodic waves. *Journal of engineering mechanics*, 123(10):1060–1069, 1997.

[65] S. T. Grilli, J. Skourup, and I. A. Svendsen. An efficient boundary element method for nonlinear water waves. *Engineering Analysis with Boundary Elements*, 6(2):97–107, 1989.

[66] S. T. Grilli and R. Subramanya. Quasi-singular integrals in the modeling of nonlinear water waves in shallow water. *Engineering Analysis with Boundary Elements*, 13(2):181–191, 1994.

[67] S. T. Grilli and I. A. Svendsen. Corner problems and global accuracy in the boundary element solution of nonlinear wave flows. *Engineering Analysis with Boundary Elements*, 7(4):178–195, 1990.

[68] E. Guerber, M. Benoit, S. T. Grilli, and C. Buvat. A fully nonlinear implicit model for wave interactions with submerged structures in forced or free motion. *Engineering Analysis with Boundary Elements*, 36(7):1151–1163, 2012.

[69] P. Guevel, J. C. Daubisse, and G. Delhommeau. Oscillation of floating bodies subjected to wave action. 1978.

[70] M. Guiggiani. Hypersingular boundary integral equations have an additional free term. *Computational Mechanics*, 16(4):245–248, 1995.

[71] M. Guiggiani. Formulation and numerical treatment of boundary integral equations with hypersingular kernels. *Singular integrals in boundary element methods*, 10:85–124, 1998.

[72] M. Guiggiani and A. Gigante. A general algorithm for multidimensional cauchy principal value integrals in the boundary element method. *Journal of Applied Mechanics*, 1990.

[73] M. Guiggiani, G. Krishnasamy, T. J. Rudolphi, and F. Rizzo. A general algorithm for the numerical solution of hypersingular boundary integral equations. *Journal of Applied Mechanics*, 1992.

[74] J. C. Harris, E. Dombre, M. Benoit, and S. T. Grilli. Fast integral equation methods for fully nonlinear water wave modeling. In *The Twenty-fourth International Ocean and Polar Engineering Conference*. OnePetro, 2014.

[75] J. C. Harris, E. Dombre, M. Benoit, S. T. Grilli, and K. I. Kuznetsov. Nonlinear time-domain wave-structure interaction: A parallel fast integral equation approach. *International Journal for Numerical Methods in Fluids*, 94(2):188–222, 2022.

[76] M. Haskind and J. Newman. The exciting forces and wetting of ships in waves. Technical report, DAVID TAYLOR MODEL BASIN WASHINGTON DC, Translation from russian original publication: Haskind, 1957, 'Vozmushchayushchie Sili i Zativemos' Sudov na Volnenii', 1962.

[77] T. H. Havelock. The wave-making resistance of ships: a theoretical and practical analysis. *Proceedings of the Royal Society of London. Series A, Containing Papers of a Mathematical and Physical Character*, 82(554):276–300, 1909.

[78] T. H. Havelock. The theory of wave resistance. *Proceedings of the Royal Society of London. Series A, Containing Papers of a Mathematical and Physical Character*, 138(835):339–348, 1932.

[79] T. H. Havelock. The forces on a circular cylinder submerged in a uniform stream. *Proceedings of the Royal Society of London. Series A-Mathematical and Physical Sciences*, 157(892):526–534, 1936.

[80] T. H. Havelock. Waves due to a floating sphere making periodic heaving oscillations. *Proceedings of the Royal Society of London. Series A. Mathematical and Physical Sciences*, 231(1184):1–7, 1955.

[81] G. E. Hearn. Alternative methods of evaluating green's function in three-dimensional ship-wave problems. *Journal of Ship Research*, 21(02):89–93, 1977.

[82] J. L. Hess and A. M. O. Smith. Calculation of nonlifting potential flow about arbitrary three-dimensional bodies. *Journal of ship research*, 8(04):22–44, 1964.

[83] J. L. Hess and A. M. O. Smith. Calculation of potential flow about arbitrary bodies. *Progress in Aerospace Sciences*, 8:1–138, 1967.

[84] J. C. Holladay. A smoothest curve approximation. *Mathematical tables and other aids to computation*, 11(60):233–243, 1957.

[85] Y. Huang. *Nonlinear ship motions by a Rankine panel method*. PhD thesis, Massachusetts Institute of Technology, 1997.

[86] V. Hutson, J. Pym, and M. Cloud. *Applications of functional analysis and operator theory*. Elsevier, 2005.

[87] G. Jensen. Berechnung der stationären potentialströmung um ein schiff unter berücksichtigung der nichtlinearen randbedingung an der wasseroberfläche. Technical Report 484, Institut für Schiffbau der Universität Hamburg, 1988.

[88] G. Jensen, H. Söding, and Z. Mi. Rankine source methods for numerical solutions of the steady wave resistance problem. In *Sixteenth Symposium on Naval Hydrodynamics*, 1986.

[89] F. John. On the motion of floating bodies ii. simple harmonic motions. *Communications on pure and applied mathematics*, 3(1):45–101, 1950.

[90] J. Katsikadelis. *The boundary element method for engineers and scientists: theory and applications*. Academic Press, 2016.

[91] J. Katz and A. Plotkin. *Low-speed aerodynamics*, volume 13. Cambridge university press, 2001.

[92] G. H. Keulegan, L. H. Carpenter, et al. *Forces on cylinders and plates in an oscillating fluid*. National Bureau of Standards, 1956.

[93] W. D. Kim. On the harmonic oscillations of a rigid body on a free surface. *Journal of Fluid Mechanics*, 21(3):427–451, 1965.

[94] B. K. King, R. F. Beck, and A. R. Magee. Seakeeping calculations with forward speed using time domain analysis. In *Proc. 17th Symp. on Naval Hydrodynamics*, pages 577–596, 1988.

[95] M. Klein, M. Dudek, G. F. Clauss, S. Ehlers, J. Behrendt, N. Hoffmann, and M. Onorato. On the deterministic prediction of water waves. *Fluids*, 5(1):9, 2020.

[96] J.-M. Kobus. *Application de la méthode des singularités au problème des flotteurs cylindriques soumis à des oscillations harmoniques forcées de faible amplitude*. PhD thesis, Univ. Nantes, 1976.

[97] F. T. Korsmeyer, D. K. P. Yue, K. Nabors, and J. White. Multipole-accelerated preconditioned iterative methods for three-dimensional potential problems. *WIT Transactions on Modelling and Simulation*, 1, 1970.

[98] S. Kosleck. *Prediction of wave-structure interaction by advanced wave field forecast*. PhD thesis, Universitätsbibliothek der Technischen Universität Berlin, 2013.

[99] D. C. Kring. *Time domain ship motions by a three-dimensional Rankine panel method*. PhD thesis, Massachusetts institute of technology, 1994.

[100] R. Kurnia and G. Ducrozet. Nemoh: Open-source boundary element solver for computation of first-and second-order hydrodynamic loads in the frequency domain. *Available at SSRN 4396951*, 2023.

[101] J. G. Kusters, K. L. Cockrell, B. S. H. Connell, J. P. Rudzinsky, and V. J. Vinciullo. Futurewaves™: A real-time ship motion forecasting system employing advanced wave-sensing radar. In *OCEANS 2016 MTS/IEEE Monterey*, pages 1–9. IEEE, 2016.

[102] H. Lamb. *Hydrodynamics*. The University Press, 1895.

[103] C.-H. Lee. *Numerical methods for boundary integral equations in wave body interactions*. PhD thesis, Massachusetts Institute of Technology, 1988.

[104] C.-H. Lee. *WAMIT theory manual*. Massachusetts Institute of Technology, Department of Ocean Engineering, 1995.

[105] C.-H. Lee and J. N. Newman. Computation of wave effects using the panel method. *WIT Transactions on State-of-the-art in Science and Engineering*, 18, 2005.

[106] C.-H. Lee and P. D. Sclavounos. Removing the irregular frequencies from integral equations in wave-body interactions. *Journal of Fluid Mechanics*, 207:393–418, 1989.

[107] H.-B. Li, G.-M. Han, and H. A. Mang. A new method for evaluating singular integrals in stress analysis of solids by the direct boundary element method. *International Journal for Numerical Methods in Engineering*, 21(11):2071–2098, 1985.

[108] W. M. Lin, J. N. Newman, and D. K. P. Yue. Nonlinear forced motions of floating bodies. In *Fifteenth Symposium on Naval Hydrodynamics*, 1984.

[109] W.-M. Lin and D. Yue. Numerical solution for large-amplitude ship motions in the time-domain. In *Eighteenth Symposium on Naval Hydrodynamics*. National Academy of Sciences, 1991.

[110] W.-M. Lin and D. K. P. Yue. Time-domain analysis for floating bodies in mild-slope waves of large amplitude. In *Proceedings of the Eighth International Workshop on Water Waves and Floating Bodies*, 1993.

[111] Y. Liu, M. Xue, and D. K. P. Yue. Computations of fully nonlinear three-dimensional wave–wave and wave–body interactions. part 2. nonlinear waves and forces on a body. *Journal of Fluid Mechanics*, 438:41–66, 2001.

[112] M. S. Longuet-Higgins and E. D. Cokelet. The deformation of steep surface waves on water-i. a numerical method of computation. *Proceedings of the Royal Society of London. A. Mathematical and Physical Sciences*, 350(1660):1–26, 1976.

[113] B. Malgrange. Existence et approximation des solutions des équations aux dérivées partielles et des équations de convolution. In *Annales de l'institut Fourier*, volume 6, pages 271–355, 1956.

[114] D. Martin. Résolution numérique du problème linéarisé de la tenue à la mer. *BULL. ASSOC. TECH. MAR. AERONAUT.*, 1980.

[115] C. C. Mei, M. Stiassnie, and D. Yue. *Theory and applications of ocean surface waves-Linear aspects*, volume 23. World Scientific Publishing CO. Pte. Ltd, Advanced series on ocean engineering, 2005.

[116] K. S. Miller. On the inverse of the sum of matrices. *Mathematics magazine*, 54(2):67–72, 1981.

[117] S. Motora. Stripwise calculation of hydrodynamic forces due to beam seas. Technical report, Stevens Institute of Technology, 1962.

[118] P. Naaijen, R. R. T. Van Dijk, R. H. M. Huijsmans, and A. A. El-Mouhandiz. Real time estimation of ship motions in short crested seas. In *International conference on offshore mechanics and arctic engineering*, volume 43444, pages 243–255, 2009.

[119] K. Nabors, F. T. Korsmeyer, F. T. Leighton, and J. White. Preconditioned, adaptive, multipole-accelerated iterative methods for three-dimensional first-kind integral equations of potential theory. *SIAM Journal on Scientific Computing*, 15(3):713–735, 1994.

[120] K. Nabors, J. Phillips, F. T. Korsmeyer, and J. White. 12. multipole and precorrected-FFT accelerated iterative methods for solving surface integral formulations of three-dimensional laplace problems. In *Domain-Based Parallelism and Problem*

Decomposition Methods in Computational Science and Engineering, pages 193–215. Society for Industrial and Applied Mathematics, jan 1995.

[121] D. Nakos and P. Sclavounos. Ship motions by a three-dimensional rankine panel method. In *Eighteenth Symposium on Naval Hydrodynamics*, 1991.

[122] D. E. Nakos. *Ship wave patterns and motions by a three dimensional Rankine panel method*. PhD thesis, Massachusetts Institute of Technology, 1990.

[123] D. E. Nakos and P. D. Sclavounos. On steady and unsteady ship wave patterns. *Journal of Fluid Mechanics*, 215:263–288, 1990.

[124] J. N. Newman. The exciting forces on fixed bodies in waves. *Journal of Ship Research*, 6(04):10–17, 1962.

[125] J. N. Newman. Algorithms for the free-surface green function. *Journal of engineering mathematics*, 19(1):57–67, 1985.

[126] J. N. Newman. Distributions of sources and normal dipoles over a quadrilateral panel. *Journal of Engineering Mathematics*, 20(2):113–126, 1986.

[127] J. N. Newman. Evaluation of the wave-resistance green function: Part 1—the double integral. *Journal of ship research*, 31(02):79–90, 1987.

[128] J. N. Newman. The approximation of free-surface green. *Wave asymptotics*, page 107, 1992.

[129] J. N. Newman. *Marine hydrodynamics*. The MIT press, 2018. 40th anniversary edition.

[130] J. N. Newman and C.-H. Lee. Boundary-element methods in offshore structure analysis. *J. Offshore Mech. Arct. Eng.*, 124(2):81–89, 2002.

[131] F. Noblesse. On the theory of flow of regular water waves about a body. Technical report, Massachusettes Inst of Tech Cambridge Dept of Ocean Engineering, 1980.

[132] F. Noblesse. The green function in the theory of radiation and diffraction of regular water waves by a body. *Journal of Engineering Mathematics*, 16(2):137–169, 1982.

[133] T. F. Ogilvie. First-and second-order forces on a cylinder submerged under a free surface. *Journal of Fluid Mechanics*, 16(3):451–472, 1963.

[134] T. F. Ogilvie and Y. S. Shin. Integral-equation solutions for time-dependent free-surface problems. *Journal of the Society of Naval Architects of Japan*, 1978(143):41–51, 1978.

[135] T. F. Ogilvie and E. O. Tuck. A rational strip theory of ship motions: part i. Technical report, University of Michigan, 1969.

[136] P. W. Partridge, C. A. Brebbia, and L. C. Wrobel. *Dual reciprocity boundary element method*. Springer Science & Business Media, 2012.

[137] C. Pérez-Arancibia, L. M. Faria, and C. Turc. Harmonic density interpolation methods for high-order evaluation of laplace layer potentials in 2d and 3d. *Journal of Computational Physics*, 376:411–434, 2019.

[138] M. A. Peter and M. H. Meylan. The eigenfunction expansion of the infinite depth free surface green function in three dimensions. *Wave Motion*, 40(1):1–11, 2004.

[139] H. Prautzsch, W. Boehm, and M. Paluszny. *Bézier and B-spline techniques*, volume 6. Springer, 2002.

[140] W. G. Price and R. E. D. Bishop. Probabilistic theory of ship dynamics. *Chapman & Hall, London*, 1974.

[141] M. Riesner, G. Chillcce, and O. el Moctar. Rankine source time domain method for nonlinear ship motions in steep oblique waves. *Ships and Offshore Structures*, 14(3):295–308, 2019.

[142] M. Riesner and O. el Moctar. A time domain boundary element method for wave added resistance of ships taking into account viscous effects. *Ocean Engineering*, 162:290–303, 2018.

[143] M. Riesner, A. Von Graefe, V. Shigunov, and O. el Moctar. Prediction of non-linear ship responses in waves considering forward speed effects. *Ship Technology Research*, 63(3):135–145, 2016.

[144] P. N. Sadjang, W. Koepf, and M. Foupouagnigni. On moments of classical orthogonal polynomials. *Journal of Mathematical Analysis and Applications*, 424(1):122–151, 2015.

[145] J. T. B. Sagredo. Z-splines: moment conserving cardinal spline interpolation of compact support for arbitrarily spaced data. In *Research Report/Seminar für Angewandte Mathematik*, volume 2003. ETH, Eidgenössische Technische Hochschule Zürich, 2003.

[146] I. J. Schoenberg. Contributions to the problem of approximation of equidistant data by analytic functions. part b. on the problem of osculatory interpolation. a second class of analytic approximation formulae. *Quarterly of Applied Mathematics*, 4(2):112–141, 1946.

[147] I. J. Schoenberg. Spline interpolation and best quadrature formulae. *Bulletin of the American Mathematical Society*, 70:143–148, 1964. Communicated by Felix Browder.

[148] I. J. Schoenberg. On spline interpolation at all integer points of the real axis. *Séminaire Delange-Pisot-Poitou. Théorie des nombres*, 9(1):1–18, 1967.

[149] L. Schumaker. *Spline Functions: Basic Theory*. Cambridge Mathematical Library. Cambridge University Press, 3 edition, 2007.

[150] J. Schwarz. *An Efficient Isogeometric Boundary Element Framework Enabling Interactive Simulation*. PhD thesis, Hamburg University of Technology, 2019.

[151] P. D. Sclavounos and D. E. Nakos. Stability analysis of panel methods for free-surface flows with forward speed. In *17th Symp. on Naval Hydrodynamics*, pages 173–192, 1988.

[152] D. Scullen and E. O. Tuck. Nonlinear free-surface flow computations for submerged cylinders. *Journal of Ship Research*,

39(3):185–193, 1995.

[153] Y.-L. Shao. *Numerical potential-flow studies on weakly-nonlinear wave-body interactions with/without small forward speeds*. PhD thesis, Norwegian University of Science and Technology, 2010.

[154] Y.-L. Shao and O. M. Faltinsen. Linear seakeeping and added resistance analysis by means of body-fixed coordinate system. *Journal of marine science and technology*, 17(4):493–510, 2012.

[155] S. Sirtori, G. Maier, G. Novati, and S. Miccoli. A galerkin symmetric boundary-element method in elasticity: formulation and implementation. *International Journal for Numerical Methods in Engineering*, 35(2):255–282, 1992.

[156] V. Sladek and J. Sladek. Regularization of hypersingular integrals in bem formulations using various kinds of continuous elements. *Engineering analysis with boundary elements*, 17(1):5–18, 1996.

[157] H. Söding. A potential method for fully non-linear wave responses of ships. In *11th International Workshop on Ship and Marine Hydrodynamics (IWSH2019)*, 2019.

[158] H. Söding and V. Bertram. A 3-d rankine source seakeeping method. *Ship Technology Research*, 56(2):50–68, 2009.

[159] H. Söding, A. von Graefe, O. el Moctar, and V. Shigunov. Rankine source method for seakeeping predictions. In *International Conference on Offshore Mechanics and Arctic Engineering*, volume 44915, pages 449–460. American Society of Mechanical Engineers, 2012.

[160] H. H. Sohrab. *Basic Real Analysis*. Springer Science & Business Media, 2011.

[161] O. Steinbach. *Numerical approximation methods for elliptic boundary value problems: finite and boundary elements*. Springer Science & Business Media, 2007.

[162] A. Sutradhar, G. Paulino, and L. J. Gray. *Symmetric Galerkin boundary element method*. Springer Science & Business Media, 2008.

[163] K. Tanizawa. A nonlinear simulation method of 3d body motions in waves. *Journal of the Society of Naval Architects of Japan*, 178:96–105, 1995.

[164] J. G. Telste and F. Noblesse. Numerical evaluation of the green function of water-wave radiation and diffraction. *Journal of Ship Research*, 30(02):69–84, 1986.

[165] R. C. Thorne. Multipole expansions in the theory of surface waves. In *Mathematical Proceedings of the Cambridge Philosophical Society*, volume 49, pages 707–716. Cambridge University Press, 1953.

[166] E. O. Tuck. The effect of non-linearity at the free surface on flow past a submerged cylinder. *Journal of Fluid Mechanics*, 22(2):401–414, 1965.

[167] F. Ursell. On the heaving motion of a circular cylinder on the surface of a fluid. *The Quarterly Journal of Mechanics and Applied Mathematics*, 2(2):218–231, 1949.

[168] F. Ursell. Surface waves on deep water in the presence of a submerged circular cylinder. i. In *Mathematical proceedings of the Cambridge philosophical society*, volume 46, pages 141–152. Cambridge University Press, 1950.

[169] F. Ursell. Surface waves on deep water in the presence of a submerged circular cylinder. ii. In *Mathematical Proceedings of the Cambridge Philosophical Society*, volume 46, pages 153–158. Cambridge University Press, 1950.

[170] F. Ursell. Short surface waves due to an oscillating immersed body. *Proceedings of the Royal Society of London. Series A. Mathematical and Physical Sciences*, 220(1140):90–103, 1953.

[171] F. Ursell. The periodic heaving motion of a half-immersed sphere: the analytic form of the virtual-mass coefficient. Technical report, Victoria Univ of Manchester (United Kingdom), 1962.

[172] F. Ursell. Irregular frequencies and the motion of floating bodies. *Journal of Fluid Mechanics*, 105:143–156, 1981.

[173] F. J. Ursell. On the theory of the kelvin ship-wave source: asymptotic expansion of an integral. *Proceedings of the Royal Society of London. A. Mathematical and Physical Sciences*, 418(1854):81–93, 1988.

[174] E. F. G. Van Daalen. *Numerical and theoretical studies of water waves and floating bodies.* PhD thesis, University of Twente, 1993.

[175] K. J. Versprille. *Computer-aided design applications of the rational b-spline approximation form.* Syracuse University, 1975.

[176] H. Voss. *Numerische Methoden*. Technische Universität Hamburg-Harburg, 2010.

[177] J. H. Vugts. The hydrodynamic coefficients for swaying, heaving and rolling cylinders in a free surface. *International Shipbuilding Progress*, 15(167):251–276, 1968.

[178] J. L. Walsh, J. H. Ahlberg, and E. N. Nilson. Best approximation properties of the spline fit. *Journal of mathematics and mechanics*, pages 225–234, 1962.

[179] R. S. Wang. The numerical approach of three dimensional free-surface green function and its derivatives. *Journal of Hydrodynamics (Ser. A)*, 7(3):277–286, 1992.

[180] T. Wang, R. Yokota, and L. A. Barba. Exafmm: a high-performance fast multipole method library with c++ and python interfaces. *Journal of Open Source Software*, 6(61):3145, 2021.

[181] J. V. Wehausen and E. V. Laitone. Surface waves. In *Fluid Dynamics/Strömungsmechanik*, pages 446–778. Springer, 1960.

[182] G. Weinblum and M. St. Denis. On the motions of ships at sea. *David W Taylor Model Basin, Navy Department, Paper 2 of The Society of Naval Architects and Marine Engineers, SNAME Transactions, 1950, Paper: T1950-1 Transactions.*, 1950.

[183] G. P. Weinblum. On hydrodynamic masses. Technical report, David Taylor Model Basin Washington DC, 1952.

[184] B. West, K. Brueckner, R. Janda, D. Milder, and R. Milton. A new numerical method for surface hydrodynamcis. *Journal of Geophysical Research*, 1987.

[185] H. Wu, C. Zhang, Y. Zhu, W. Li, D. Wan, and F. Noblesse. A global approximation to the green function for diffraction radiation of water waves. *European Journal of Mechanics-B/Fluids*, 65:54–64, 2017.

[186] C. Xie. *An efficient method for the calculation of the free-surface Green function using ordinary differential equations*. PhD thesis, École centrale de Nantes, 2019.

[187] C. Xie, Y. Choi, F. Rongère, A. H. Clément, G. Delhommeau, and A. Babarit. Comparison of existing methods for the calculation of the infinite water depth free-surface green function for the wave–structure interaction problem. *Applied Ocean Research*, 81:150–163, 2018.

[188] H. Xü. *Numerical study of fully nonlinear water waves in three dimensions*. PhD thesis, Massachusetts Institute of Technology, 1992.

[189] H. Xü and D. K. P. Yue. A numerical study of kinematics of nonlinear water waves in three dimensions. In *Civil Engineering in the Oceans V*, pages 81–98. ASCE, 1992.

[190] M. Xue. *Three-dimensional fully-nonlinear simulations of waves and wave body interactions*. PhD thesis, Massachusetts Institute of Technology, 1997.

[191] M. Xue, H. Xü, Y. Liu, and D. K. P. Yue. Computations of fully nonlinear three-dimensional wave-wave and wave-body interactions. part 1. dynamics of steep three-dimensional waves. *Journal of Fluid Mechanics*, 438:11–39, 2001.

[192] R. W. Yeung. Numerical methods in free-surface flows. *Annual review of fluid mechanics*, 14(1):395–442, 1982.

[193] R. W. C. Yeung. A singularity-distribution method for free-surface flow problems with an oscillating body. Technical report, California Univ Berkeley Coll of Engineering, 1973.

[194] V. Zakharov. Stability of periodic waves of finite amplitude on the surface of a deep fluid. *Zhurnal Prikladnoi Mekhaniki i Tekhnicheskoi Fiziki*, 1968.

[195] S. Zhang, K. M. Weems, W.-M. Lin, H. Yan, and Y. Liu. Application of a quadratic boundary element method to ship hydrodynamic problems. In *International Conference on Offshore Mechanics and Arctic Engineering*, volume 48234, pages 123–133, 2008.